Computational design of patient-specific orthopedic implants
from micro-architected materials to shape-matching geometry

Garner, E.

DOI
10.4233/uuid:bbd11d77-f64a-4498-a0b8-16975f6e1e77

Publication date
2024

Document Version
Final published version

Important note
To cite this publication, please use the final published version (if applicable).
Please check the document version above.

Computational design of patient-specific orthopedic implants

Eric Garner

Delft University of Technology

Computational design of patient-specific orthopedic implants

from micro-architected materials to shape-matching geometry

Dissertation

for the purpose of obtaining the degree of doctor
at Delft University of Technology
by the authority of the Rector Magnificus, Prof.dr.ir. T.H.J.J. van der Hagen,
chair of the Board for Doctorates
to be defended publicly on
Tuesday, 12 March, 2024 at 10:00 o'clock

by

Eric GARNER

Master of Science in Integrated Product Design,
Delft University of Technology, the Netherlands,
born Montreal, Canada.

This dissertation has been approved by the promotors:
Prof. dr. A.A. Zadpoor and Dr. J. Wu.

Composition of the doctoral committee:

Rector Magnificus,	chairperson
Prof. dr. ir. A. Zadpoor,	Delft University of Technology, promotor
Dr. J. Wu,	Delft University of Technology, promotor

Independent members:

Prof. dr. ir. H.H. Weinans	Delft University of Technology
Prof. dr. ir. L.J. Sluys	Delft University of Technology
Prof. dr. Q. Li	University of Sydney, Australia
Prof. dr. ir. M. Langelaar	Delft University of Technology
Dr. J. de Kleer	Palo Alto Research Center (PARC), USA

An electronic version of this dissertation is available at
`http://repository.tudelft.nl/`.

Summary

Background: Despite over a century's worth of technical improvements, the long-term survivability associated with orthopedic implants continues to fall short. In contrast to earlier designs, implant failure is no longer caused by structural failure of the implant itself. Rather, it results from the implant's long-term detrimental effects on the surrounding bone tissue. Over time, changes in mechanical loading conditions induce a reduction in bone density, increasing the risk of fracture, and destabilizing the bone-implant interface. The mechanisms which drive peri-prosthetic bone loss are complicated and inter-related. Add to this the unique morphological variations among patients, and an optimal one-size-fits-all solution seems unlikely.

Aims: The main goal of this research is to develop computational design strategies that automatically generate patient-specific implants based on medical imaging, in an effort to improve their long-term survivability.

Methods: The proposed approach involves the application of methods from the fields of topology and shape optimization to the problem of orthopedic implant design. This includes the development of appropriate design parametrizations, and the formulation of application-specific objectives and constraints. The quality of the proposed design strategies is first assessed from a technical perspective, in terms of their efficiency, robustness and stability – and then, from a clinical perspective, in terms of their effectiveness in addressing the application-specific design objectives and constraints.

Results: To overcome the conflicting stress-related design requirements, a new multi-scale optimization strategy was developed based on a novel micro-architected material parametrization. The proposed parametric micro-architecture is capable of achieving a wide range mechanical properties, while constructed from a single material. By varying the micro-architecture parameter values throughout the design domain, local mechanical and geometric properties can be finely tuned to achieve a favorable mechanical response. The smooth relationship between the micro-architecture parameters and mechanical properties allows for decoupled multi-scale optimization, wherein mechanical properties are interpolated from pre-computed data. This eliminates the computationally expensive asymptotic homogenization step from the optimization procedure, and has proven to be an extremely efficient

approach. The proposed multi-scale optimization strategy was applied to the design of hip stems, with excellent results. A significant reduction was achieved in the predicted rate of peri-prosthetic bone loss, without any increase in the risk of interface fracture. This new parametrization also facilitates the incorporation of manufacturing-related and functional constraints, such as the need for osseointegration, which is one of the primary implant fixation mechanisms in cementless joint replacement surgery. Osseointegration requires near-perfect contact along the bone-implant interface. To address this requirement, a new shape optimization strategy was developed. The proposed method was applied to the design of acetabular components where is has proven highly effective in eliminating reaming-related bone loss, while simultaneously improving interface contact. In order to be usable in real world implant design, the optimization strategy also required the development of a constraint to ensure insertability of the implant into the host bone. The proposed insertability metric is the first of its kind, and may be applied to assess and optimize designs in a broad range of applications, beyond the design of orthopedic implants.

Discussion: These numerical results represent an encouraging first step towards the development and adoption of patient-specific implant designs in the orthopedics community. Future research may also see the design and incorporation of other application-specific requirements. New objective functions may, for example, target the promotion of strain and surface geometry-related bone ingrowth. Future design strategies may also attempt to model the effects of growth hormone on osseointegration, or even include biodegradable materials in the design process.

Samenvatting

Achtergrond: Ondanks ruim een eeuw aan technische verbeteringen blijft de levensduur van orthopedische implantaten tekortschieten. In tegenstelling tot vroege ontwerpen wordt het falen van het implantaat niet langer veroorzaakt door een structureel falen van het implantaat zelf, maar resulteert eerder uit het langdurige schadelijke effect van het implantaat op het omringende botweefsel. Na verloop van tijd veroorzaken veranderingen in belasting een afname van botdichtheid, waardoor het risico op fracturen toeneemt en de hechting tussen bot en implantaat verstoord wordt. De belastingen die leiden tot botverlies rondom het implantaat zijn complex en onderling verbonden. Als men daar de unieke morfologische variaties tussen patiënten aan toe voegt lijkt een optimale *one-size-fits-all* oplossing onwaarschijnlijk.

Doelen: Het belangrijkste doel van dit onderzoek is het ontwikkelen van computationele ontwerp strategieën die automatisch patiëntspecifieke implantaten genereren op basis van medische beeldvorming, in een poging om hun levensduur te verbeteren.

Methoden: De voorgestelde aanpak omvat de toepassing van methoden uit de vakgebieden van de topologie en vormoptimalisatie op het probleem van het orthopedisch implantaatontwerp. Dit omvat de ontwikkeling van een passend parametrisch ontwerp en het formuleren van toepassingsspecifieke doelstellingen en beperkingen. De kwaliteit van de voorgestelde ontwerpstrategieën worden eerst beoordeeld vanuit een technisch perspectief, rekening houdend met hun efficiëntie, robuustheid en stabiliteit – en vervolgens, vanuit een klinisch perspectief, en hun effectiviteit bij het aanpakken van de toepassingsspecifieke ontwerpdoelstellingen en beperkingen.

Resultaten: Om de conflicterende stress-gerelateerde ontwerpeisen te overwinnen, is er een nieuwe multi-schaal optimalisatiestrategie ontwikkeld op basis van een nieuwe parameterisatie van micro-gearchitectuurde materialen. De voorgestelde parametrische micro-architectuur is in staat om een breed scala aan mechanische eigenschappen te bereiken, terwijl deze uit één materiaal is opgebouwd. Door de parameterwaarden van de micro-architectuur in het hele ontwerpdomein te variëren, kunnen lokale mechanische en geometrische eigenschappen nauwkeurig worden afgestemd om een gunstige mechanische respons te bereiken. Deze methode heeft zichzelf buitengewoon efficiënt bewezen en is in staat om het voorspelde tempo van peri-prothetisch botverlies aanzienlijk te verminderen, evenals het risico op interfacebreuken. Om aan deze eis te voldoen, is er een nieuwe vormoptimalisatiestrategie ontwikkeld. Deze optimalisatie heeft bewezen succesvol te zijn in het bereiken van maximaal contact tussen interfaces met minimalisering van het bijbehorende bot verlies. Deze optimalisatiestrategie vereiste ook de ontwikkeling van een beperking

om ervoor te zorgen dat het implantaat in het gastheerbot kan worden geplaatst zonder interferentie. De voorgestelde metriek voor implantatie is de eerste in zijn soort en kan worden toegepast om ontwerpen te beoordelen en te optimaliseren in een breed scala van toepassingen.

Discussie: Deze numerieke resultaten zijn een bemoedigende eerste stap richting de ontwikkeling en adoptie van patiënt specifieke implantaten in de orthopedische gemeenschap. Toekomstig onderzoek kan ook betrekking hebben op het ontwerp en de integratie van andere toepassingsspecifieke vereisten. Met name ontwikkelingen naar herconfigureerbare structuren en beperkte articulatie kunnen worden toegepast op het ontwerp van orthopedische implantaten met nieuwe en spannende functionaliteit.

There is no true one-size-fits-all. One size fits one – at best.

Acknowledgements

Firstly, I would like to thank my supervisor and promotor, Jun Wu, for introducing me to the field of computational design, and for always having my best interests in mind when guiding me through this chapter in my life. I would also like to thank my promoter, Amir Zadpoor, for giving me the freedom to work on the topics that captured my interest, and for allowing me the flexibility to find a suitable working arrangement. Of course, I would like to thank my girlfriend Barbara, as well as my friends and family for their support throughout this – admittedly longer than expected – journey. I would also like to thank everyone who facilitated this work, either by providing access to their code, technical knowledge, or experience. In particular, I must thank my co-authors Alexander Meynen and Lennart Scheys for providing access to their results and for their efforts in our shared publications. And I must also thank Ole Sigmund, Erik Andreassen, Anders Clausen, Mattias Schevenels, Boyan Lazarov, Oded Amir, Niels Aage, Thomas-Peter Fries, Kai Liu, Andrés Tovar, and Krister Svanberg for publishing open source code that served as a basis for much of my work. I have never met most of these people, but they have saved me countless hours of work, and for that I am very grateful. Finally, thank you to Eric Garling, Michael Ormond, Rob Nelissen, and Gerald Kraan for sharing their technical knowledge and industry experience.

Contents

Introduction

1.1 Background

The advent of joint replacement surgery has revolutionized the treatment of osteoarthritis, and is considered to be among the most successful orthopedic interventions in modern history. This success is the result of over a century's worth of incremental improvements through innovation and development, in all areas of science. In their earliest embodiment, implants used in joint replacement surgery were made from natural materials such as ivory, glass, and, eventually, metal [19]. They were invasive, and were prone to rapid deterioration, generating wear particles that lead to bone loss and implant loosening. Since then, better designs and new materials have improved the service life of orthopedic implants. However, in spite of these advances, the need for revision surgery due to implant failure still persists. One reason for long term implant failure relates to the mechanical interaction between the implant and the surrounding bony tissue [63, 111, 66]. Bone is a living material that reacts to its environment. Among other factors, cyclical mechanical stresses are needed to activate the mechanisms that maintain bone density. When bones are modified and embedded with implants, the loading conditions change significantly, triggering the bone remodeling process, and often resulting in bone degeneration. Over time, this can lead to implant loosening, chronic pain, peri-prosthetic fracture, or catastrophic failure of the bone-implant system [63, 111, 66]. While this problem of peri-prosthetic bone deterioration is now well-known, it remains unsolved.

Numerical methods, enabled by modern high-performance computing, have been developed to perform precise analysis of complex systems and structures. Finite element methods (FEM), decompose complex structures into small (finite) elements and use linear algebra to solve the differential equations that govern their behavior under load. These techniques have become an integral part of the validation and performance analysis of new designs in all areas of engineering. Going a step further, researchers have developed optimization strategies that use the results of these numerical analyses to iteratively improve designs without ever building a single prototype. This innovation represents a paradigm shift in engineering design and optimization.

In parallel to these developments, advances in additive manufacturing, or 3D printing, have enabled the precise fabrication of extremely complex one-off designs with little to no lead time. This technology has triggered an explosion of application-specific and even consumer-specific products with unmatched levels of performance. Together, numerical methods and additive manufacturing offer unprecedented possibilities for tackling the most complex engineering challenges. Now, more than ever, a solution to the problem of bone-implant compatibility seems within reach.

1.2 Challenges in design of orthopedic implants

The mechanisms that drive peri-prosthetic bone loss are complicated and interrelated. Add to this the unique morphological variations among patients, and an optimal one-size-fits-all solution seems unlikely. Yet, modern surgical practice continues to favor the use of generic components over patient-specific designs. The reasons for this are primarily pragmatic; the current design process is simply too labor-intensive and expensive for general use. It involves manual analysis and careful design by expert engineers, surgeons, and trained technicians. As a result, patient-specific implants are only ever employed in the most challenging of cases, where no generic options are suitable. A promising alternative, which would ultimately require minimal additional resources as compared to generic implants is to develop computational tools that automatically generate patient-specific designs, based on standard medical scans. This would allow us to leverage our understanding of bone remodeling and interface fracture mechanics to create patient-specific designs that promote long-term implant stability and peri-prosthetic bone health.

1.2.1 Bone remodelling

Bone remodeling is a continuous process of synthesis and destruction through a complex sequence of cellular events. This process is understood to be driven by, among other things, local stress conditions present throughout the bone [66]. Stress shielding, which is a reduction in the load-induced stresses resulting from the presence of a stiff implant, triggers the bone remodeling process, increasing the risk of implant failure. Less stiff implant materials, a natural solution to the problem of stress shielding, also tend to increase the induced tensile and shear stresses along the bone-implant interface, increasing the risk of micro-slipping and interface fracture [79]. To add insult to injury – no pun intended – micro-slipping produces wear particles that may trigger an inflammatory response, resulting in –

you guessed it – more bone remodeling [118]. Figure 1.1 (left) shows how this issue affects femoral health in the case of total hip replacement (THA). Finding a way to simultaneously address both of these stress-related issues remains an open challenge.

1.2.2 Osseointegration

As previously mentioned, interface stability is an extremely important factor in the long-term survivability of orthopedic implants. It is dependent not only on local stress conditions but also on the strength of the interface itself. Modern medical practice favours cementless joint reconstruction methods, using porous titanium implants [47]. Fixation, therefore, is provided by a combination of surface friction and bony ingrowth into the porous implant surface (osseointegration). Naturally, then, the strength of the resulting bone-implant interface is highly dependent on the congruity of the interface surfaces, *i.e.*, the degree to which they line up with one another. Figure 1.1 (right) shows the poor interface contact and significant bone loss associated with a generic hemispherical acetabular component used in total hip replacement.

1.3 Main goals

In broad terms, the aim of this research is to develop and apply methods from the field of numerical optimization to the design of orthopedic implants. In doing so, this project is intended to make a case for the commercial use of computationally generated patient-specific implants with improved biocompatibility and long-term survivability. Specifically, the project concentrates on two design aspects. The first focuses on structural mechanics and aims to understand how the conflicting stress-related requirements can be managed through the use of micro-architected materials. The second aspect concerns osseointegration and the need for a congruent bone-implant interface. Here, the objective is to develop methods that produce a stable bone-implant interface, while limiting bone loss and ensuring the insertability of the final design.

Hip stem design   **Acetabular cup design**

Solid titanium

Bone remodeling   Interface risk   Defect pelvis   Bone-implant contact

Titanium lattice

Bone remodeling   Interface risk   Resection depth   Resected surface
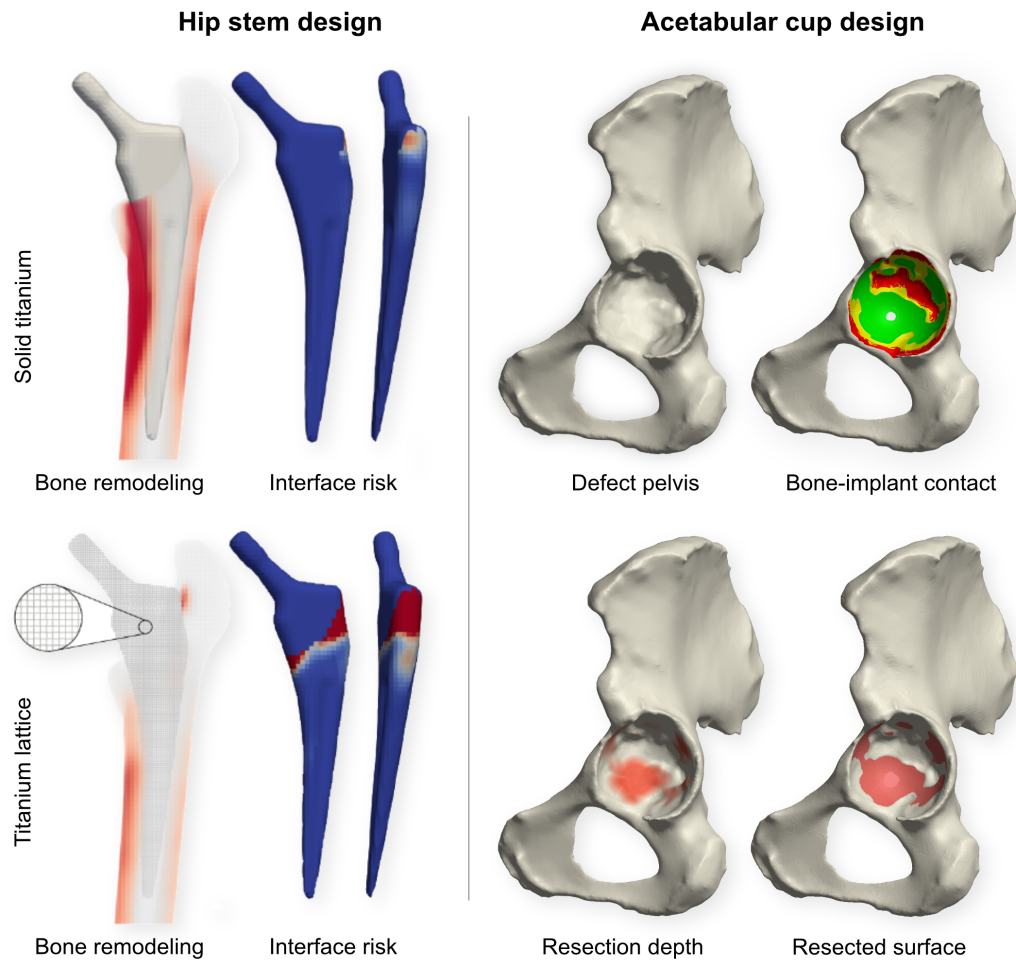
Fig. 1.1.: Some of the shortcomings associated with generic orthopedic implants. Left: Bone remodelling and interface fracture risks, for solid and uniform lattice hip stems. Right: Interface contact and bone resection associated with a hemispherical acetabular component.

1.4 Contributions

Fig. 1.2 presents an overview of the ideas explored in each chapter. Beginning with an investigation into the inter-compatibility between micro-architectures within a heterogeneous lattices, focus then shifts to the interactions between tuned heterogeneous lattice implants and bone tissue. Finally, a solution to the problem of insertability in implant design is presented, along with an application to acetabular cups used in total hip arthroplasty.

Titanium is an ideal material for orthopedic implants in that it is bio-inert and provides excellent stiffness, strength, and toughness. However, this high stiffness is

precisely what leads to stress-shielding-related bone loss. Traditionally, implants are made from a solid block of titanium. But what if a fine lattice structure was used instead? Then, the implant would behave much like if it were made from a softer material. How about if a spatially varying lattice was used? Then, it would behave in a new way, defined by the specific configuration of the spatially-varying lattice. The ability to produce a desired mechanical response by finely tuning local material properties may be precisely what is needed to tackle the conflicting stress-related requirements encountered in the design of orthopedic implants.

A micro-architected material, often referred to as a microstructure, is a periodically repeating structure that behaves much like a new material whose mechanical properties follow both from the base material and from the geometry of the repeating unit cell. This concept can be exploited to achieve extraordinary or highly tailored mechanical properties. Going a step further, multi-scale structures with spatially varying micro-architectures can be designed to produce desirable deformation modes under mechanical load. The design of such structures, however, requires careful consideration of the interface between regions with differing micro-architectures. If, for example, two adjacent micro-architectures are not well-connected along their interface, then the whole structure may not perform as expected, and may even fail prematurely. Chapter 2 presents a novel "super-cell" design method for handling this issue. By considering each cell within the context of a larger neighborhood, the design process naturally favors compatible micro-architectures. Another approach to multi-scale optimization circumvents the problem entirely by prescribing a parametric micro-architecture with guaranteed adjacent-cell compatibility. This formulation allows for an efficient decoupled solution but is limited by the choice of parametric micro-architecture. Chapter 3 presents a multi-scale optimization strategy that employs a newly developed parametric micro-architecture capable of achieving a wide range of mechanical properties. The new micro-architecture, which is a generalization of the well-known anti-chiral auxetic micro-architecture [52], is parameterized to produce smoothly varying geometric and mechanical properties. As a result, the mechanical properties for any arbitrary parameter values can be interpolated from a pre-computed dataset, eliminating the need for repeated analysis via asymptotic homogenization. This innovation represents a significant efficiency boost in the design of 3D multi-scale structures. To incorporate this parametrization into a multi-scale optimization framework, a new distance function-based cost function was designed to restrict the individual unit cell parameter combinations to within the permitted design space.

With generic implants, interface stability is achieved by reaming the host bone and press-fitting the implant into place. This process potentially leaves interface

Micro-architectural compatibility

Multi-scale, multi-objective optimization

Shape-matching insertable implants

Posterior view

Medial view

Anterior view

Lateral view
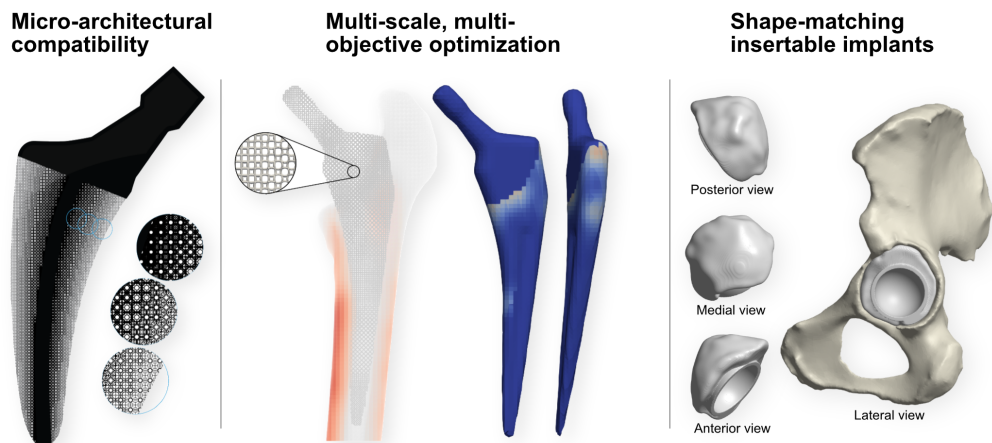
Fig. 1.2.: Chapter overview: Chapter 2 focuses on adjacent-cell compatibility in multi-scale design, introducing a novel "super-cell" formulation. Chapter 3 presents an efficient multi-scale and multi-objective approach to implant design. Chapters 4 & 5 introduces a comprehensive automated design strategy for shape-matching, bone-preserving and insertable acetabular components.

gaps in areas with bone deficiency, and often results in a significant loss of healthy bone stock. A straightforward alternative leverages medical imaging to produce patient-specific implants with interface-matching geometry. These designs, however, would not necessarily be insertable into the host bone cavity, without interference. To address this issue, a novel insertability metric is presented in Chapter 4. The new metric can efficiently determine if a given design is insertable into a matching cavity. In contrast to other methods, the new metric does not require the computation of a complete insertion path and is not limited to rectilinear motion. Moreover, the metric is continuously differentiable and can be readily included as a constraint in shape or topology optimization routines. In Chapter 5, the insertability constraint is coupled with a shape-matching and bone-preserving objective function to automatically optimize the design of patient-specific acetabular components for use in total hip arthroplasty.

Compatibility in Microstructural Optimization

2

Abstract

Microstructures with spatially-varying properties such as trabecular bone are widely seen in nature. These functionally graded materials possess smoothly changing microstructural topologies that enable excellent micro and macro-scale performance. The fabrication of such microstructural materials is now enabled by additive manufacturing (AM). A challenging aspect in the computational design of such materials is ensuring compatibility between adjacent microstructures. Existing works address this problem by ensuring geometric connectivity between adjacent microstructural unit cells. In this chapter, we aim to find the optimal connectivity between topology optimized microstructures. Recognizing the fact that the optimality of connectivity can be evaluated by the resulting physical properties of the assemblies, we propose to consider the assembly of adjacent cells together with the optimization of individual cells. In particular, our method simultaneously optimizes the physical properties of the individual cells as well as those of neighbouring pairs, to ensure material connectivity and smoothly varying physical properties. We demonstrate the application of our method in the design of functionally graded materials for implant design (including an implant prototype made by AM), and in the multi-scale optimization of structures.

2.1 Introduction

In recent years, advances in additive manufacturing have made it possible to fabricate cellular materials whose mechanical properties are defined not only by their chemical
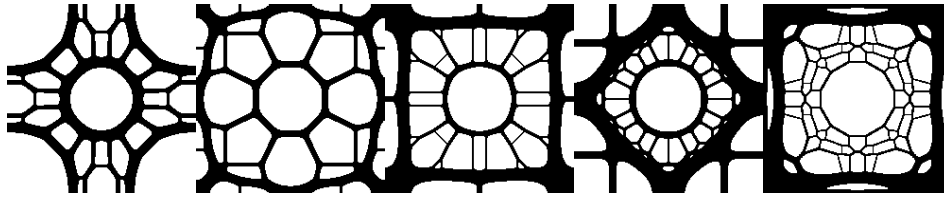
Fig. 2.1.: Illustration of poorly connected microstructures. The unit cells are individually optimized for maximum bulk modulus under linearly-varying volume fractions from 30% to 50%, from left to right.

composition, but also by their micro-scale topologies [91]. These microstructural materials, also referred to as architected materials [106] or meta-materials [168], can be designed to possess highly tailored or extreme physical properties not usually found in nature.

A systematic approach in the computational design of microstructural materials is to define the material as a periodic array of identical unit cells, and to formulate it as a topology optimization problem [14]. This process, often called inverse homogenization [133], optimizes the material distribution within the design space of a single unit cell, and uses homogenization theory to evaluate the effective properties of the material. Inverse homogenization has been used to design periodic microstructures with exceptional properties such as maximized bulk modulus [133, 27], negative Poisson's ratio [133, 6], and negative thermal expansion [132], among others (cf. [23, 106]).

While the optimization of periodic microstructures has been studied in depth, less attention has been paid to the assembly of optimized microstructures with spatially-varying properties. Such inhomogeneous microstructures are of great importance in engineering design. For instance, when designing orthopaedic implants, it may be desirable to have a continuous transition from denser microstructures in the central region to highly porous microstructures at the bone-implant interface. This functional gradation promotes bony ingrowth at the bone-implant interface, while maintaining structural integrity and increasing the mechanical properties in the areas where bony ingrowth is irrelevant [11].

A critical issue in the assembly of spatially-varying microstructures relates to the compatibility of neighbouring microstructures. As illustrated in Fig. 2.1, individually optimized neighbouring cells do not necessarily form an integral part, and the physical properties along their shared boundaries are unpredictable and often inferior to those of the individual microstructures.

Existing works typically address this problem by pursuing geometric connectivity between adjacent microstructural unit cells. In the design of functionally graded materials (FGMs), Zhou and Li [169] proposed three methods to address the connectivity issue, namely *kinematic connective constraint*, *pseudo load* and *unified formulation with non-linear diffusion*. In the first two methods, unit cells are optimized individually, while constraints are imposed to connect optimized cells with predefined common regions. The kinematic approach has been adopted by Li et al. [86]. In the unified formulation, unit cells are optimized all together, and a non-linear diffusion term is introduced in the objective function to penalize disconnection. The computational efficiency of the unified formulation is improved by successively optimizing new unit cells while considering connection to cells that have been optimized [114]. An alternative approach is to optimize some key microstructures, and apply geometric interpolation to obtain intermediate microstructures between individually optimized unit cells [33]. This geometric approach works for microstructures of similar topology.

In this chapter, we aim to find the optimal connectivity between topology optimized microstructures. Given the fact that the optimality of connectivity can be evaluated by the resulting physical properties of the assemblies, we propose to consider the assembly of adjacent cells together with the optimization of individual cells. In particular, our method simultaneously optimizes the physical properties of the individual cells as well as those of neighbouring pairs, to ensure material connectivity and smoothly varying physical properties. This idea is substantiated on the design of graded microstructures with maximized bulk moduli under varying volume fractions. The graded microstructures are employed in designing an implant (cf. Fig. 2.2), which is fabricated by additive manufacturing.

Our method could also be applied to improve multi-scale structural optimization, where poor connectivity across neighbouring microstructures has recently received considerable attention. For example, Cramer et al. [33] proposed a bottom-up approach to multi-scale optimization, where a set of optimized and interpolated microstructures is used as building blocks for macro-scale optimization. To circumvent the connectivity issue in optimized microstructures, parametrized lattice structures are commonly used in bottom-up approaches (e.g. [149, 107, 85]). The parametrization, nevertheless, reduces the design space and limits the range of possible topologies. Our method places no restrictions on the topology and generates optimized, compatible microstructures. In a different approach, Zhu et al. [170] proposed a two-scale method where the gamut of microstructures is pre-computed. In the subsequent mapping process, boundary similarity across adjacent cell interfaces is taken into account for selecting the microstructures.
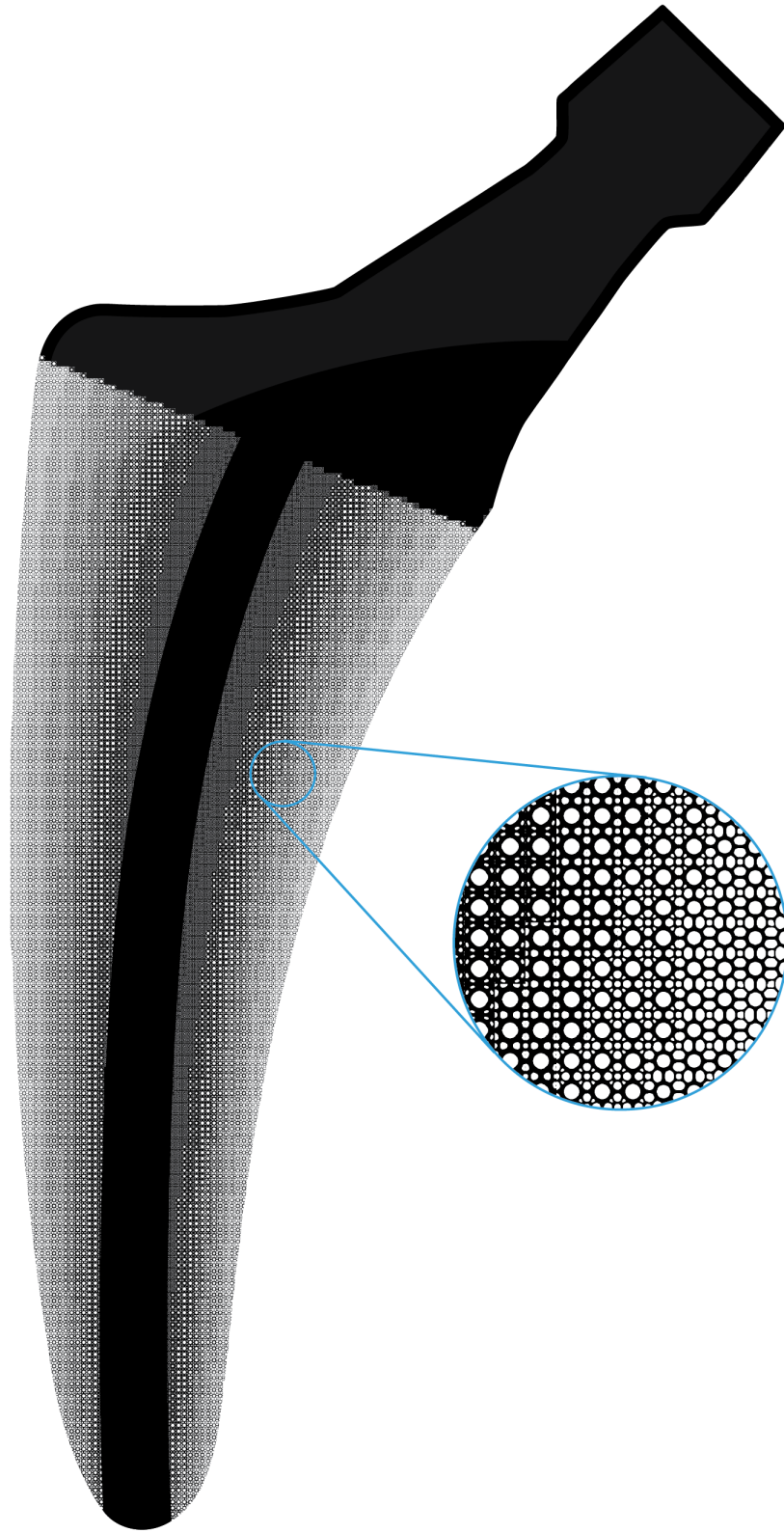
Fig. 2.2.: An orthopaedic implant with functionally graded microstructures optimized by the proposed method. The different microstructures have distinct topologies but are still well connected, forming an integral part.

Concurrently optimizing the microstructural material and the macro-structure gives more flexibility in design. Rodrigues et al. [121] proposed hierarchical optimization of material and structure. This was later extended to 3D [32]. Integrating our method into the hierarchical approach results in two-scale structures with improved connectivity. A recent survey on hierarchical optimization of material and structure is given by Xia and Breitkopf [162]. In contrast to the isoparametric microstructures with four-fold rotational symmetry generated in the design of FGMs, the microstructures generated in concurrent multi-scale optimization possess two-fold rotational symmetry and therefore more topological variations and direction-dependent properties. Wang and colleagues [150, 152] developed a level-set method to obtain topologically similar and, thus, connectable, microstructures. Du and Kim [40] proposed a physics-independent connectivity index, which ensures good geometric connectivity by progressively modifying each microstructure to be well connected to its nearest neighbour. Alexandersen and Lazarov [2] and Wu et al.[156, 157] performed structural analysis and optimization on the fully refined microstructure details, naturally ensuring the connectivity of the resulting microstructures. The full scale analysis is computationally intensive, thereby limiting the microstructural details that can be practically optimized.

The remainder of the chapter is organized as follows. In Section 2.2, we introduce the compound formulation for optimizing compatibility in microstructures, building upon inverse homogenization and density-based topology optimization. In Section 2.3, we analyze the performance of optimized microstructures and demonstrate their usage in the design of an implant. Section 2.4 demonstrates the applicability of the proposed method in multi-scale structure optimization. Finally, the most important conclusions from this study are summarized in Section 2.5.

2.2 Compatibility Optimization with Compound Formulation

To start with, let us consider the design of a 2D functionally graded cellular material with a density gradation in one direction and periodicity in the other (see Fig. 2.3). The design domain of the graded material (referred to as GM) is composed of N square subdomains, each for a unique unit cell. Generating the unit cells in isolation leads to the lack of connectivity between adjacent cells. Here, we propose a holistic approach that generates the unit cells simultaneously in a unified formulation,

incorporating the mechanical behaviour across adjacent microstructures in the optimization.

The design of graded materials is formulated as an inverse homogenization problem based on finite element analysis and density-based topology optimization [15]. Let us denote the design domain of the GM by Ω and the subdomain of each unit cell by $\Omega^n, n = 1, ..., N$. Each subdomain is discretized into square finite elements for mechanical analysis. For each element, the volume fraction of solid material (also referred to as pseudo density), $\rho_e^n \in [0, 1]$, serves as the design variable, with $\rho_e^n = 0$ (or $\rho_e^n = 1$) indicating that the element is empty (or solid). The density distribution within each unit cell is optimized to maximize a specific mechanical property (e.g. bulk modulus), derived from the effective elasticity tensor, and is subject to a volume fraction constraint, which varies linearly in the graded direction.

To ensure optimal connectivity between adjacent cells, the idea is to directly incorporate into the objective function a term which quantifies the degree of connectivity. A simple measure of connectivity between adjacent cells is the number of shared elements across the interface. This type of geometric measures, however, does not reflect any mechanical properties of the connection. An effective and intuitive measure of the mechanical connectivity considers the mechanical properties of the assembled cells as a compound part. To this end, we introduce the concept of compound cells. Each compound cell is composed of two neighbouring unit cells (Fig. 2.4). The mechanical properties of the compound cell serve as an effective measure of the mechanical connectivity. The objective function is therefore defined as a weighted average of the individual and compound cell objectives.

The mathematical formulation of the optimization problem is written as

$$
\begin{aligned}
\max_{\rho} \quad & J = (1 - \omega) \sum_{n=1}^{N} f(E^H(\boldsymbol{\rho}^n)) + \\
& \omega \sum_{n=1}^{N-1} f(E^H([\boldsymbol{\rho}^n, \boldsymbol{\rho}^{n+1}])) \\
\text{s.t.} \quad & : \sum_{e=1}^{M} v_e^n \rho_e^n / |Y^n| \leq V^n, \ \forall n \\
& : 0 \leq \rho_e^n \leq 1, \ \forall e, n.
\end{aligned} \tag{2.1}
$$

In the objective function, an abstract function f derives an objective from the effective elasticity tensor (E^H), which depends on the density vector $\boldsymbol{\rho}^n$ (or $[\boldsymbol{\rho}^n, \boldsymbol{\rho}^{n+1}]$) of a unit (or compound) cell. A weighting factor ω determines the influence of the compound cells on the optimization of individual unit cells. With $\omega = 0$, this

objective function is equivalent to the microstructure design formulation where the connectivity is not taken into account.
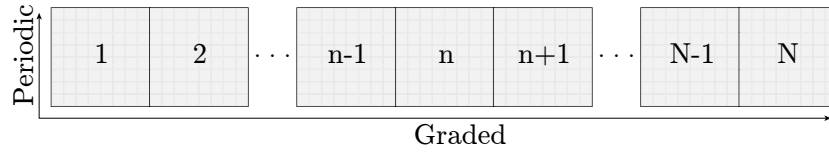
Fig. 2.3.: Illustration of a 2D graded material, comprising N unique unit cells.
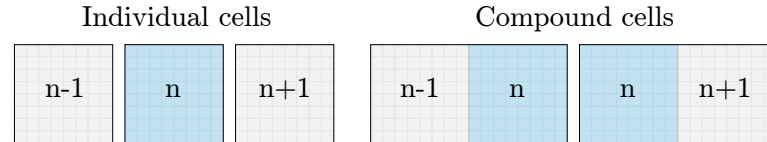
Fig. 2.4.: Unit cell n shown individually and a part of compound cells $(n - 1, n)$ and $(n, n + 1)$.

The first constraint restricts the volume fraction of each individual cell. M is the number of the finite elements per unit cell. v_e^n is the area or volume of a finite element. $|Y^n|$ is the area or volume of the unit cell domain. V^n is a prescribed volume fraction. The second constraint restricts the element density ρ_e^n between 0 and 1. For the sake of clarity, the state equations which are known in inverse homogenization for evaluating the elasticity tensor (E^H) are omitted here, and will be introduced in the following subsection.

This formulation can be extended to achieve some desirable properties of the graded material, e.g., gradation in multiple directions. The optimization problem as formulated in Eq. 2.1 only ensures that neighbouring unit cells are compatible along a single direction. The compatibility along the other direction can be ensured by a rotational symmetry constraint on each unit cell. This constraint has been realized by assigning a single design variable to, and averaging the sensitivities of, the elements that are corresponding due to the symmetry condition [158].

More extensions will be discussed and their effects on the optimized cells will be demonstrated in the results section. In the following, we proceed to the essential steps in inverse homogenization.

2.2.1 Homogenization

We make use of homogenization theory to predict the effective elasticity tensor of both individual and compound cells. According to the homogenization theory [56,

133, 161], the effective elasticity tensor (E^H) for a periodic microstructure is given by

$$E_{ijkl}^H = \frac{1}{|Y|} \int_Y E_{ijpq}(\varepsilon_{pq}^{0(kl)} - \varepsilon_{pq}^{*(kl)})dY, \qquad (2.2)$$

where $|Y|$ is the area or volume of the cell domain Y in $\mathbb{R}^2$ or $\mathbb{R}^3$, respectively. $\varepsilon_{pq}^{0(kl)}$ corresponds to the independent unit test strains (in 2D there are three; e.g. unit strain in the horizontal direction, unit strain in the vertical direction, and unit shear strain). $\varepsilon_{pq}^{*(kl)}$ is the Y-periodic solution to the variational type problem

$$\int_Y E_{ijpq}\varepsilon_{pq}^{*(kl)}\frac{\partial \nu_i}{\partial y_i}dY = \int_Y E_{ijpq}\varepsilon_{pq}^{0(kl)}\frac{\partial \nu_i}{\partial y_i}dY, \ \forall \nu \in V, \qquad (2.3)$$

where ν is a Y-admissible displacement field.

Using an energy-based approach [58], the elasticity tensor is rewritten as

$$E_{ijkl}^H = \frac{1}{|Y|} \int_Y E_{pqrs}\left(\varepsilon_{pq}^{0(ij)} - \varepsilon_{pq}^{*(ij)}\right)\left(\varepsilon_{rs}^{0(kl)} - \varepsilon_{rs}^{*(kl)}\right)dY. \qquad (2.4)$$

In finite element form, for a cell discretized into M elements, the effective tensor is approximated by

$$E_{ijkl}^H = \frac{1}{|Y|} \sum_{e=1}^{M} (\mathbf{u}_e^{*(ij)})^T \mathbf{k}_e \mathbf{u}_e^{*(kl)}, \qquad (2.5)$$

where $\mathbf{u}_e^{*(ij)}$ are the element displacement solutions corresponding to the unit test strain fields $\varepsilon^{0(ij)}$, and $\mathbf{k}_e$ is the stiffness matrix of an element.

It should be noted that the homogenization theory assumes infinite periodicity of the microstructures, and as such may not provide accurate results when used to generate spatially-varying microstructure distributions. However, it has been shown that reasonable accuracy can be expected if the gradient of material properties is sufficiently small [169]. This has been confirmed in our numerical tests.

Equilibrium equations

To evaluate the elasticity tensor, equilibrium equations corresponding to the linearly independent unit test strain fields must be solved for each individual and compound cell. For the individual cells, the equilibrium is written as:

$$\mathbf{K}_n \mathbf{U}_n^{A(kl)} = \mathbf{F}_n^{(kl)}, \ k, l = 1, ..., d, \ n = 1, ..., N, \qquad (2.6)$$

and for the compound cells:

$$\mathbf{K}_{n,n+1}\mathbf{U}_{n,n+1}^{A(kl)} = \mathbf{F}_{n,n+1}^{(kl)}, \; k,l = 1, ..., d, \; n = 1, ..., N-1, \tag{2.7}$$

where, for each individual cell n, $\mathbf{K}_n$ is the global stiffness matrix, $\mathbf{U}_n^{A(kl)}$ and $\mathbf{F}_n^{(kl)}$ are the global displacement vector and external force vector of the test case (kl), respectively. Similarly, for each compound cell $(n, n+1)$, $\mathbf{K}_{n,n+1}$ is the global stiffness matrix, $\mathbf{U}_{n,n+1}^{A(kl)}$ and $\mathbf{F}_{n,n+1}^{(kl)}$ are the global displacement vector and external force vector of the test case (kl), respectively.

The individual contributions of each element to the global stiffness matrix $\mathbf{K}_n$ are calculated as $\mathbf{k}_e = E_e(\rho_e)\mathbf{k}_0$, where $\mathbf{k}_0$ is the stiffness matrix of a solid element and $E_e(\rho_e)$ is the Young's modulus corresponding to element e, interpolated via the modified solid isotropic material with penalization (SIMP), given by

$$E_e(\rho_e) = E_{min} + \rho_e^\gamma (E_0 - E_{min}), \tag{2.8}$$

where E_0 is the Young's modulus of a solid element, E_{min} is a small term assigned to prevent the global stiffness matrix from becoming singular, and γ is a penalization factor (typically $\gamma = 3$).

Objective function

The objective function is formulated to maximize or minimize a specific material property, derived from the elasticity tensor. Using the engineering notation with $11 \to 1$, $22 \to 2$, and $12 \to 3$, the elasticity tensor, E_{ijkl}^H in Eq. (2.5), is rewritten as

$$G_{ij} = \frac{1}{|Y|} \sum_{e=1}^{M} (\mathbf{u}_e^{*(i)})^T \mathbf{k}_e \mathbf{u}_e^{*(j)}. \tag{2.9}$$

For the individual and compound cells, respectively, the objective is defined generically as:

$$f(\overline{G}(\boldsymbol{\rho}^n)) = \sum_{i,j=1}^{3} r_{ij} G_{ij}^n, \tag{2.10}$$

and

$$f(\overline{G}([\boldsymbol{\rho}^n, \boldsymbol{\rho}^{n+1}])) = \sum_{i,j=1}^{3} r_{ij} G_{ij}^{n,n+1}, \tag{2.11}$$

where r_{ij} are constant values, typically 1 or 0. For maximizing bulk modulus, $r_{11} = r_{22} = r_{12} = r_{21} = 1$, all others are 0. $G_{ij}^{n,n+1}$ represents the elasticity tensor of the compound cell composed of unit cells n and $n+1$.

The optimization problem is solved by the method of moving asymptotes (MMA) [143]. The required sensitivities for the objective functions (2.10) and (2.11) are, respectively

$$\frac{\partial f}{\partial \rho}\left(\overline{G}(\boldsymbol{\rho}^n)\right) = \sum_{i,j=1}^{3} r_{ij} \frac{\partial G_{ij}^n}{\partial \rho}, \tag{2.12}$$

and

$$\frac{\partial f}{\partial \rho}\left(\overline{G}([\boldsymbol{\rho}^n, \boldsymbol{\rho}^{n+1}])\right) = \sum_{i,j=1}^{3} r_{ij} \frac{\partial G_{ij}^{n,n+1}}{\partial \rho}, \tag{2.13}$$

where $\frac{\partial G_{ij}^n}{\partial \rho}$ and $\frac{\partial G_{ij}^{n,n+1}}{\partial \rho}$ are computed using the adjoint method [14]

$$\frac{\partial G_{ij}}{\partial \rho} = \frac{1}{|Y|} \gamma \rho_e^{\gamma-1} (E_0 - E_{min})(\mathbf{u}_e^{*(i)})^T \mathbf{k}_0 \mathbf{u}_e^{*(j)}. \tag{2.14}$$

2.2.2 Three-field SIMP

We make use of the three-field approach in topology optimization using SIMP [57, 134, 163]. Rather than directly optimizing the density field ρ, a design field ϕ is introduced. The design field ϕ is smoothed by a density filter, obtaining a smoothed field $\tilde{\phi}$. This is followed by a projection operation using a smoothed Heaviside function to obtain the density field $\rho = \overline{\tilde{\phi}}$.

Filtering

The density filter eliminates common checkerboarding (i.e., regions of alternating solid and void elements) inherent to low order discretization. The smoothed density $\tilde{\phi}_e$ is defined as a weighted average of the neighbouring design variables, i.e.,

$$\tilde{\phi}_e = \frac{\sum_{i \in \mathbb{M}_e} \omega_{i,e} \phi_i}{\sum_{i \in \mathbb{M}_e} \omega_{i,e}}, \tag{2.15}$$

where the neighbourhood of element e is defined as

$$\mathbb{M}_e = \{i|\ \|x_i - x_e\|_2 \leq r_e\}, \tag{2.16}$$
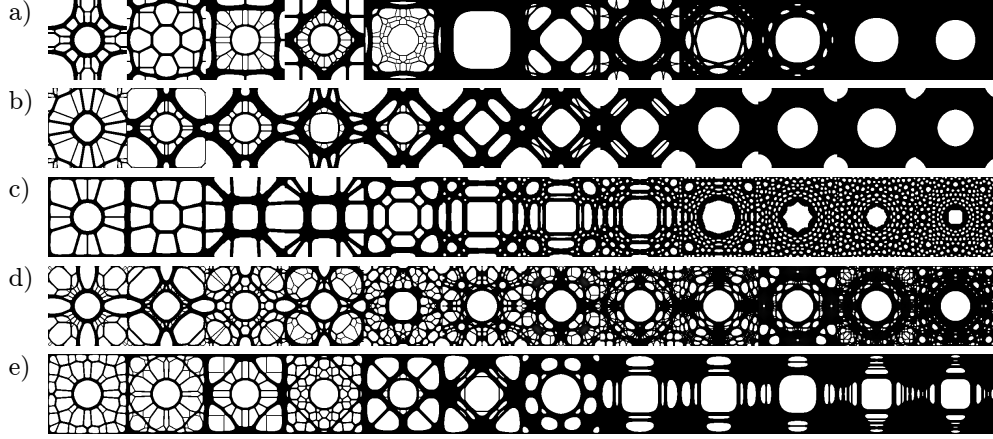
Fig. 2.5.: 2D FGMs optimized for maximum bulk modulus under linearly-varying volume fraction from 30% to 80% a) with $\omega = 0$; b) with $\omega = 1$; c) with local volume constraint ($\alpha = 95\%$, $R_e = 10$); d) with additional isotropy constraint; e) with mutual compatibility.

where r_e is the filter radius and the weighting factor $\omega_{i,e}$ depends linearly on the distance between elements, i.e.,

$$\omega_{i,e} = 1 - \frac{\|x_i - x_e\|_2}{r_e}.$$ (2.17)

The density filter is applied over the ordered sequence of unit cells in the GM, rather than within individual unit cells. This strategy has been used by Radman et al. [114]. This global filtering has the effect of reducing sharp features, and thus promotes smooth transitions at the boundaries between adjacent unit cells.

Projection

To ensure convergence to a binary (i.e. solid and void) solution, we use the parametrized projection function. The projected physical density is

$$\rho = \overline{\tilde{\phi}}_e = \frac{\tanh(\beta\eta) + \tanh(\beta(\tilde{\phi}_e - \eta))}{\tanh(\beta\eta) + \tanh(\beta(1 - \eta))}.$$ (2.18)

The parameter β controls the sharpness of the threshold function. To avoid instability, we use a parameter continuation starting with $\beta = 1$ and double its value at regular intervals. The parameter η is the projection threshold. Following the robust formulation proposed by Wang et al. [147], dilated ρ^d, intermediate ρ^i and eroded
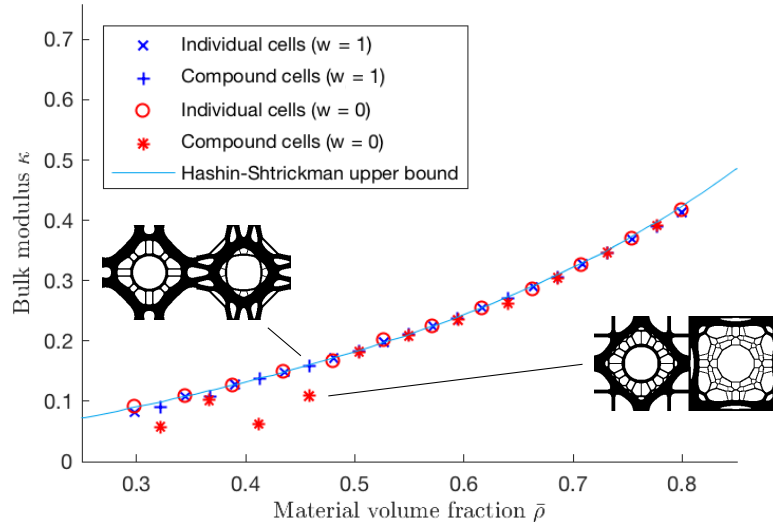
Fig. 2.6.: Bulk modulus vs. material volume fraction for FGM generated with ($\omega = 1$) and without ($\omega = 0$) compound formulation.

ρ^e designs are formulated using thresholds η, 0.5, and $(1 - \eta)$, with $\eta = 0.25$. This enforces a minimum length scale on both solid and void phases.

2.3 Results and Analysis

The proposed method has been implemented in Matlab based on the code developed by Xia and Breitkopf [161]. In this section, we present and analyze the results.

2.3.1 2D functionally graded materials (FGM)

A 2D FGM is optimized for maximum bulk modulus with linearly-varying volume fraction from 30% to 80%. The domain is discretized into 8 unique microstructures, each with 200×200 elements. Fig. 2.5 a) and b) compare results without ($\omega = 0$) and with compound formulation ($\omega = 1$).

The results confirm that the compound formulation ensures material connectivity between adjacent microstructures, particularly between the first and second and between the third and fourth cells, which are otherwise poorly connected. Moreover, the material transitions between adjacent cells are very smooth despite each microstructure exhibiting remarkably different topologies from one to another.

To assess the mechanical compatibility between adjacent structures, the bulk modulus for each individual and compound cell is plotted in Fig. 2.6, together with the theoretical Hashin-Shrickman (HS) upper bounds [59]. Several observations can be made from the results of the compound formulation. Firstly, the performance of the individual cells agrees well with the HS bounds, meaning that the optimization of connectivity does not compromise the optimality of individual cells. This can be attributed to the large design space in topology optimization. Secondly, the performance of compound cells is close to the theoretical limit. This contrasts the performance of those obtained via the reference formulation ($\omega = 0$), which are frequently inferior to those of either of their constituent microstructures.

2.3.2 FGM with maximum length scale

The formulation can be extended to allow control over the maximum length scale on the design. Together with the minimum length scale, this can reduce the variation in the thickness of the microstructures. We make use of the local volume constraint [156] to (approximately) control the maximum length scale. The constraint is formulated as:

$$\hat{\rho}_e \leq \alpha, \ \forall e, \tag{2.19}$$

where α is the prescribed upper bound on $\hat{\rho}_e$, which is the average element density in a neighbourhood $\mathbb{N}$ surrounding e, i.e.,

$$\hat{\rho}_e = \frac{\sum_{i \in \mathbb{N}_e} \rho_i}{\sum_{i \in \mathbb{N}_e} 1}. \tag{2.20}$$

The neighbourhood $\mathbb{N}_e$ is defined as the set of elements within an influence radius R_e of element e, i.e.,

$$\mathbb{N}_e = \{i| \ \|x_i - x_e\|_2 \leq R_e\}. \tag{2.21}$$

Figure 2.5 c) shows the effects of a maximum length-scale constraint. Here, besides prescribing a global volume fraction for each microstructure, a local volume bound ($\alpha = 95\%$) is also used. This constraint enriches the topology especially in the unit cells with a high volume fraction. The connectivity between unit cells of distinct topologies can be observed.

The bulk moduli of individual and compound cells optimized with and without a maximum length scale are plotted in Fig. 2.7. It can be observed that the bulk moduli in both settings agree well with the HS bounds. To the right of the plot (i.e., microstructures with high material volume fractions), the cells optimized with
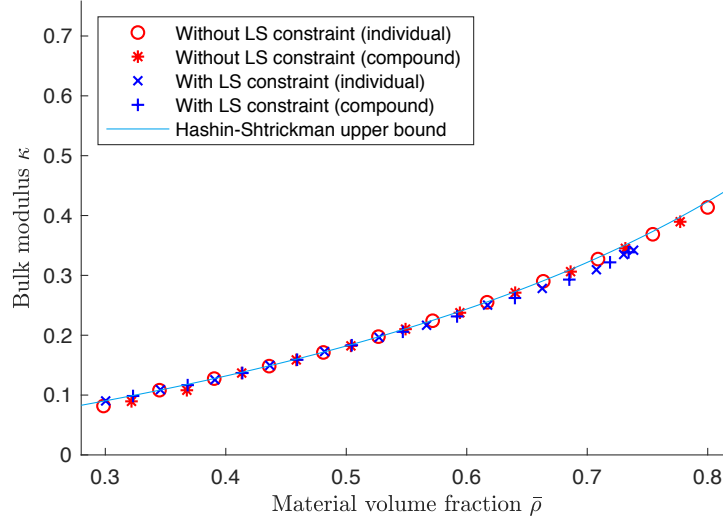
Fig. 2.7.: Bulk modulus vs. material volume fraction for the optimized FGM with/without a maximum length scale (LS).

this local constraint have a smaller global volume fraction than those without this constraint. This is due to the fact that local volume constraints are more restrictive. Similar effects have been reported in a study where local volume constraints were originally proposed for compliance minimization [156].

2.3.3 FGM for orthopaedic implant design

FGMs are extremely useful in the design of mechanical components with spatially-varying requirements. We apply the compound formulation to the design of an orthopaedic hip implant with high porosity on the bone-implant interface and high density in the core region. We include an isotropy constraint in the form of a cubic-symmetry constraint and an additional constraint on the stiffness tensor:

$$G_{11} + G_{22} - (G_{12} + G_{21}) - 4G_{33} = 0. \tag{2.22}$$

The isotropy constraint is included to reduce the sensitivity of the structure to loading conditions. The effects of the isotropy constraint are shown in Fig. 2.5 d). We also introduce a local volume constraint ($\alpha = 95\%, R_e = 10$), which limits the size of solid material regions, thus increasing the number and size of pores necessary for dendritic bone ingrowth.

We first optimize a set of 9 microstructures for maximum bulk modulus under linearly-varying volume constraint from 40% to 90%. Each cell is discretized into
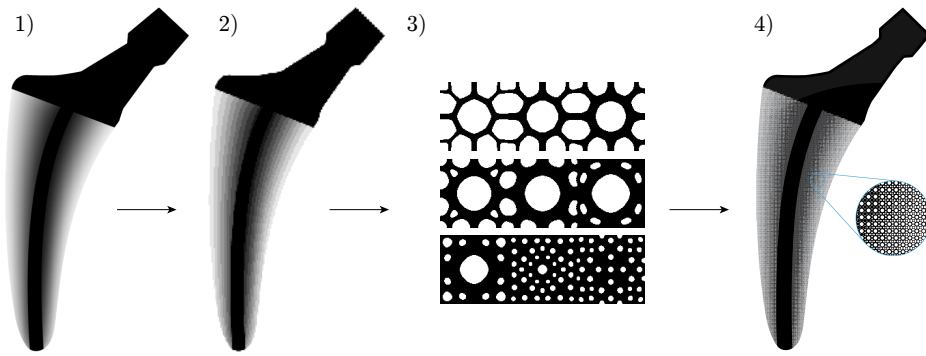
Fig. 2.8.: Implant development: 1) Define density distribution; 2) Discretize distribution; 3) Generate compatible microstructures; 4) Map microstructures into discretized density distribution.

100×100 finite elements. We then map the optimized microstructures into the implant to obtain the desired functional gradation. The process and final geometry are shown in Fig. 2.8. The 2D microstructures are extruded to obtain a 3D model. Fig. 2.9 shows a titanium specimen fabricated via selective laser melting.

A similar methodology can be applied to the design of infill patterns for 3D printing where spatially-varying structural requirements exist. In this case, the density distribution can be user-defined or determined based on the stress distribution. We then optimize a family of microstructures for maximum bulk modulus in a specific range of volume fraction and map them into the structure in the same way as for the orthopaedic implant.

2.3.4 Granularity

When mapping microstructures into a macrostructure for both FGM design and bottom-up multi-scale optimization (to be introduced in the next section), the discretization of a continuous density distribution introduces some error that is inversely correlated to the granularity of the discretization. It is therefore useful to be able to generate large families of microstructures. However, the computational effort required to simultaneously design a large number of unit cells may become problematic. Instead, an interpolation method can be used to break-up the problem into a series of more manageable ones. Firstly, a reduced set of uniformly distributed key unit cells is optimized. Subsequently, the intermediate unit cells between the key cells are optimized as smaller GMs with key cells set as fixed bounds and using
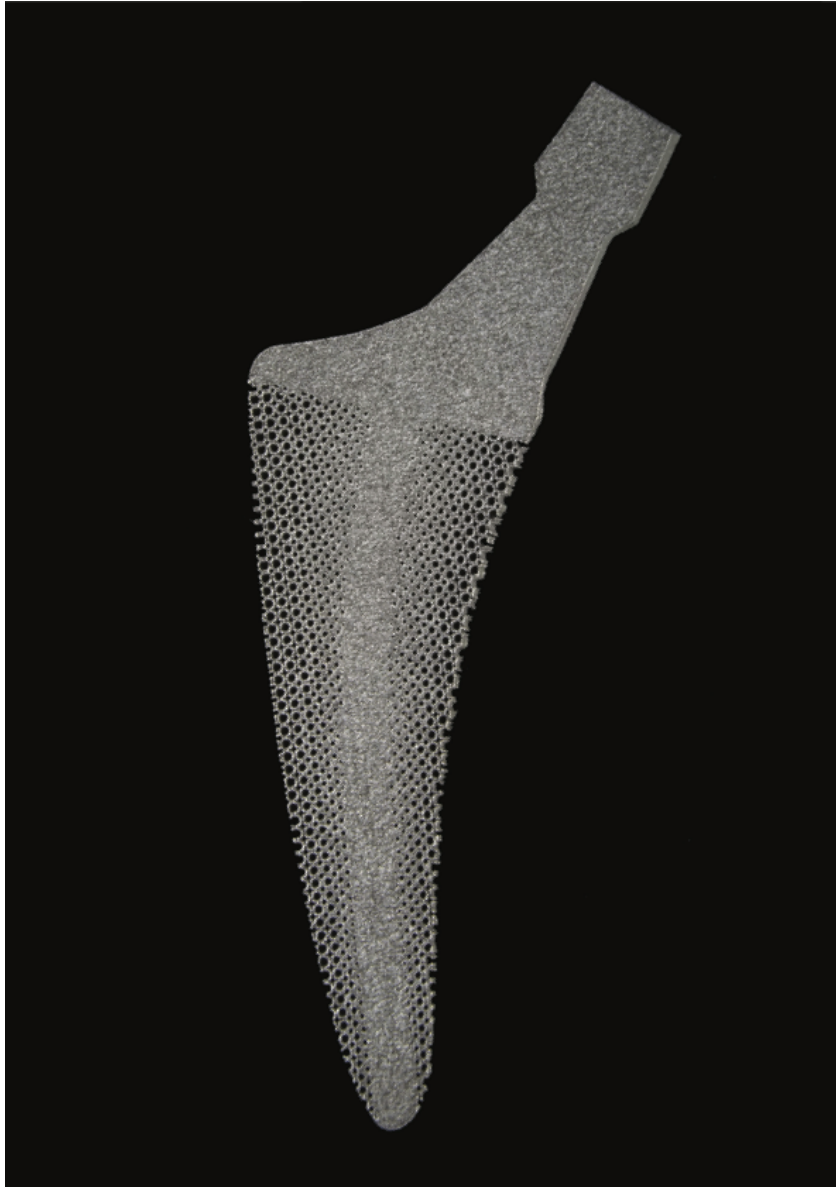
Fig. 2.9.: A specimen fabricated using selective laser melting (SLM). Material: Ti-6Al-4V ELI ASTM B348 with a particle size range of 10-45 micron. Machine: Realizer SLM125, Additive Manufacturing Laboratory, TU Delft.
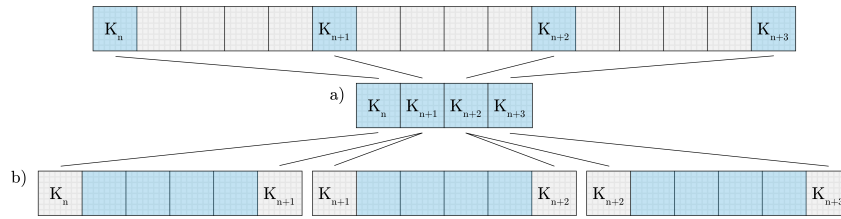
Fig. 2.10.: Interpolated GM optimization scheme. a) Key unit cells are optimized as a reduced GM. b) Intermediate unit cells are optimized as GMs with fixed key unit cells at either ends.
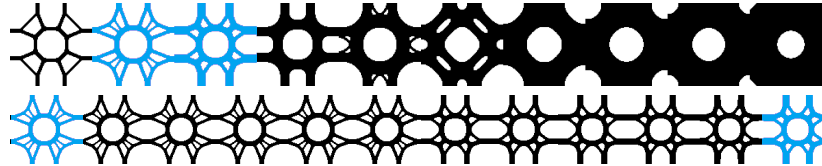
Fig. 2.11.: Key cell family (top) and interpolated cell family belonging to key cells two and three (bottom).

the key cells as an initial guess. Fig. 2.10 depicts the process graphically. A set of interpolated cells is shown in Fig. 2.11. As a reference, we also optimized the full granularity of 100 cells simultaneously. Fig. 2.12 compares the bulk modulus on the interpolated cells as depicted in Fig. 2.11. The bulk modulus of the interpolated cells is very close to that of the full-granularity optimized cells. For cells with low volume fraction, the difference in modulus is relatively large, but still less than 5%.

2.3.5 Full-scale analysis

Homogenization theory assumes the separation of scales [56]. In engineering however it is impractical to fabricate an infinite array of periodic microstructures. This leads to an unavoidable discrepancy in structural performance between homogenization-based analysis and a full-scale analysis on the non-infinite array of microstructures. To investigate this discrepancy, we set up a cantilevered beam made up of two microstructural regions, as shown in Fig. 2.13. Each microstructural region is discretized with $m \times m$ elements. In Fig. 2.13 a) each element is assigned with the homogenized properties, while in Fig. 2.13 b) each element is realized by the microstructural unit cell. Fig. 2.14 plots the normalized compliance regarding the resolution of the microstructural array. The normalized compliance is defined as the compliance obtained with homogenized properties over the compliance of the full-scale structure. As the resolution increases, the normalized compliance approaches 1. The error is within 5% with microstructural resolutions as low as
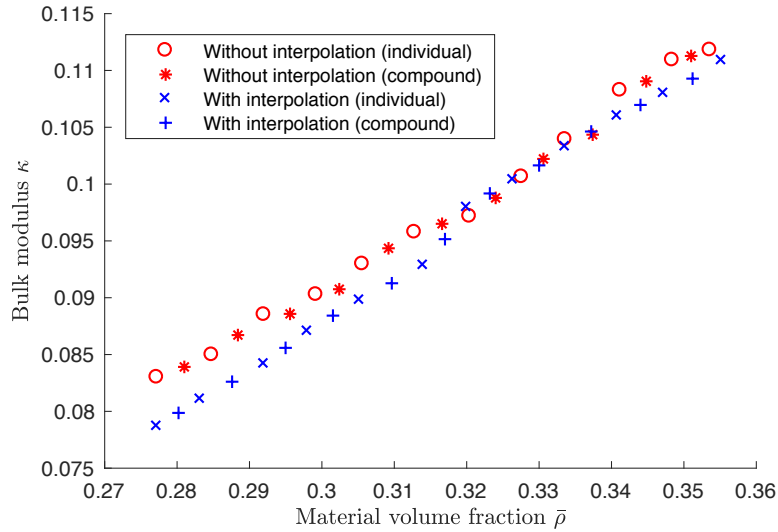
Fig. 2.12.: Bulk modulus vs. material volume fraction for cells optimized with and without the interpolation method.
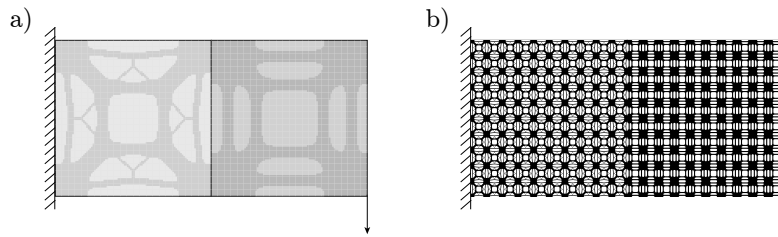
Fig. 2.13.: Cantilevered beam with two microstructural regions (50% and 60%): a) with homogenized properties assigned to each macro-scale element; b) full-scale structure with $m \times m$ microstructural unit cells for each macro-scale element.

18×18. In this example the two regions have a large difference (10%) in material fraction. This error becomes small as the difference in material fraction decreases. The full-scale analysis is performed using a multigrid-CG solver [3].

We compare this discrepancy with microstructures optimized without consideration for compatibility. The numbers are reported in Table 2.1. A resolution of 10×10 is used for both types of microstructures. It is observed that the compliance of a full-scale structure made up of incompatible microstructures is several orders of magnitude higher than predicted by numerical homogenization. In contrast, with the compound formulation ($\omega = 1$) the discrepancy is small.
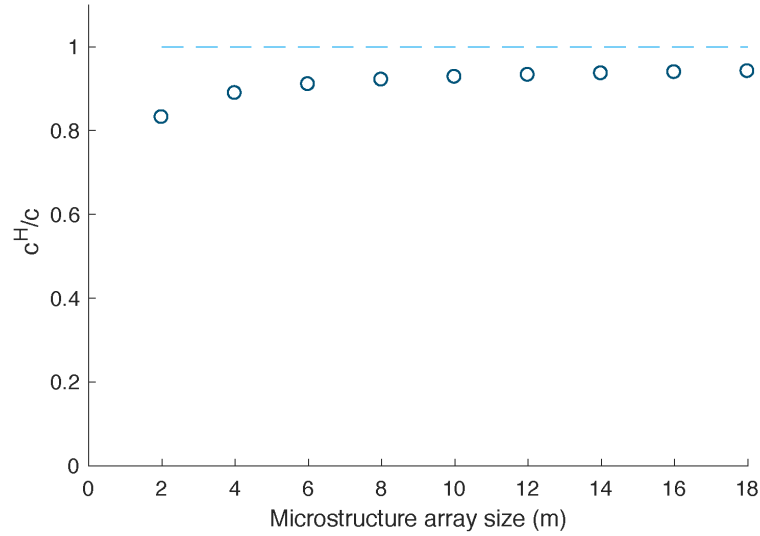
Fig. 2.14.: Normalized compliance vs. microstructural resolution.

	Homogenized	Full scale analysis
Individual formulation	2.436×10^2	1.899×10^8
Compound formulation	2.682×10^2	2.892×10^2

Tab. 2.1.: The structural compliance evaluated by homogenization and by full-scale analysis on the array of microstructures with and without consideration of compatibility.

2.4 Applicability to multi-scale Optimization

The proposed method for ensuring mechanical compatibility is also applicable to multi-scale optimization. Rather than developing a new multi-scale optimization framework, our intent here is to demonstrate the general applicability of the compound formulation for existing multi-scale frameworks. In particular, we demonstrate it on a bottom-up approach [33] and a concurrent approach [121].

2.4.1 Bottom-up multi-scale optimization

Following the method proposed by Cramer et al. [33], decoupled multi-scale optimization is performed by first generating a family of microstructures optimized for maximum bulk modulus under linearly-varying volume constraint, and subsequently fitting their properties to a functional which then replaces the SIMP model (Eq. 2.8) in the macro-scale optimization procedure.

This bottom-up approach is useful for some challenging loading conditions where density-based topology optimization methods do not converge to black-white solutions. Fig. 2.15 a) shows one such case. The beam is fixed at two ends, under a distributed load on the top and subject to a local volume constraint $\alpha = 60\%$. The density-based method [156] failed to produce binary structures and resulted in grey elements. Our method enables physically realizable microstructures to be mapped into such non-binary structures, shown in Fig. 2.15 b). Fig. 2.15 c) and d) show alternative binary microstructures for comparison. In Fig. 2.15 c) the graded microstructures are generated by adapting the thickness of an 'X'-shaped unit. Parametrized lattices have been commonly used (e.g. [149, 107, 85]). In Fig. 2.15 d) the graded microstructures are optimized with a density filter across the unit cell domains to promote connectivity, following the approach proposed by Radman et al. [114]. Using full scale analysis, the compliance of the microstructures generated by our method is smaller than the other two, and is close to the compliance using homogenized properties.

The compound formulation generates families of microstructures which are compatible with their nearest neighbours on either side. In order to use the resulting microstructures in a bottom-up multi-scale optimization procedure, the formulation has been modified to generate families of mutually compatible microstructures. In other words, each cell is compatible to any other cell in the family. The modified objective function for generating mutually compatible microstructures is:

$$
\max_{\rho} \quad J = (1 - \omega) \sum_{n=1}^{N} f(\overline{G}(\boldsymbol{\rho}^n)) +
$$
$$
\omega \sum_{n=1,m>n}^{N} f(\overline{G}([\boldsymbol{\rho}^n, \boldsymbol{\rho}^m])).
$$
(2.23)

As an example, Fig. 2.16 shows a sequence of microstructures generated with the original and modified compound formulation. In the latter case, non-adjacent microstructures possess improved compatibility with one another. The effects of the mutual compatibility are also shown in Fig. 2.5 e) for comparison to other options. This formulation increases the number of compound pairs from $N - 1$ to $\frac{N(N-1)}{2}$, and can impede convergence.

The elasticity tensor for linearly-varying volume constraint is fitted by a functional which replaces the SIMP model. The functional takes the form:

$$
G_{ij}^{fit}(\rho) = G_{ij}^0 \left(1 - \frac{1 - \rho}{1 + a_{ij}\rho}\right),
$$
(2.24)
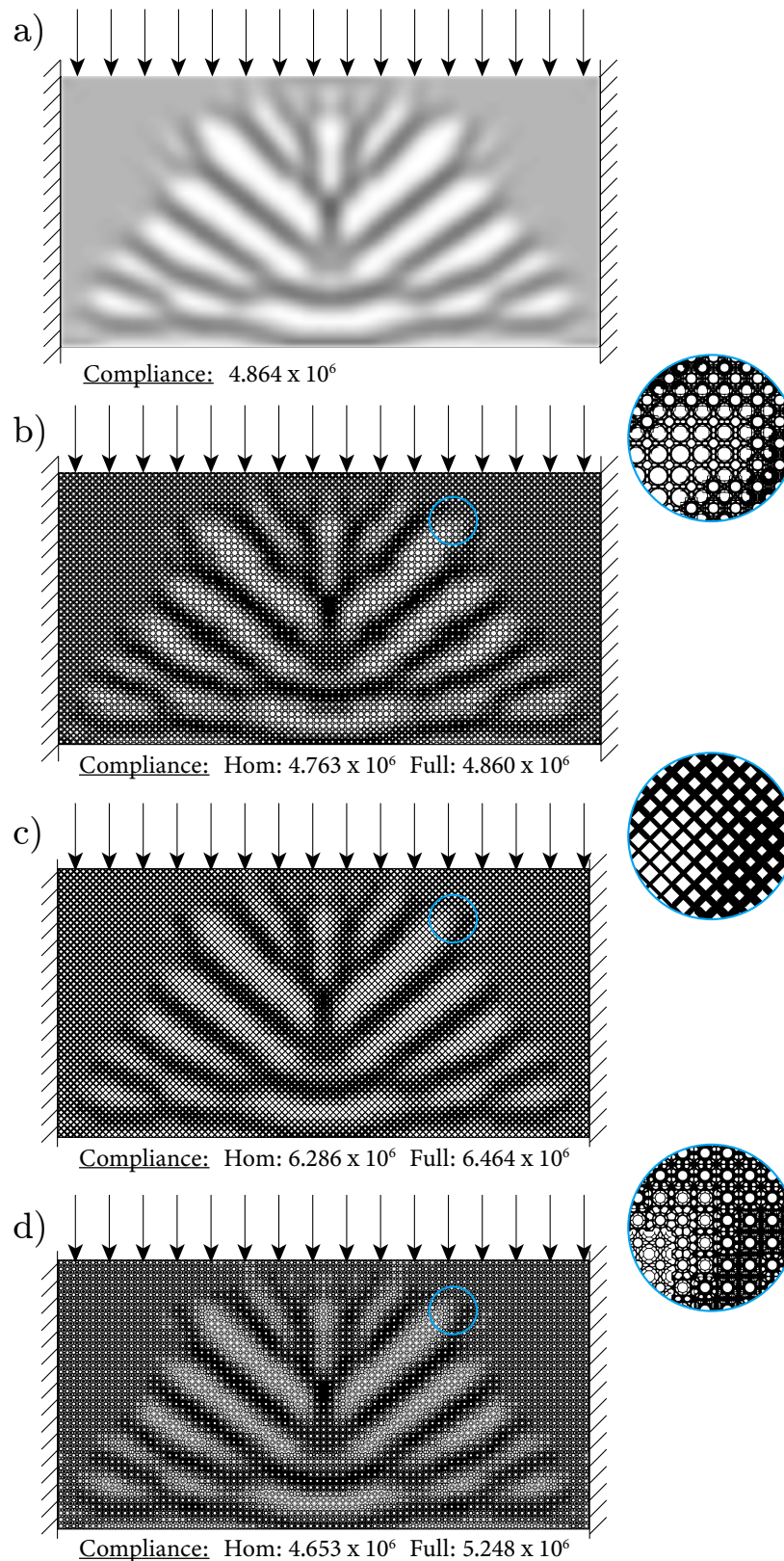
Fig. 2.15.: a) Non-convergent fixed beam under distributed load and subject to local volume fraction $\alpha = 60\%$. The binary structure can be realized by mapping b) compatible microstructures optimized by our method, c) 'X'-shaped lattices with varying thickness, and d) microstructures optimized by a density filter across the unit cell domains. For the binary structures, the compliances evaluated by homogenized properties (Hom) and by full scale analysis (Full) are reported.
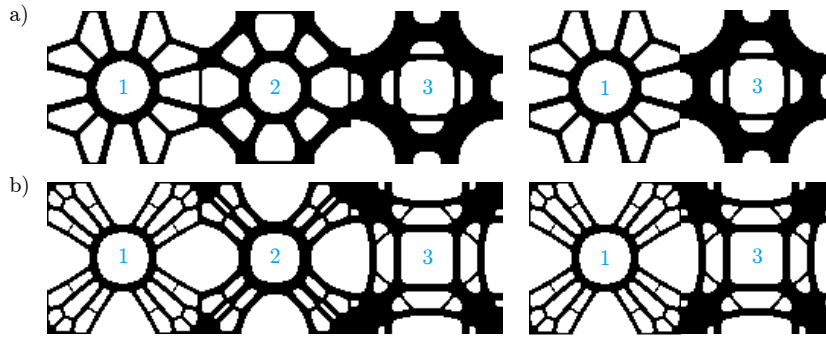
Fig. 2.16.: Sequence of microstructures generated: a) with compound formulation (Eq. 2.1), b) with modified compound formulation considering mutual compatibility (Eq. 2.23).
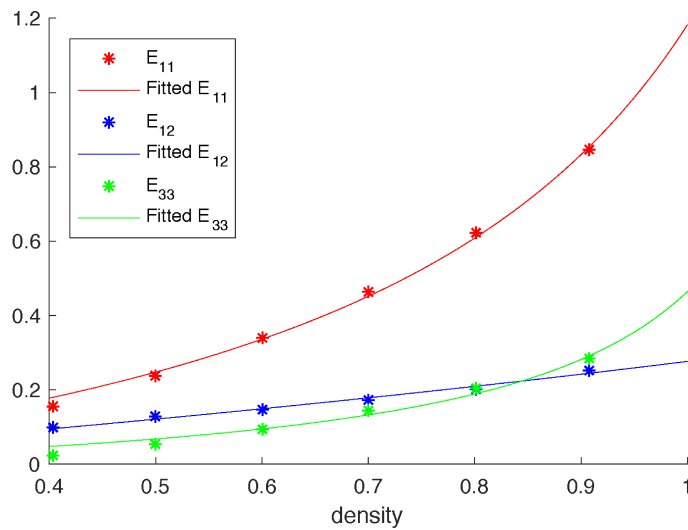
Fig. 2.17.: Fitted material property interpolation functions.

where G_{ij}^0 corresponds to a fully solid microstructure, and a_{ij} is the fitted coefficient. The functional matches the data very closely, and has the appropriate boundary values, i.e., $G_{ij}^{fit}(0) = 0$ and $G_{ij}^{fit}(1) = G_{ij}^0$ (see Fig. 2.17).

An isotropy constraint is imposed to ensure that the entries of the effective elasticity matrices vary monotonically with the average material density. Moreover, it reduces the number of parameters required to build the stiffness matrix from 6 (2D) or 21 (3D) to 2. This restriction reduces the computational cost of the optimization procedure, particularly for 3D implementations.

2.4.2 Concurrent multi-scale optimization

In previous sections, the compound formulation has been applied to the design of structures with a finite number of unique microstructures. This formulation can also be adapted for use in concurrent multi-scale optimization procedures, which typically result in an unlimited number of microstructures. We follow the hierarchical concurrent material and structure scheme proposed by Rodrigues et al. [121]. In line with the compound formulation, we update the homogenized macro-scale element stiffness tensor to be a weighted average of the element itself and a *super-element*, defined as the 3×3 (in 2D) Moore neighbourhood centred about the element, i.e.,

$$G_{ij}^{nm} = (1 - \omega)G_{ij}^{nm} + \omega G_{ij}^{n \pm 1, m \pm 1} \tag{2.25}$$

where n and m are the macro level element coordinates. Fig. 2.18 shows a simply supported beam with 45×24 macro-elements and 60×60 micro-elements, subject to a 30% material constraint, optimized for minimum compliance using the concurrent multi-scale scheme with and without the compound formulation. The boundary conditions are depicted in Fig. 2.18. The results show improved connectivity between adjacent microstructures and smoother topological gradation across the macro-structure. Furthermore, from multiple numerical tests it was observed that with the compound formulation the results are less dependent on the initialization of the design variables. Using full scale analysis it was observed that the improved connectivity reduces the compliance by more than four orders of magnitude. We note, however, that the compound formulation increases the homogenization-based compliance of the optimized structure by 28.8%. This could be explained by some distortion of the microstructures for ensuring compatibility. Moreover, even with improved connectivity there is a large discrepancy between the homogenization-based predictions and the results by full scale analysis.

2.5 Conclusions

In this chapter, we have presented a novel method to ensure mechanical compatibility among topology optimized microstructures. By optimizing the mechanical properties of the compound cells, together with the properties of the individual cells, our method generates microstructures that form an integral part. Our results show that the bulk moduli of individual cells reach the theoretical bounds predicted by the Hashin-Shtrikman model, meaning that the optimization of compatibility does not compromise the performance of individual cells. Furthermore, the bulk
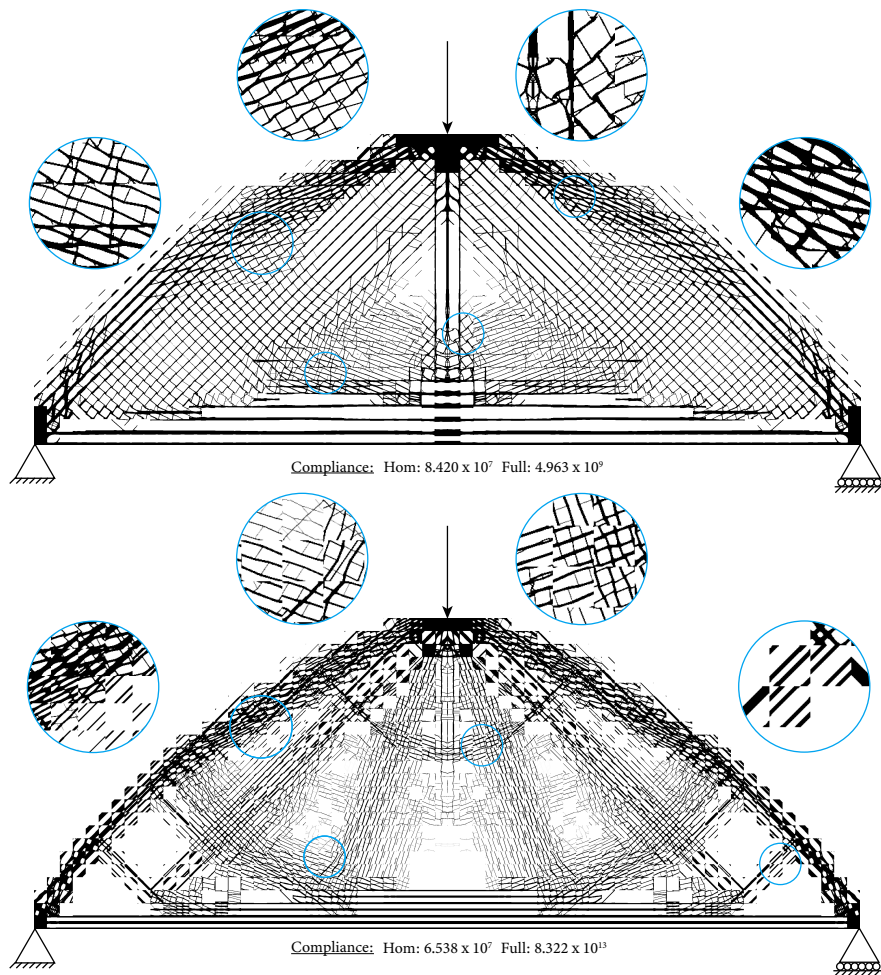
Fig. 2.18.: Multi-scale optimization of a simply supported beam subject to 30% volume constraint with $\omega = 0.9$ (top) and $\omega = 0.0$ (bottom). The compliance is evaluated using homogenized properties (Hom) and full scale analysis (Full). Better connectivity of microstructures and lower compliance (using full scale analysis) are observed in the top.

moduli of neighbouring pairs also agree well with the Hashin-Shtrikman bounds. The method has been extended to allow maximum length scale and isotropy in microstructures. In a number of designs, including functionally graded materials and multiscale structures, we have demonstrated the effectiveness of the proposed method. The optimized microstructures can be fabricated by additive manufacturing technologies.

As future work, we are particularly interested in the following aspects. Firstly, this method is directly applicable to 3D design problems. To alleviate the computational burden in 3D, the GPU-based topology optimization framework [158] can be used. Secondly, while we have applied the compound formulation for maximizing bulk modulus, its applicability to other physical problems such as conductivity [164] is left to be demonstrated.

Design optimization of 3D micro-architected implants

3

Abstract

Recent advances in 3D printable micro-architected materials offer unprecedented possibilities for the development of highly tailored orthopaedic implants. These devices, which are typically made from fully solid materials, significantly alter load transmission to the surrounding bone tissue, potentially leading to interface instability and bone resorption. In this work, we present computational methods to synthesize three dimensional (3D), patient-specific, implants with heterogeneous micro-architecture. Our method simultaneously minimizes the risks of load-induced interface fracture and peri-prosthetic bone remodelling, while taking into account functional and manufacturing constraints.

We first develop a novel parametric micro-architecture with desirable functional attributes and a wide range of effective mechanical properties, including both positive and negative Poisson's ratios. We then present formulations which optimize the spatial configuration of micro-architecture parameters in order to simultaneously minimize the risk of load-induced interface fracture and post-operative bone remodelling. To that end, a novel bone remodelling objective is devised, taking into account both bone apposition and resorption, predicted via a model based on strain-energy density. The interface fracture objective is defined as the maximum value of the multi-axial Hoffman failure criterion along the interface.

The procedure is applied to the design of 3D titanium hip implants with prescribed conventional geometries and compared, in silico, to both a conventional solid implant and a homogeneous low-stiffness lattice design. The optimized implant

results in a performance improvement of 64.0% in terms of bone remodelling, and 13.2% in terms of interface fracture risk, compared to a conventional solid implant design.

3.1 Introduction

New developments in the fields of additive manufacturing and micro-architected materials offer an opportunity to produce mechanical components with unprecedented geometric complexity. This design freedom, in turn, enables engineers to design components which greatly outperform their conventionally engineered counterparts. However, the design of these new micro-architected components requires a thorough understanding of the use context, as well as the development of novel computational methods. In this work, we present multi-objective optimization methods for the design of orthopaedic hip implant stems in an effort to improve their longevity and avoid the need for complicated revision surgeries. We demonstrate the superior performance of these optimized designs over conventional solid and uniform lattice designs in silico, via finite element analysis.

Orthopaedic implant stems used in total hip arthroplasty (THA) are typically fully solid and made from engineering materials, such as titanium alloys, stainless steel, chromium alloys, or tantalum. These materials have been selected for their high strength, relatively low density, corrosion resistance, and biocompatibility. Although considerable strides have been made towards improving long-term implant fixation and osseointegration, 15% of THA patients undergo revision surgery within 10 years, of which over half are required within the first 5 years [120, 81]. Revisions are more complex due to degradation of the peri-prosthetic bone tissue and represent a four-fold increase in failure risk, compared to the original procedure [111]. Although patient-related medical factors play a role in bone resorption, mechanical, rather than medical factors are believed to be responsible for most bone-related implant failure [77]. From a mechanical perspective, two main factors contribute to peri-prosthetic bone degradation: *inadequate stress transmission to the bony tissue,* and *inappropriate stress conditions along the bone-implant interface.*

Orthopaedic implants are typically made from much stiffer materials (100-200 GPa) [21] than the relatively compliant bone tissue (14.8-20.7 GPa) [98]. As a result of this mismatch, much of the loads applied to the implant are not transmitted to the surrounding bone tissue. This phenomenon, known as stress shielding, triggers bone remodelling, which is an adaptive process through which bone is deposited

or resorbed based on local stress conditions [63]. Over time, the reduced stress conditions result in significant bone resorption. This phenomenon, termed bone loss secondary to stress shielding, can lead to serious complications, such as aseptic loosening, chronic pain, and peri-prosthetic fracture.

In the last few decades, numerous strategies have been proposed to reduce stress shielding. A common approach has been to reduce the difference in stiffness between the implant and bone tissue. Means to achieving that end fall into two categories: modification of the implant geometry and the use of low-stiffness materials. Geometric modifications include alteration of the implant cross-section [35, 122, 13], stem length reduction [22, 100, 119], stem hollowing [125, 55], and the addition of anchors, collars or grooves [35, 54, 13]. Material modifications include the use of polymeric composites or porous metals [65, 136, 126], metallic foams [154, 94], and cellular structures [42]. However, the introduction of softer materials has the undesired effect of increasing the risk of interface failure by producing considerably higher tensile and shear stresses [44, 126]. Fracture of the relatively weak interface leads to aseptic loosening, alters load transmission to the surrounding bone tissue and produces wear particles, which can lead to bone resorption and further aseptic loosening [26].

Kuiper and Huiskes were first to identify the conflict between stress shielding and interface instability. In their seminal work, they introduced the notion of an implant with spatially-varying mechanical properties and proposed a multi-objective optimization strategy which was successful in reducing both stress shielding and the risk of stress-related interface fracture. Their work, however, was limited to the optimization of a coarse 2D model and considered only the macro-scale problem [79, 80]. Arabnejad and Pasini extended upon their idea by additionally considering the micro-scale detail, making use of genetic algorithms to improve the design of a 3D-printable implant with parametric micro-architecture [8]. Other contributions have mostly focused on the stress shielding aspect. Some authors have proposed metrics to quantify bone resorption or stress shielding, while others have used compliance as a surrogate [60, 46, 149]. These methods have proven successful in reducing stress shielding, but suffer from a number of shortcomings (e.g., regarding sensitivity to tuning parameters, which will be further discussed in the methodology section).

In industry, despite early concerns regarding fatigue failure [71], porous materials, such as metallic foams [94, 154], porous tantalum [11] and open-cell porous coatings [42] are gaining traction. Their structure allows for increased bone ingrowth and interface strengthening. However, their success is strongly dependent

on pore size, porosity and mechanical conditions – factors which can be difficult to control independently of one another [145, 51, 41]. Instead, recent advances in additive manufacturing technologies, such as selective laser sintering (SLS), selective laser melting (SLM), and electron-beam melting (EBM), have enabled the precise fabrication of functional components with ultra-fine detail using advanced engineering materials, such as titanium alloys and stainless steel [117]. These advances are expected to enable the fabrication of implants with custom micro-architecture, offering extremely precise control over the porosity, pore size, and mechanical properties [110, 141, 99, 165].

To take full advantage of the newly expanded design space, however, efficient computational methods are critical. Until now, studies have been limited to a small number of design variables and relatively coarse finite element discretization. These concessions were necessary due to the high computational costs associated with the proposed optimization strategies. On the other hand, in the field of topology optimization, gradient-based non-linear optimization strategies, such as the method of moving asymptotes (MMA) [144], as well as efficient finite element solvers, such as multi-grid preconditioned conjugate gradient [3, 158] have been specifically designed to handle finite element analysis problems with thousands or millions of design variables, facilitating the timely solution of large 3D optimization problems on a standard PC. These methods can be applied to the design of multi-scale structures with both micro-scale and macro-scale considerations [32, 160, 34, 150, 48]. We refer to a recent review article for an overview of multi-scale topology optimization methods [159].

In this work, we propose a gradient-based numerical optimization methodology to automatically synthesize 3D micro-architected implants that simultaneously minimize 1) the risk of interface fracture and 2) implant-induced bone remodelling. The procedure decouples the micro-scale unit-cell geometry from the macro-scale design problem, allowing for the efficient inclusion of manufacturing and/or application-related constraints, while significantly reducing the computational costs compared to concurrent multi-scale strategies. In addition, we propose performance metrics which, we argue, more accurately represent the design objectives than in prior publications. We validate our method by comparing the optimized design, in its full micro-architectural detail, with a solid implant and one with uniform lattice.

The remainder of this chapter is organized as follows. We first present an overview of the design methodology. Next, we describe the parametric micro-architecture. This is followed by an explanation of the optimization objectives and constraints. Finally, the optimization strategy is applied to the design of 3D hip implant stems under
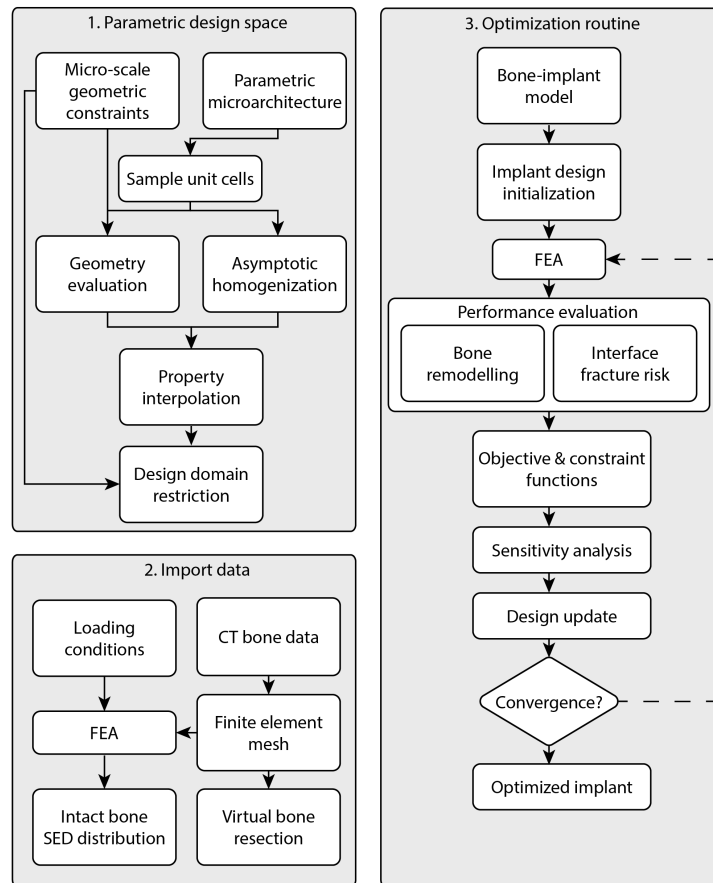
Fig. 3.1.: Flow chart illustrating our approach for the design of micro-architected material (1), initialization (2) and optimization (3) procedures.

multiple loading conditions, the results of which are summarized and discussed in detail.

3.2 Methodology

The structure of our three-stage method is presented in Fig. 3.1. In stage 1, a parametric micro-architecture is defined and evaluated via numerical homogenization to extract its effective properties. In stage 2, the macro-scale implant design problem is formulated based on patient-specific bone data. In stage 3, the implant optimization problem is solved using the design space defined in stage 1. This section provides detail on each stage.

3.2.1 Parametric micro-architecture

The first stage of our implant design method involves the definition and characterization of a parametric micro-architecture for use in a decoupled multi-scale optimization formulation. In such a formulation, the micro-scale architecture design is decoupled from the macro-scale optimization. This approach reduces computation costs, but introduces the possibility of poor compatibility between adjacent unit cells with different micro-architecture. A number of strategies have been proposed to address these issues, though these methods tend to incur significant computation cost [169, 151, 87, 40, 48, 159]. Instead, we introduce a parametric micro-architecture, such that adjacent cell compatibility and smoothly varying geometric properties can be ensured at a negligible computational cost.

To be suitable for use with our implant optimization formulation, the parametric micro-architecture must be able to produce a wide and smoothly varying range of mechanical properties. Moreover, it must possess adjacent cell connectivity and open-cell porosity, and must be suited to additive manufacturing. To these ends, we propose a generalization of the well-known cubic anti-chiral topology. It possesses the required attributes and can produce both positive and negative (auxetic) Poisson's ratios, a rare feature which has been recently utilized in the design of hip implant stems [76, 52].

The generalized cubic anti-chiral topology, shown in Fig. 3.2 and Fig. 3.3, is characterized by a set of identical sinusoidal curves with amplitude a and diameter d, both defined as a fraction of the unit cell side-length. For small diameter values, negative values of a correspond to the familiar auxetic structure, while positive values of a correspond to a different structure resembling close-packed spheres, and results in positive Poisson's ratios ν, greater than that of the base material ν_0. Note that the curves are at 45° from the principal planes to ensure that the mechanical properties are identical in the principal directions. Parameter a is, in fact, the amplitude projected onto the face of the cubic bounding box, as shown in Fig. 3.3. The diameter parameter, d, controls the effective elastic modulus. By tuning these two parameters within the design space, a wide range of mechanical properties can be achieved. The aforementioned design space is defined to ensure a non-overlapping geometry, which can be written as $4a - 2d \leq 1$. If additional geometric constraints are imposed, the design space is reduced accordingly. For each additional constraint, values are computed for a set of sample micro-architecture. From there, a binary mask Φ_c is generated and applied to the original design space Φ:

$$\Phi_{constrained} = \Phi \cap \Phi_{c_1} \cap ... \cap \Phi_{c_m} \tag{3.1}$$
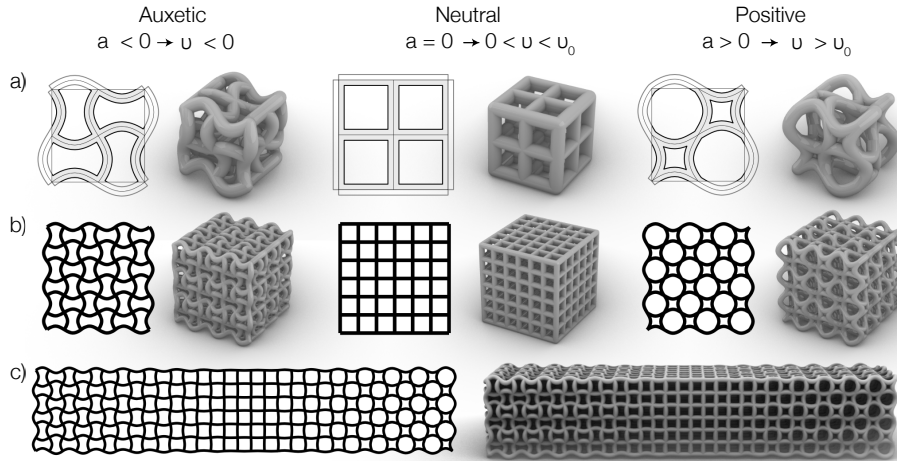
Fig. 3.2.: Generalized parametric cubic anti-chiral micro-architecture: a) Sample unit cells exhibiting negative, neutral, and positive Poisson's ratios; b) Periodic arrays of unit cells c) A functionally graded assembly of chiral micro-architectures exhibiting ideal interface connectivity. The left-hand side illustrations refer to the 2D version of the structure, while the right-hand side illustrations refer to the 3D version shown in Fig. 3.3, and used throughout this work.

where Φ_{c_i} is the binary mask associated with constraint i, and m is the number of added constraints. This method allows for the inclusion of any number of geometry-related constraints, without incurring additional computational cost. Fig. 3.4 shows the original and reduced design spaces when maximum effective density and minimum length scale are imposed.

In order to facilitate an efficient optimization procedure, we do not represent the implant in its full micro-architectural detail. Instead, we take advantage of the quasi-periodic nature of our structure and employ asymptotic homogenization (AH) to
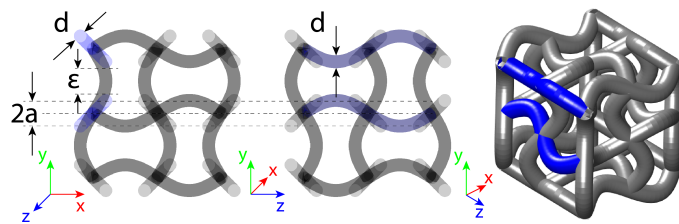
Fig. 3.3.: An illustration of the 3D cubic anti-chiral micro-architecture, shown in the front, side, and isometric views, including the geometric design parameters a and d. ϵ represents the clearance between adjacent wave forms. The highlighted blue wave forms on the right correspond to the highlighted blue out-of-plane wave forms on the left.
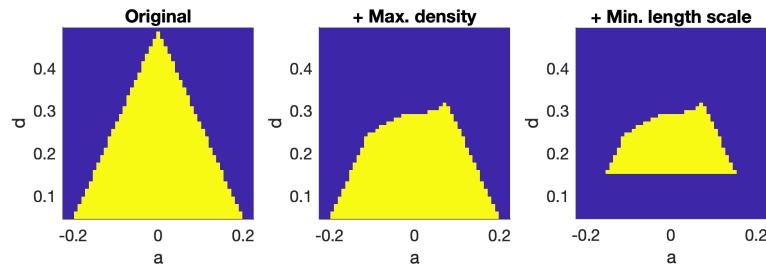
Fig. 3.4.: Design space Φ without constraint (left), including maximum density constraint (middle), including maximum density and minimum length scale constraints (right).

map from each geometric parameter combinations to a corresponding homogenized elasticity tensor.

In many cases, multi-scale approaches involve repeated AH of each micro-architecture, for every design iteration. This costly procedure is necessary when the micro-architecture topology is not prescribed. In this case, however, re-evaluation via AH can be avoided by characterizing the entire space of possible geometric parameter combinations prior to optimization. To that end, we evaluate a set of 1600 representative volume elements (RVE) spanning the range of geometric properties. Samples were discretized using between $60 \times 60 \times 60$ and $100 \times 100 \times 100$ hexahedral finite elements and homogenized using the method described in [39]. The higher resolution was used for samples with small d values, in order to ensure mesh independence. This procedure was performed in ~ 100 hours on a standard PC with a 2.6 GHz 6-core Intel i7 CPU. From there, cubic interpolation is used to capture the relations between the geometric and mechanical properties. The effective properties for any feasible parameter combination can be obtained by simple interpolation, rather than expensive AH. The fitted functions mapping the geometric parameter combinations to the effective elastic modulus, Poisson's ratio, and shear modulus are shown in Fig. 3.5, each normalized with respect to the elastic modulus of the bulk material.

3.2.2 Finite element model

The bone geometry and density information used in this work is that of a 28 year old healthy male patient, obtained via computational tomography (CT) and retrieved from the embodi3D database [68]. The CT data is projected onto the finite element mesh, along with the density information. The bone boundaries are then extracted using the marching cubes algorithm, and used to enrich the finite element model, according to the extended finite element method outlined below. The original and
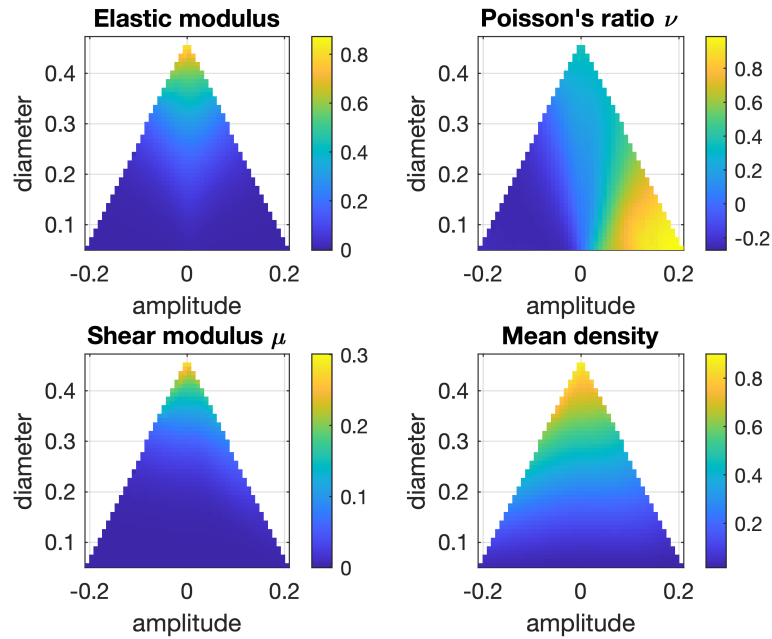
Fig. 3.5.: Normalized mechanical properties obtained via asymptotic homogenization and fitted using cubic surface interpolation.

resected bone meshes are shown in Fig. 3.6, along with the density information. The loading conditions are based on the walking and stair climbing profiles described in [62], with slight modifications to fit the bone model (see appendix for details). Note that in this work, the implant is not preloaded, as it would be when press-fitted into place. This simplification most likely causes an overestimation of the interface fracture risk and bone resorption. As a result, the optimized design's predicted performance will be somewhat conservative.

The bone-implant system is represented on a $158 \times 158 \times 210$ mm fixed grid with $2 \times 2 \times 2$ mm trilinear hexahedral elements using an extended finite element method (XFEM). The XFEM model captures discontinuities in the displacement field by enriching a set of nodes along the interface with additional degrees of freedom (DOF) and interpolating them with discontinuous shape functions. This allows for a more accurate representation of the physical geometry and captures discontinuities in the displacement, strain, and stress fields. Both features improve the accuracy of interface stress predictions over standard fixed grid methods, while maintaining low computational costs. For completeness, the XFEM procedure is briefly introduced here.

According to the XFEM strategy, elements which are cut by a material interface are enriched with additional degrees of freedom. Specifically, each DOF associated with a node belonging to a cut element is duplicated. The added DOF is associated with a
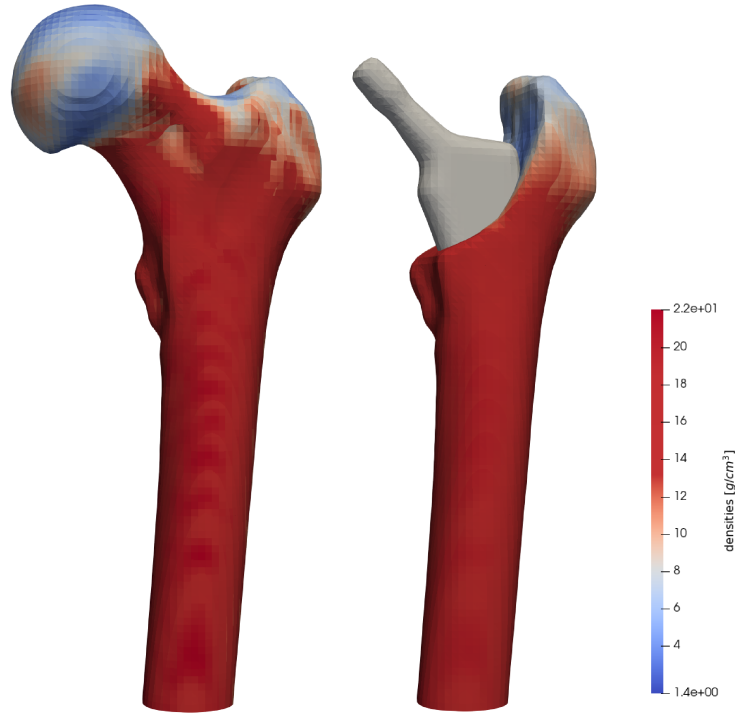
Fig. 3.6.: Original (left) and resected (right) bone geometries, and density distributions, projected to the extended finite element mesh.

discontinuous shape function, thus enabling discontinuities in the displacement field. The displacement $\mathbf{u}(\mathbf{x})$ at any point $\mathbf{x}$ on either side of the interface is obtained from the standard and enriched element DOF solutions $\mathbf{a}$ and $\mathbf{b}$:

$$\mathbf{u_e}(\mathbf{x}) = \sum_{i \in D} N_i(\mathbf{x})\mathbf{a}_i + \sum_{j \in \Gamma} \nu(\mathbf{x})N_j(\mathbf{x})\mathbf{b}_j \tag{3.2}$$

where N_i and N_j are the conventional shape functions. The enrichment function $\nu(\mathbf{x})$ is here defined as

$$\nu(\mathbf{x}) = H(\phi(\mathbf{x})) - H(\phi(\mathbf{x}_j)) \tag{3.3}$$

in which $\phi(\mathbf{x})$ is the level set function equal to zero along the interface Γ, $\mathbf{x}_j$ is the coordinate of node j, and $H(\phi(\mathbf{x}))$ is the Heaviside function of the level set ϕ at coordinate $\mathbf{x}$. This second order discontinuous shape function captures the discontinuities of the strain field, assuming a perfectly bonded interface. A detailed description of the XFEM strategy can be found in [97].
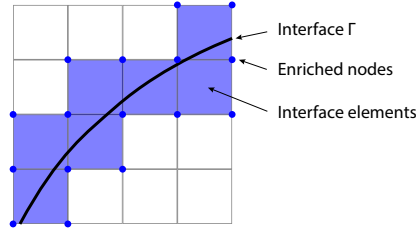
Fig. 3.7.: XFEM enrichment along material interface

3.2.3 Bone remodelling

To assess the performance of an implant design, we consider two main failure mechanisms: failure at the interface due to inappropriate stress conditions, and excessive bone resorption due to stress shielding. Bone loss can be most accurately predicted via a bone remodelling simulation. However, these simulations involve computationally intense iteration. Instead, a number of alternative formulations have sought to approximate bone loss by considering the stress conditions immediately before and after THA. Kuiper and Huiskes proposed to count up the amount of bone which is locally under-stressed [79]. Specifically,

$$m_r(\mathbf{b}) = \frac{1}{M} \int_V g(S(\mathbf{b}))\rho dV \tag{3.4}$$

where M and V are the original bone mass and volume, respectively, and $g(S(\mathbf{b}))$ is a resorptive function equal to unity if the local strain energy density S is below a certain threshold, defined in terms of the original strain energy density S_{ref}. This function, though commonly referenced and employed in the literature [8, 73], suffers from a vulnerability. Since it does not differentiate between a slightly under-loaded and an extremely under-loaded local stress condition, the optimization routine cannot prioritize one over another. Moreover, this function is highly sensitive to the choice of threshold value and may incorrectly evaluate the quality of an implant under certain conditions. For instance, a design for which a slight under-loading exists throughout the bone would be considered poorer than a design for which extreme bone loss is predicted only in the peri-prosthetic region. The second design is far more likely to cause implant failure. Yet, the model favours it over the first.

Another commonly-used bone loss prediction function is called "Stress Shielding Increase" (SSI) [46, 124]. In this model, the von Mises stresses are computed before

and after THA. SSI is defined as the relative difference between the two, averaged over a specified region.

$$SSI = \frac{\langle \sigma_{VMS}^{pre-THA} \rangle - \langle \sigma_{VMS}^{THA} \rangle}{\langle \sigma_{VMS}^{pre-THA} \rangle} \tag{3.5}$$

where $\sigma_{VMS}^{pre-THA}$ and σ_{VMS}^{THA} are the von Mises stresses in the femur before and after THA and

$$\langle \sigma_{VMS}^{pre-THA} \rangle = \frac{1}{\sum_e V^e} \sum_e \int_{V^e} (\sigma_{VMS}^{pre-THA})^e dV$$
$$\langle \sigma_{VMS}^{THA} \rangle = \frac{1}{\sum_e V^e} \sum_e \int_{V^e} (\sigma_{VMS}^{THA})^e dV \tag{3.6}$$

are the averages of the stress over a set of elements. This formulation outputs performance values for each element set. However, it is unclear how a single overall performance value would be defined for use in an optimization setting. Furthermore, the choice of domain segmentation would likely affect results. In the extreme, with a single domain, the function looses all local information. On the other hand, in the case of single-element domains, the function becomes highly susceptible to finite-element-related instabilities and numerical rounding errors, especially in cases where stress values approach zero.

In addition to the above-mentioned issues, both formulations ignore the effects of local stress over-loading. Over-loading can induce bone formation which alters the stress distribution along the bone-implant interface, potentially destabilising the implant. Moreover, severe over-stressing can cause stress fractures which can cause chronic pain and generally weaken the bone-implant system [115, 28].

We present an alternative function which aims to address the above-mentioned issues. This approach takes into account both bone resorption and bone apposition, as well as their relative magnitudes. In this way, the algorithm aims to minimize all bone remodelling, and prioritizes areas in which greater remodelling is predicted.

The well-established bone remodelling algorithm, proposed by Huiskes and Weinans, defines the predicted change in bone density in a given time step as a piece-wise function based on the local strain energy density [66]. For values below a certain threshold, bone loss is predicted, and for values above the threshold, bone apposition

is predicted. Additionally, a stable region is defined, for which no net remodelling is predicted. Formally stated, the bone remodelling $\frac{\partial \rho}{\partial t}$ in time step t is defined as:

$$\frac{\partial \rho}{\partial t} = \begin{cases} C_1(\Xi_t - k(1+s))^m & k(1+s) < \Xi_t \\ 0 & k(1-s) \leq \Xi_t \leq k(1+s) \\ -C_2(k(1-s) - \Xi_t)^n & \Xi_t < k(1-s) \end{cases} \quad (3.7)$$

where Ξ is the local strain energy density, k is the stable strain energy density, often chosen as the original pre-THA value, s is a threshold defining the stable zone, C_1, C_2, m and n are constant tuning parameters. In practice, normalized densities are constrained to values between $[\rho^{min} \rho^{max}]$. This introduces discontinuities, as shown in Fig. 3.8 (left). As a result, the function is non-differentiable along the density extrema, which can cause convergence problems in a gradient-based optimization routine. To remedy this issue, a minor modification is proposed:

$$\frac{\partial \rho}{\partial t} = \begin{cases} C_1(\rho^{max} - \rho_t) \cdot (\Xi_t - k(1+s))^m & k(1+s) < \Xi_t \\ 0 & k(1-s) \leq \Xi_t \leq k(1+s) \\ -C_2(\rho_t - \rho^{min}) \cdot (k(1-s) - \Xi_t)^n & \Xi_t < k(1-s) \end{cases} \quad (3.8)$$

The added factors $(\rho^{max} - \rho_t)$ and $(\rho_t - \rho^{min})$ smoothly constrain the density ρ_t to specified maximum and minimum values ρ^{max} and ρ^{min}, thereby eliminating the discontinuities, without affecting the general behaviour of the model. In this work, the following constant values were used: $k = \Xi_{unresected}$, $s = 0$, $C_1 = 10^{-2}$, $C_2 = 1$, $m = n = 1$, $\rho^{min} = 0.1$, $\rho^{max} = 1$.
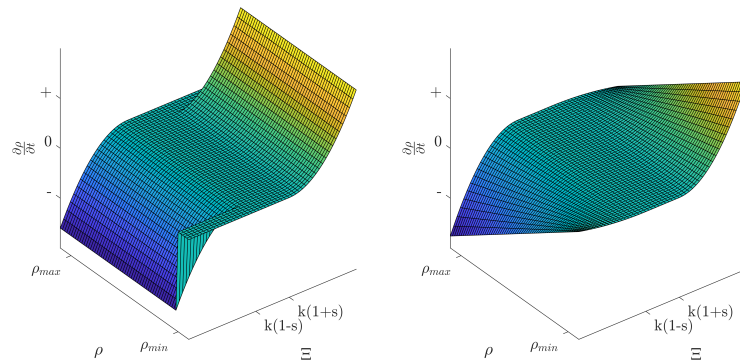
Fig. 3.8.: Original (left) and augmented (right) Huiskes bone remodelling algorithms described in Eq. 3.7 and Eq. 3.8

The bone remodelling objective is defined as the sum of the unsigned changes in bone density throughout the bone, in the first iteration:

$$F_r = \int_V \left| \frac{\partial \rho}{\partial t} \right|_{t=0} dV \tag{3.9}$$

where V is the bone domain. We note that in the tuning parameters C_1, C_2, m and n, which were originally intended to ensure accuracy in the bone remodelling simulation, can instead be used to prioritize bone resorption over bone apposition, if desired. This formulation, provides a robust and flexible way to evaluate and optimize performance in terms of bone remodelling.

3.2.4 Interface fracture risk

The second failure mechanism considered in this work is interface fracture due to inappropriate stress conditions along the bone-implant interface. In cementless THA, no adhesive material is used to fixate the implant. Instead, press-fitting and eventual bone ingrowth stabilize the implant. In this context, inappropriate stress conditions can impede bone ingrowth and create wear particles by inducing micro-motions along the interface. Prior works have demonstrated that when the interface fails, fracture tends to occur within the brittle bone tissue [31, 38]. It is therefore appropriate to estimate the risk of failure via an orthotropic brittle material model such as the Tsai–Wu failure criterion or the elliptic multi-axial Hoffman failure criterion (HFC) [64]. This latter model defines the local failure risk as an elliptic function of the normal stress σ and shear stress τ:

$$f_H(\sigma, \tau) = \frac{1}{S_t S_c} \sigma^2 + \left(\frac{1}{S_t} - \frac{1}{S_c} \right) \sigma + \frac{1}{S_s^2} \tau^2 \tag{3.10}$$

where S_t, S_c, and S_s are the local strengths of the material in tension, compression and shear loading, respectively. These strengths are defined as a function of local material density, according to a power law.

$$S_x = a_x \cdot \rho^b \tag{3.11}$$

Here, $a_t = 2.63$, $a_c = 8.29$, $a_s = 6.60$, and $b = 1.65$ [142].

The global interface risk function is defined as the p-norm of local risk measured over the interface. For lower p values, the function approaches the set mean, whereas for high p values, the function approaches the set maximum. In this work, $p = 12$.

$$F_\sigma = ||\{f_H(\sigma, \tau)\}||_p \tag{3.12}$$

3.2.5 Multi-objective optimization

In this section, we formulate a multi-objective optimization problem in which the goal is to find an implant design which simultaneously minimizes the bone remodelling and interface fracture risk functions. The implant is assumed to be a quasi-periodic arrangement of cubic anti-chiral unit cells, the geometric parameters for which will serve as design variables.

The two objectives are aggregated into a single global objective via linear scalarization:

$$F = w_\sigma \cdot F_\sigma + w_r \cdot F_r \tag{3.13}$$

where w_σ and w_r are weighting factors. In this work, the weights are chosen such that the weighted components of the objective are equal prior to the optimization. This helps avoid scaling issues, in which the objective with largest magnitude is favoured by the optimization method, to the detriment of the other. Furthermore, constraints are added to to ensure that the interface stress F_σ and bone remodelling F_r objectives are below prescribed critical values F_r^* and F_σ^*, respectively.

Design space

In order to ensure that the geometric parameter combinations for each element belong to the permitted design space as described in Section 3.2.1, a signed distance field is generated from the binary design space (Fig. 3.9). The distance field, computed via a distance transform, maps the distance from any point $x \in \Omega$ to the boundary of a domain $\Phi \subseteq \Omega$. Points outside of Φ correspond to positive values, and points within Φ are assigned a value of 0. The sum of the distance field is included as a constraint in the optimization routine.

Formally, the element-wise constraint C_i with design element i is

$$C_i = DT_\Phi(a_i, d_i) \tag{3.14}$$

where Φ is a binary representation of the permissible parameter combinations, and $DT_\Phi(a_i, d_i)$ is the distance transform of Φ, evaluated at (a_i, d_i). The sum of the element-wise constraint values for all n elements is then constrained to be less than or equal to zero.

$$\sum_{i=1}^{n} C_i \leq 0 \qquad (3.15)$$
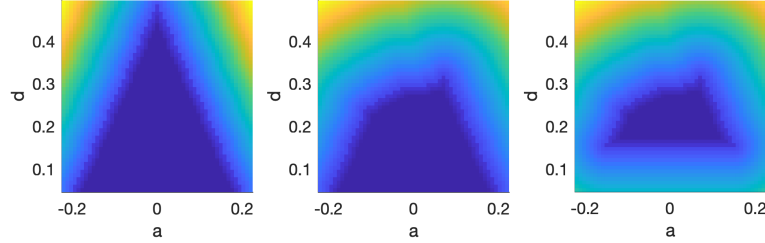
Fig. 3.9.: Distance fields corresponding to the design spaces shown in Fig. 3.4

Optimization formulation

To ensure that the optimized implant is not unduly sensitive to variations in the loading conditions, we consider multiple loading conditions: walking and stair climbing. We formulate our design objective as a min-max problem in which the worst case performance is optimized. Overall, the optimization problem is

$$\begin{aligned}
\min_{\mathbf{a},\mathbf{d}} \quad & \max_{l \in L}(w_\sigma \cdot F_\sigma^l + w_r \cdot F_r^l) \\
\text{subject to} \quad & \mathbf{K}\mathbf{U}_l = \mathbf{F}_l & l = 1, ..., L \\
& F_r^l \leq F_r^{l*} & l = 1, ..., L \\
& F_\sigma^l \leq F_\sigma^{l*} & l = 1, ..., L \\
& \sum_{i=1}^{n} C_i \leq 0
\end{aligned} \qquad (3.16)$$

where F_σ^l and F_r^l are the interface stress and bone remodelling objectives for load case l, and L is the number of the load cases considered. The state equation $\mathbf{K}\mathbf{U}_l = \mathbf{F}_l$ is solved to obtain the unknown displacements $\mathbf{U}_l$ corresponding to load $\mathbf{F}_l$. Additional constraints ensure that the bone remodelling F_r^l and interface stress F_σ^l objectives are below the prescribed critical values F_r^{l*} and F_σ^{l*}, respectively. The stress tensors $\boldsymbol{\sigma}_e$ are computed for each element e as:

$$\boldsymbol{\sigma}_e^l = \mathbf{C}_e \mathbf{B}_e \mathbf{u}_e^l \qquad (3.17)$$

where $\mathbf{C}_e$ is the local isotropic constitutive tensor, with $\nu = 0.3$ and E is defined as a function of the local bone density, according to [9]:

$$E(\rho) = \begin{cases} 1.904\,\rho^{1.64} & 0 < \rho < 0.95 \\ 2.065\,\rho^{3.09} & 0.95 \le \rho \le 1 \end{cases} \tag{3.18}$$

$\mathbf{B}_e$ is the strain-displacement matrix and $\mathbf{u}_e^l$ is the solution corresponding to the degrees of freedom associated with element e.

To obtain the local Hoffman interface failure risk, the stress tensors are aligned to the interface normal direction via the coordinate transformation, i.e.,

$$(\boldsymbol{\sigma}_e^l)_\perp^{full} = Q(\mathbf{n}_e) \cdot (\boldsymbol{\sigma}_e^l)^{full} \cdot Q(\mathbf{n}_e)^T \tag{3.19}$$

Here, $\mathbf{n}_e$ is the interface normal, $Q(\mathbf{n}_e)$ is a coordinate transformation matrix, and $(\boldsymbol{\sigma}_e^l)^{full}$ and $(\boldsymbol{\sigma}_e^l)_\perp^{full}$ are the full rank element stress tensors. The normal σ and shear τ components are obtained from the components of $(\boldsymbol{\sigma}_e^l)_\perp^{full}$.

The normal and shear stress components σ_e and τ_e are obtained from the interface-aligned stress tensor that are computed as $(\boldsymbol{\sigma}_e^l)_\perp^{full}(1,1)$ and $\sqrt{(\boldsymbol{\sigma}_e^l)_\perp^{full}(1,2)^2 + (\boldsymbol{\sigma}_e^l)_\perp^{full}(1,3)^2}$, respectively.

Finally, since we are concerned with elements along the bone-implant interface, we eliminate the distant elements by dividing the element-wise Hoffman function $f(\sigma_e)$ by the distance from the centroid of the element to the implant boundary,

$$\tilde{f}(\sigma_e) = \frac{f(\sigma_e)}{d(x_e)}. \tag{3.20}$$

For elements that intersect with the implant boundary, $d(x_e)$ is the distance from the centroid of the portion of the element which lies within the implant. The global risk function is then given by:

$$F_\sigma = \left(\sum_{e \in n} \tilde{f}(\sigma_e)^p \right)^{\frac{1}{p}} \tag{3.21}$$

Filtering

The proposed optimization strategy is susceptible to mathematical instabilities, introduced by the finite element representation. A common solution is to regularize the

design variables by means of a convolutional operator. Specifically, the convolutional operator calculates a weighted average of the neighbouring values via

$$\tilde{\phi}_e = \frac{\sum_{i \in \mathbb{M}} w_{i,e} \phi_i}{\sum_{i \in \mathbb{M}} w_{i,e}},$$ (3.22)

where ϕ refers to design variables a and d. $\mathbb{M}_e$ is the set of voxels close to voxel e, i.e.,

$$\mathbb{M}_e = \{i | ||x_i - x_e||_2 \leq r_e\}$$ (3.23)

with filter radius r_e. The weighting factor $w_{i,e}$ is inversely related the distance between voxels i and e, i.e.,

$$w_{i,e} = 1 - \frac{||x_i - x_e||_2}{r_e}$$ (3.24)

Sensitivity analysis

The optimization problem is solved using the method of moving asymptotes (MMA) [143], which takes in the sensitivities of the objective and constraints with respect to the design variables. These sensitivities are obtained via adjoint analysis. For details, refer to the Appendix.

3.3 Results & Discussion

In this section, the proposed optimization strategy is applied to the design of a hip stem. The implant is made from titanium ($E = 116GPa, \nu = 0.34$), and its geometry is based on a standard tapered, press-fitted design, described in [43]. The loading conditions are based on the walking and stair climbing profiles described in [62]. The optimized design's performance is compared to those of a fully solid and highly porous ($E = 3.4GPa, \nu = 0.05, \mu = 0.06GPa$) titanium designs. The accuracy of the homogenization-based finite element analysis (FEA) is verified, in 2D, by re-evaluating the bone-implant system in full micro-architectural detail. Finally, we investigate the performance of the algorithm for various implant geometries.

An optimized hip stem is shown in Fig. 3.10, alongside benchmark solid and porous designs. As expected, the solid implant exhibits significant bone remodelling due to the stress shielding, but presents a low risk of interface fracture. On the other hand, the compliant porous design generates considerably lower bone resorption, but induces a high risk of interface fracture in the proximal lateral interface region.

Shape	Microarchitecture	Fig.	FEA	Interface Risk (F_σ)	Bone Remodelling (F_r)	Huiskes Bone Resorption
Type 1 (Single-wedge)	Solid	3.10	3D/AH	5.85×10^0	2.67×10^8	33.5%
	30% density cubic lattice	3.10	3D/AH	5.18×10^2	1.22×10^8	17.8%
	Optimized CAC lattice	3.10	3D/AH	5.08×10^0	9.61×10^7	16.1%
	Optimized CAC lattice under manufacturing constraints	3.15	3D/AH	6.07×10^0	1.11×10^8	17.2%
Type 2 (Double-wedge)	Solid	3.14	3D/AH	3.96×10^0	2.75×10^8	29.9%
	30% density cubic lattice	3.14	3D/AH	2.27×10^3	4.07×10^8	14.3%
	Optimized CAC lattice	3.14	3D/AH	1.34×10^1	1.08×10^8	17.8%
Type 3 (Tapered)	Solid	3.14	3D/AH	7.5×10^0	2.75×10^8	30.1%
	30% density cubic lattice	3.14	3D/AH	3.49×10^3	8.55×10^8	13.6%
	Optimized CAC lattice	3.14	3D/AH	1.91×10^1	1.24×10^8	19.4%
Type 1-Short	Solid	3.14	3D/AH	5.84×10^0	2.08×10^8	17.3%
	30% density cubic lattice	3.14	3D/AH	3.87×10^2	1.01×10^8	8.32%
	Optimized CAC lattice	3.14	3D/AH	4.91×10^0	8.92×10^7	8.97%
Type 1 (Single-wedge)	Optimized CAC lattice	3.13	2D/AH	7.93×10^0	3.36×10^{10}	NA
	Optimized CAC lattice	3.13	2D/Full	8.66×10^0	3.83×10^{10}	NA

Tab. 3.1.: Performance results for all studied implant configurations. Interface risk, bone remodelling, and Huiskes bone resorption function are computed according to Eq. 3.21, Eq. 3.9, and Eq. 3.4, respectively.

By contrast, the optimized design generates 21.2% less bone resorption than the porous implant, and 13.2% less interface stress than the solid implant. Moreover, the predicted bone remodelling associated with the optimized design is 64.0% lower than that of the conventional solid implant. Improved performance in terms of both metrics, compared to the benchmark solid and porous designs, is achieved by setting the objective constraints according to the performance of the benchmarks. If the constraints are respected, this guarantees that the optimized design shall perform at least as well as the benchmark designs, in terms of their respective strengths. Performance in terms of the interface fracture risk and bone remodelling objectives is computed according to Eq. 3.21 and Eq. 3.9, respectively, and presented in Table 5.1. Performance in terms of the bone resorption metric proposed by Huiskes [66] is also included, for comparison.
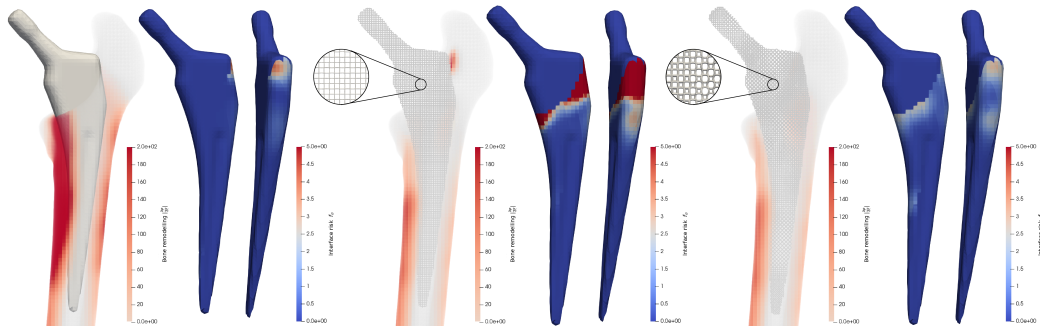
Fig. 3.10.: The design and performance of a) solid, b) uniform lattice, c) optimized heterogeneous lattice titanium implants in terms of local bone remodelling and the Hoffman interface stress risk indices.

The optimization history, shown in Fig. 3.11, highlights the stability of the optimization routine. The initial, uniform lattice (Fig. 3.10-b) converges smoothly to the

final design (Fig. 3.10-c) after 50 iterations. The interface risk and bone remodelling objectives are each normalized with respect to their initial values (iteration 1). In this case, the interface stress risk was constrained to be less than or equal to that of the solid implant design. As a result, the interface stress is prioritized over bone remodelling, if both objectives cannot be improved simultaneously.
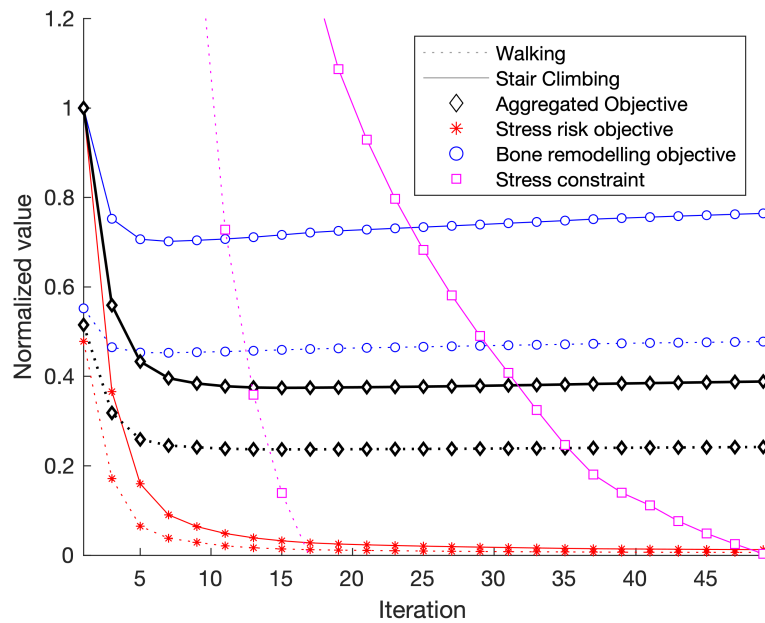
Fig. 3.11.: The optimization history starting from the uniform lattice shown in Fig. 3.10-b and ending in the design shown in Fig. 3.10-c.

The optimized implant possesses a highly non-uniform geometric parameter distribution, spanning nearly the entire range of allowed parameter combinations (Fig. 3.12). This heterogeneity is precisely what enables its improved performance. This was confirmed by running the optimization routine with a reduced design space.

The proposed optimization routine, like other multi-scale finite element-based methods, relies on asymptotic homogenization. This means that the fine scale mechanics are not captured in their true detail. While it has been demonstrated that AH is accurate for semi-periodic structures with large length scale separation [7], we confirm the reliability of our model by comparing the AH-based performance with that of the full-detail structure. Simplification to 2D was necessary to reduce the computational cost of the analysis. Additionally, a relatively coarse ground mesh with elements of the size $2 \times 2\,$mm was used for the AH-based study, such that each unit cell of the micro-architected implant was modelled as 60×60 standard linear quadrilateral finite elements in the detailed study ($\sim$2.7 million $33 \times 33\,\mu$m elements). The results indicate that the homogenization-based model is highly accurate, both in terms of bone remodelling and interface fracture risk, with 8.4% difference in the peak
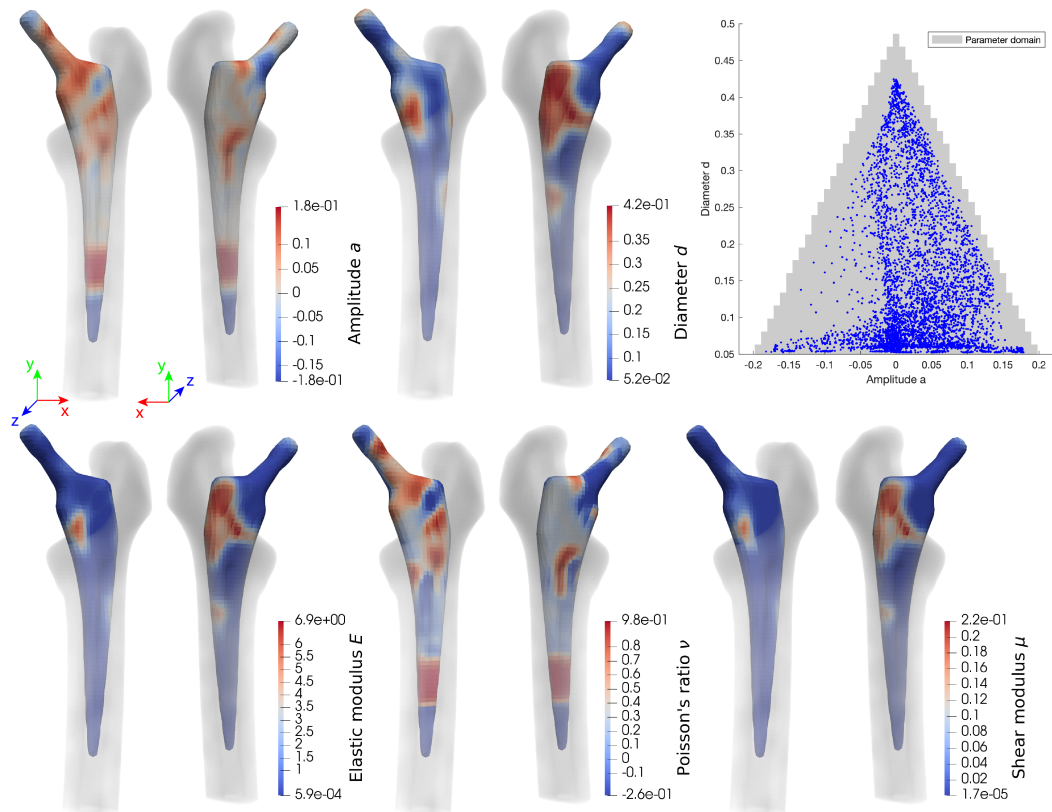
Fig. 3.12.: Geometric parameter (top) and mechanical property (bottom) distribution associated with the implant shown in Fig. 3.10-c.

interface risk predictions and 14.0% difference in total bone remodelling. AH-based and FEA considering the full micro-architectural detail are shown in Fig. 3.13. Note that the FEA study considering full detail uses a 5 times finer mesh in the bone region in order to capture any stress concentrations introduced by the sharp edges of the implant micro-architecture. This explains small discrepancies and the oscillation of the fracture risk along the interface.

3.3.1 Alternative implant shapes

The results presented in this work make use of a common implant geometry. However, many implant designs exist in the industry. In particular, minimally invasive implants with shortened stems have recently been gaining traction [17]. It is therefore relevant to assess the performance of the proposed optimization strategy with various implant geometries. To this end, three alternative implant designs were studied, namely Type 2, Type 3, and Type 1-short stems, according to the Mont group classification system [75].
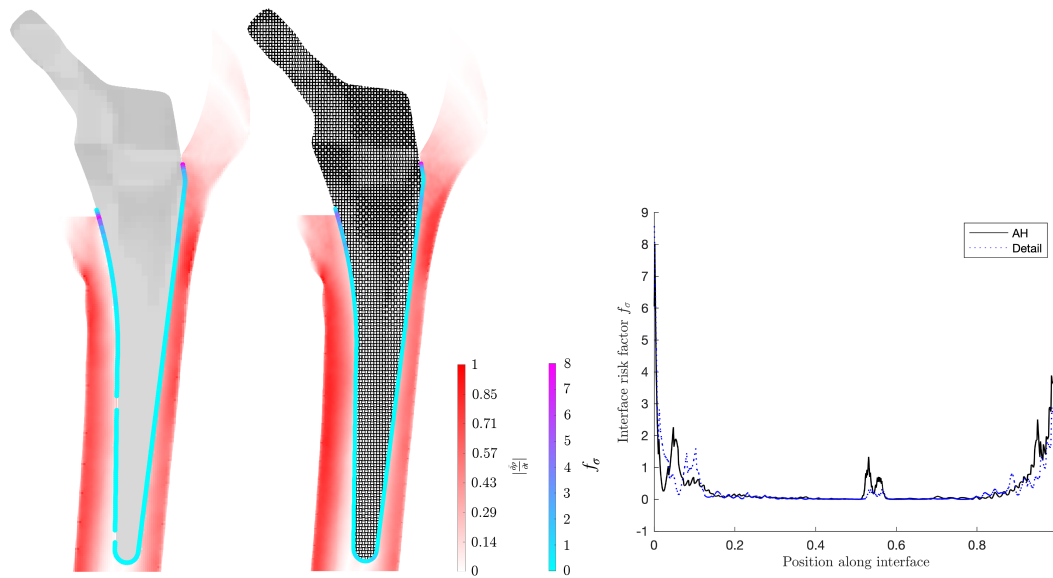
Fig. 3.13.: Performance comparison of asymptotic homogenization-based FEA (left) and FEA considering full micro-architectural detail (right).The homogenization-based implant design is shown here in terms of mean local density.

In Fig. 3.14, three alternative implant geometries are optimized. The results indicate that the optimization routine is able to significantly improve performance, in each case. In all cases, the solid implant (left) triggers high remodelling, particularly along the medial interface. The interface fracture risk is low in each case, with maximal values near the resected surface, especially along the lateral interface. The uniform highly porous lattice (center) triggers less bone remodelling along the bone shaft, but introduces apposition in the greater trochanter, due to the increased stress in this region. This increased stress also introduces a significant risk of interface fracture in this area and in the interface near resected bone surface. The optimized lattice implants (right) induce an intermediate risk of interface fracture, comparable to (Type 1-short) or somewhat greater (Type 2 and Type 3) than their solid implant counterparts. Bone remodelling is of the same order as for the uniform lattice design, with slightly worse performance along the bone shaft and better performance in the greater trochanter. The performances are summarized in Table 5.1. In all studies, the optimization procedure produces a design with considerably less bone remodelling and lower interface risk than the uniform lattice, however, we notice that in some cases (Type 2, Type 3, and Type 1 under manufacturing constraints), the interface risk is somewhat worse than in the solid design. This is likely due to the constraints on the design space that prevent any part of the design from becoming fully solid.
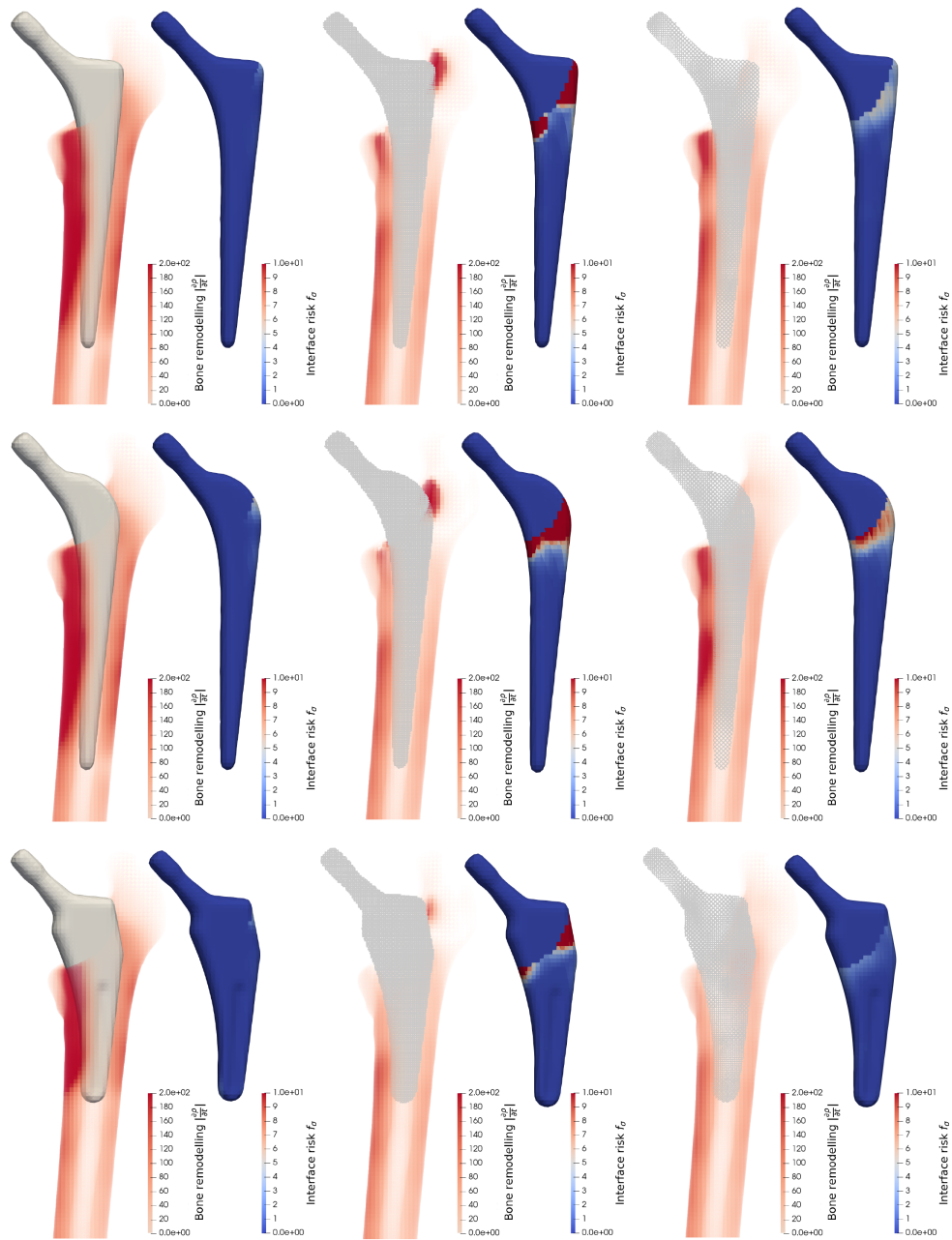
Fig. 3.14.: Performance comparison between solid (left column), uniform lattice (center column), and optimized lattice (right column) for Type 2 (top row), Type 3 (middle row), and Type 1-short (bottom row) implant geometries (Mont classification).

3.3.2 Manufacturing constraints

The results presented thus far are dependent upon manufacturing methods which are not yet reliable and cost-competitive with standard implant designs. In order to ensure the accuracy of the homogenization method employed in this work, 5 micro-architecture unit cells per centimeter were used, together with linear filtering of the design variables according to Eq. 3.22 with $r_e = 3.2$. With a minimum diameter setting of 0.05, the minimum feature size is $100\,\mu\mathrm{m}$, which corresponds to the accuracy limit of the current generation of SLM machines [12]. While SLM technology is still improving, we demonstrate the effectiveness of our method for use with readily available machines by constraining the minimum feature size, for both material and gaps to $200\,\mu\mathrm{m}$. The results presented in Fig. 3.15 and Table 5.1 indicate that, even with a significant reduction to the design space, bone remodelling can be reduced by 58.4% as compared to a solid implant, with a negligible impact on the risk of interface fracture.
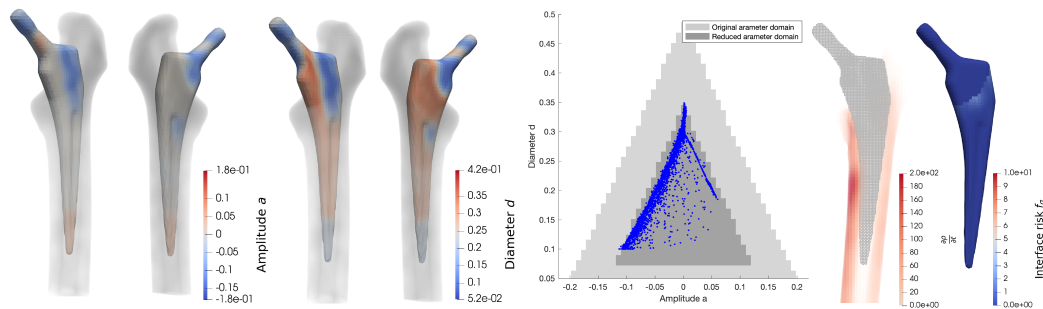
Fig. 3.15.: The design and performance of an optimized implant with a length scale of $200\,\mu\mathrm{m}$. The performance values are included in Table 5.1.

3.4 Conclusion

The optimization strategy presented in this work has proven capable of simultaneously reducing the risk of interface fracture as well as bone remodelling (and resorption), in-silico. The proposed method incorporates an accurate and versatile bone remodelling function and an efficient decoupled multi-scale strategy, capable of accurately capturing interface mechanics at comparatively low computational cost. Additionally, a generalized cubic anti-chiral parametric micro-architecture, highly suited to functionally graded structural design and capable of achieving a wide range of mechanical properties was presented. Alongside this, a new method to incorporate geometric constraints on the parametric design space allows for the

inclusion of any number of micro-level constraints, such as minimum/maximum length scale (feature size), porosity, pore size, etc, at zero extra computational cost.

This work was limited to computer simulation and should be followed up with physical testing, both in vitro and in vivo. Moreover, these results are based on linear finite element analyses, which do not capture micro-scale behaviour and non-linear effects such as buckling. While the incorporation of non-linear analysis in the proposed methodology is computationally infeasible, a non-linear analysis of the final design on a high performance cluster should be performed.

An Insertability Constraint for Shape Optimization

<div align="right">4</div>

Abstract

Patient-specific implants offer a host of benefits over their generic counterparts. Nonetheless, the design and optimization of these components present several technical challenges, among them being the need to ensure their insertability into the host bone tissue. This presents a significant challenge due to the tight-fitting nature of the bone-implant interface.

This chapter presents a novel insertability metric designed to efficiently assess whether a rigid body can be inserted into a tight-fitting cavity, without interference. In contrast to existing solutions, the metric is fully differentiable and can be incorporated as a design constraint into shape optimization routines. By exploiting the tight-fitting condition, the problem of planning an interference-free insertion path is reformulated as the search for a single interference-free movement, starting from the inserted configuration. We prove that if there exists any outward movement for which no interference is indicated, then the body can be fully extracted from or, equivalently, inserted into the cavity. This formulation is extremely efficient and highly robust with respect to the complexity of the geometry.

We demonstrate the effectiveness and efficiency of our method by applying it to the optimization of two-dimensional (2D) and three-dimensional (3D) designs for insertability, subject to various design requirements. We then incorporate the proposed metric into the optimization of an acetabular cup used in total hip replacement (THR) surgery where geometric and structural requirements are considered.

4.1 Introduction

Insertability analysis, which is the problem of assessing whether a rigid body can be inserted into a tight-fitting cavity, is ubiquitous in a wide range of engineering applications. In automated tooling, for example, it is used to plan an interference-free path for inserting robotically-guided parts into mating fixtures [24, 104]. In molding, it is used to ensure that the part can be extracted from the core and cavity without excessive force [25]. And in machine design, it is used for assembly and tolerance analysis [128]. In particular, with respect to the design of orthopaedic implants, where a tight fit with the host bone is usually required, insertability analysis plays a key role in avoiding obstructing geometry and stuck configurations.

With advances in medical imaging and computational analysis, virtual models of a patient's specific anatomy can be synthesized and used to develop custom orthopedic implants, designed to best fit the patient's unique anatomy. These implants may also be optimized for maximum long-term performance by simulating their effect on the host bony tissue. Nonetheless, the design of patient-specific implants is fraught with new technical challenges, not least of which is the requirement that the implant be insertable into the host bone tissue, without interference. The insertability requirement is particularly difficult to incorporate into a design optimization framework because of (1) the tight-fitting nature of the bone-implant system, and (2) the need for a differentiable insertability metric.

The problem of assessing the insertability of tight-fitting components has been extensively studied in the field of robotics, where it is known as the peg-in-hole problem [123]. It is typically treated as a special instance of the general path planning problem, wherein the goal is to determine how to insert a movable body (the peg) into a stationary cavity (the hole) without interference [83]. What makes the peg-in-hole problem challenging is that the body and cavity share nearly complementary geometry in the inserted configuration, resulting in highly constrained movement. This feature significantly decreases the efficiency and efficacy of traditional path-planning strategies, especially when considering 3D motion and complex geometry. Traditionally, solving the peg-in-hole problem involves searching the space of all possible physical configurations (configuration space) for a continuous non-overlapping set of interference-free configurations leading from an initial uninserted configuration to a final inserted configuration [69]. The search for an insertion path involves two tasks: (1) determining if a particular configuration is interference-free, and (2) planning a path between interference-free configurations. How and when these tasks are performed is determined by the particular path-planning strategy

employed. These strategies can be categorized as either global or local, based on how they explore the configuration space.

Global path planning strategies first divide the entire configuration space into discrete cells, individually assessing each one for interference. Path planning is performed only once the configuration space has been fully mapped out. These strategies are effective when the topography of the configuration space can be captured with a reasonably coarse sampling. However, for tight-fitting insertion problems, with complex geometry and small clearance, a prohibitively fine sampling may be required in the vicinity of the inserted configuration. This is exacerbated by the high computational cost of the methods used to assess interference, which typically involve dividing the geometry into fine polyhedra and repeatedly testing for overlap between the polyhedra of different bodies. Moreover, for tight-fitting bodies, where small incremental movements are required for insertion, simplification of the geometry or reduction of the configuration space is not possible. Therefore, techniques such as hierarchical decomposition [45, 171], geometry simplification [67], or selective exploration of configuration space [72, 70] are not applicable, meaning that complete mapping of the configuration space remains infeasible.

Local path planning strategies reduce the number of interference assessments by starting from an initial configuration and using local information to move towards the intended final configuration, mapping out the configuration space only as needed. Conventional local path-planning algorithms, such as artificial potential fields, Dijkstra, A*, D*, and rapidly exploring random trees [130], are often able to plan and adapt a path based on new environmental information but tend to be computationally expensive or become unstable in tight-fitting environments [10]. Intelligent reactive approaches search the configuration space more efficiently by leveraging nature-inspired principles [92]. Among these, genetic algorithms, artificial neural networks, and fuzzy logic have proven effective in navigating some specific types of environments [131].

Despite these advances, few path-planning strategies are efficient in navigating tight-fitting environments with complex geometry. One exception is a method proposed by [69], which specifically targets the peg-in-hole problem by leveraging the tight fit and known insertion direction. It works by partitioning the cavity into neighborhoods. These neighborhoods, defined by convex polyhedra, are then used to generate a set of linear constraints that ensure non-interference, thereby eliminating the need for overlap tests. The algorithm seeks out a sequence of small movements by formulating, for each successive movement, a linear optimization problem in which a move-related task function is minimized while subject to a set

of neighbourhood constraints. This method significantly reduces the cost of each movement. Yet, like other path-planning approaches, it involves searching for a complete path, which may be made up of many individual configurations, each adding to the computational cost of the insertability assessment.

Related to insertability is the problem of ensuring accessibility for machining. [82] suggested a constraint developed for multi-axis machining. This method assesses whether a particular design can be machined from a block of material by effectively making sure that any material to be removed is accessible from one of several prescribed insertion directions. If a single insertion direction is considered, any cavity which can be created by the tool can be interpreted as a hole for which there exists a complementary peg. This method is highly efficient since the insertion path is known. Moreover, it provides gradient information that can be used in design optimization. Nonetheless, it is effective only when an exact rectilinear insertion direction is provided and rotation along the insertion path can be omitted.

In this chapter, we present a novel approach that exploits the tight-fitting condition to assess insertability without computing the entire insertion path. We represent insertability as a continuously differentiable function that can be incorporated into gradient-based optimization to ensure that, to the extent that is possible, the optimized design satisfies the insertability requirement, together with the other design specifications. The insertability analysis can, then, be performed throughout the design process, rather than only as a validation tool.

The insertability problem is reformulated as an extraction problem, in which the object is initially in its inserted configuration. The objective is to determine if there exists a path from this *inserted* configuration to some *uninserted* configuration. We eliminate the need to construct the full path by exploiting the fact that the body and cavity shapes are nearly complementary, which is typically the case in the design and optimization of implants. We prove that if there exists any infinitesimal interference-free movement which moves the body slightly out of the cavity, then the object can be fully extracted, without interference. We demonstrate how our formulation can be employed as a design tool for both generic shape optimization and for advanced structural optimization.

The remainder of this chapter is organized as follows. Section 2 describes the novel insertability metric and the related interference-free criterion. Section 3 presents a shape optimization strategy that incorporates the insertability metric as a design constraint. Section 4 explores an application of the insertability constraint to the optimization of a patient-specific acetabular cup for use in hip replacement surgery.

Interference

Clearance

Initial configuration   New configuration
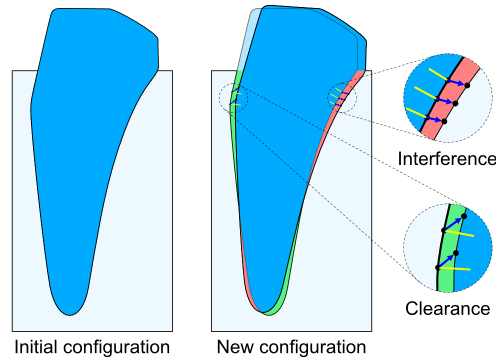
Fig. 4.1.: A body-cavity system shown before and after a small body movement. Clearance and interference are shown in green and red, respectively. Local cavity surface normals are shown in yellow. Sample body surface vertices in areas with interference are displaced in the negative normal direction, while body surface vertices in areas with clearance are displaced in the positive normal direction.

Finally, sections 5 and 6 conclude with a discussion and summary of the numerical results.

4.2 Insertability

Consider the perfectly complementary body-cavity system shown in Fig. 4.1. If the body is slightly rotated, as shown, clearance will be created in some areas (green) and interference will be introduced in others (red). In areas with clearance, points along the body surface are displaced in the direction of the local cavity surface normal, while in areas with interference, they are displaced in the negative normal direction. If all points along the body surface move in the direction of the local cavity wall normal, the configuration is interference-free. The question thus becomes whether there exists such a rigid body motion. This observation eliminates the need for the computationally expensive geometry subdivision and overlap testing commonly used to assess interference. The following describes how interference is assessed mathematically.

We define the movable object B as a rigid 3D body with 6 degrees of freedom (DOF), and the open cavity C as a fixed rigid 3D obstacle, as illustrated in Fig. 4.2. We further define the cavity interior I as the empty space within C, and the cavity exterior E as $\mathbb{R}\backslash I$. Finally, the body-cavity interface Γ includes the complementary surfaces of B and C, which are assumed perfectly coincident. We define a fixed global coordinate system and a movable frame associated with B.
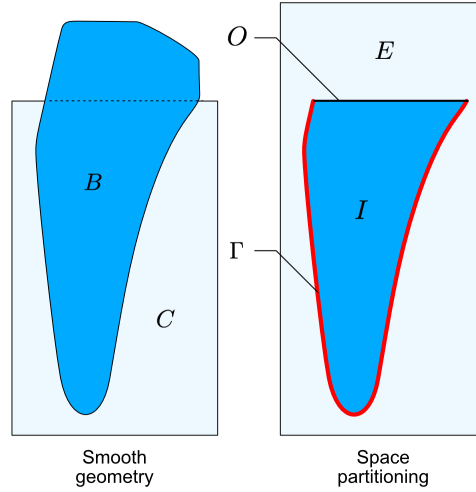
Fig. 4.2.: Illustration of an original (left) and partitioned (right) body-cavity system.

We describe a configuration as the set $(\mathbf{p}, \boldsymbol{\theta})$, made up of three displacements, $\mathbf{p}$, and three rotations, $\boldsymbol{\theta}$, with respect to the fixed coordinate frame.

In a configuration $(\mathbf{p}, \boldsymbol{\theta})$, the position, $\mathbf{v}$, of a body point, $\mathbf{b}$ is expressed as

$$\mathbf{v} = \mathrm{F}(\mathbf{p}, \boldsymbol{\theta}) \cdot \mathbf{b} = \mathrm{Rot}(\boldsymbol{\theta}) \cdot \mathbf{b} + \mathbf{p} \tag{4.1}$$

where $\mathrm{Rot}(\boldsymbol{\theta})$ is the rotation matrix specifying the orientation of the body.

Consider now the rigid body motion $\mathrm{T} : (\mathbf{p}^0, \boldsymbol{\theta}^0) \to (\mathbf{p}^*, \boldsymbol{\theta}^*)$, which maps from an initial configuration $(\mathbf{p}^0, \boldsymbol{\theta}^0)$ to a new configuration $(\mathbf{p}^*, \boldsymbol{\theta}^*)$. The resulting displacement for a point $\mathbf{b}$ is:

$$\mathbf{r}_b = \mathrm{F}(\mathbf{p}^*, \boldsymbol{\theta}^*) \cdot \mathbf{b} - \mathrm{F}(\mathbf{p}^0, \boldsymbol{\theta}^0) \cdot \mathbf{b} \tag{4.2}$$

If point $\mathbf{b}$ is on the body-cavity interface, Γ, in $(\mathbf{p}^0, \boldsymbol{\theta}^0)$, $\mathbf{r}_b$ may be expressed in terms of local interface normal and interface tangent components, $\hat{\mathbf{n}}_b$ and $\hat{\mathbf{t}}_b$, as illustrated in Fig. 4.3:

$$\mathbf{r}_b = r_b^n \hat{\mathbf{n}}_b + r_b^t \hat{\mathbf{t}}_b \tag{4.3}$$

where $\hat{\mathbf{n}}_b$ is defined as pointing towards the cavity interior.
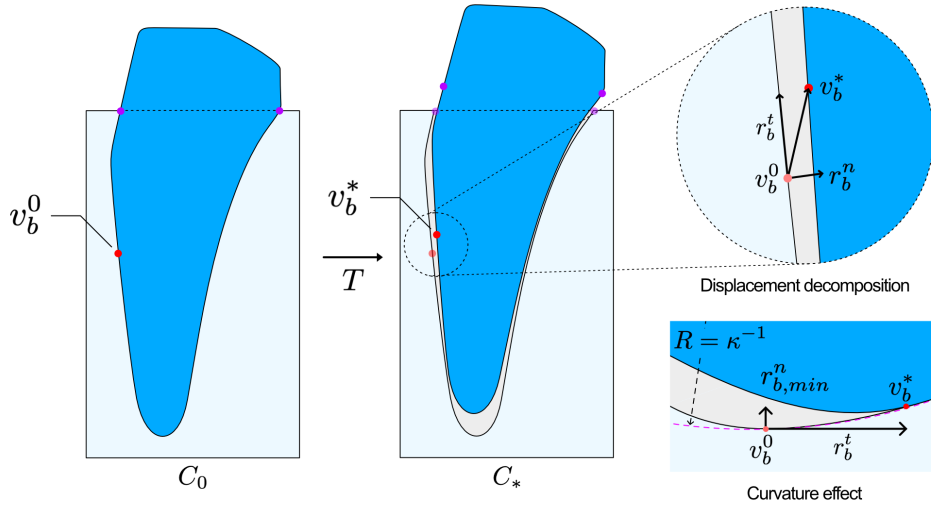
Fig. 4.3.: A body-cavity system in its inserted configuration, C^0, (left) and a perturbed configuration, C^* (center). The net displacement of a point **b** from v_0 to v_* of an arbitrary interface point (red) is decomposed into interface normal and tangent components, with respect to the interface in configuration C^0. The minimum normal displacement, as defined in Eq. 5.2, is shown for a case in which $r^n = r^n_{min}$.

4.2.1 Interference-free criterion

Interference is defined as the condition in which two bodies overlap at some point in space. For a continuous motion, starting from a tight-fitting configuration, interference can only initiate where both bodies were previously coincident. Therefore, analysis of the instantaneous velocities of the bodies along their interface can predict subsequent interference.

Let us now consider a motion $T : (\mathbf{p}^0, \boldsymbol{\theta}^0) \to (\mathbf{p}^*, \boldsymbol{\theta}^*)$ which results in an infinitesimally small movement of the body. If the resulting displacement $\mathbf{r}_b$ of a point **b** on the interface Γ is positive with respect to the local normal, *i.e.*,

$$\mathbf{r}_b = r^n_b \hat{\mathbf{n}}_b, \ r^n_b \geq 0 \tag{4.4}$$

then it can be said that T is collision-free with respect to **b**.

For the general case in which the tangential displacement is non-zero, the displacements should be limited based on the shared local interface curvature, κ_b. If the local curvature is less than or equal to 0, the minimum normal displacement is unrelated to the tangential displacement. However, when the local curvature is positive, a purely tangential displacement causes interference. In this case, a minimum normal displacement r^n_{min} is defined based on the local interface curvature, κ, and the

tangential displacement r_b^t, as shown on the bottom right of Fig. 4.3. Graphically, r_{min}^n is the distance in the normal direction $\hat{n}_b$ from v_b^0 to the intersection of the local curvature circle and a line parallel to r_b^n through the point $v_b^0 + r_b^t \hat{t}_b$. Mathematically, r_{min}^n is given by:

$$r_{min}^n = \begin{cases} \kappa^{-1} - \sqrt{\dfrac{\kappa^{-2}(r_b^t)^2}{\kappa^{-2}-(r_b^t)^2}} & \text{if } \kappa_b > 0 \\ 0 & \text{otherwise} \end{cases} \tag{4.5}$$

and Eq. 4.4 is replaced by the general local Interference-free criterion

$$r_b^n \geq r_{min}^n \tag{4.6}$$

Since we are concerned with infinitesimal displacements, the local curvature is not expected to change significantly from v^0 to v^*. The constraint is, therefore, sufficient to prevent interference.

If Eq. 4.6 is respected for all points along Γ, then T is interference-free. This can be expressed as:

$$\mathcal{I} = \max_{b \in \Gamma} \left(r_{min}^n - r_b^n \right) \leq 0 \tag{4.7}$$

To facilitate differentiability, the Kreisselmeier-Steinhauser (KS) function commonly employed in numerical optimization [78, 1, 112] is used to approximate the maximum function. The final Interference-free criterion is then expressed as:

$$\mathcal{I} \approx \mathop{\mathrm{KS}}_{b \in \Gamma}\left(r_{min}^n - r_b^n \right) = \frac{1}{\rho}\ln \sum_{b \in \Gamma} e^{\rho\left(r_{min}^n - r_b^n \right)} \leq 0 \tag{4.8}$$

where ρ is a tuning parameter, typically in the range $100 \sim 1000$.

4.2.2 Path planning

Traditionally, insertability analysis requires the iterative computation of a complete path between the inserted and extracted configurations. The high computational cost associated with this process is exacerbated when full 6 DOF motion and complex geometry are considered. Here, we exploit the tight-fitting condition to circumvent the process entirely.

Consider the perfectly complementary body-cavity system shown in Fig. 4.4 and an interference-free transformation $\mathrm{T} : (\mathbf{p}^0, \boldsymbol{\theta}^0) \to (\mathbf{p}^*, \boldsymbol{\theta}^*)$. T is defined as non-reentrant if it results in an exclusively outward movement of the body with respect to the cavity. In other words, any point b on the cavity opening O in the initial configuration must either remain on O or move to the cavity exterior E, as a result of the movement T, *i.e.,*

$$\mathbf{v}_b^* \in (O \cup E), \; \forall \; \mathbf{v}_b^0 \in O \tag{4.9}$$

If there exists a non-zero T which simultaneously satisfies the non-reentrance and the interference-free criteria, it can be proven that successive application of the same transformation T on B will always be interference-free and will eventually lead to full extraction from the cavity. In other words, T describes a full interference-free extraction/insertion path.

Property 1: Successive application of T on B is always interference-free
Proof: Consider a body point $\mathbf{b}_j$ which initially lies inside the cavity interior I. The transformation $\mathrm{T}\big((\mathbf{p}^0, \boldsymbol{\theta}^0) \to (\mathbf{p}^*, \boldsymbol{\theta}^*), \mathbf{b}_j\big)$ moves $\mathbf{b}_j$ from $\mathbf{v}_j^0 \in I$ to $\mathbf{v}_j^* \in (I \cup E)$. If $\mathbf{v}_j^* \in E$, then $\mathrm{T}\big((\mathbf{p}^*, \boldsymbol{\theta}^*) \to (\mathbf{p}^{**}, \boldsymbol{\theta}^{**}), \mathbf{b}_j\big)$ moves $\mathbf{b}_j$ from $\mathbf{v}_j^*$ to $\mathbf{v}_j^{**} \notin I$ (case 1), since T satisfies the non-reentrance criterion. Otherwise, if $\mathbf{v}_j^* \in I$ (case 2), then $\mathbf{v}_j^*$ is coincident with some position $\mathbf{v}_k$ corresponding to a body point $\mathbf{b}_k$ in the initial configuration $(\mathbf{p}^0, \boldsymbol{\theta}^0)$. Since $\mathrm{T}\big((\mathbf{p}^0, \boldsymbol{\theta}^0) \to (\mathbf{p}^*, \boldsymbol{\theta}^*), \mathbf{b}_k\big)$ was interference-free, $\mathrm{T}\big((\mathbf{p}^*, \boldsymbol{\theta}^*) \to (\mathbf{p}^{**}, \boldsymbol{\theta}^{**}), \mathbf{b}_j\big)$ is guaranteed to be interference-free. Thus, repeated application of T on B will always be interference-free.

Property 2: Successive application of T on B eventually leads to complete extraction
Proof: Excluding the trivial zero-displacement solution, any transformation T which satisfies the non-reentrance constraint results in a portion of the body exiting the cavity. Suppose T moves $\mathbf{b}_j$ from $\mathbf{v}_j^0 \in O$ to $\mathbf{v}_j^* \in E$. Given that B is a single continuous entity, T moves some $\mathbf{b}_k$ from $\mathbf{v}_k^0 \in I$ to $\mathbf{v}_j^0 \in O$. This means that each application of T on B causes some portion of B to exit the cavity. Since B is always purely exiting, repeated application of T will eventually lead to the full extraction of B.

The process of assessing whether a body-cavity system is insertable along a path described by the movement T is described in Algo. 1. The algorithm reports the degree of insertability, measured by the amount of interference (Eq.4.8. This scalar-valued metric allows an optimization routine to find the motion which minimizes interference.
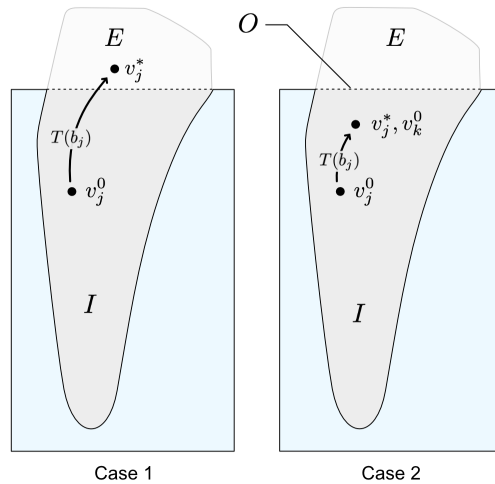
Fig. 4.4.: An illustration of both possible scenarios resulting from the application of transformation T to a body point b_j. In case 1, b_j moves from v_j^0 to v_j^*, which lies outside of the cavity interior. In case 2, b_j moves from v_j^0 to v_j^*, which overlaps with the position v_k^0 of some point b_k in the initial configuration C_0.

4.3 Design optimization

The proposed insertability metric, defined as the scalar output of Eq. 4.8, can be used as an efficient design validation tool. However, it is most effectively used as a constraint in structural optimization. To demonstrate this, we formulate a shape/topology optimization problem, following a common level set approach [5]. This formulation is ideally suited to the interference constraint since it provides a crisp interface and allows for an efficient representation of arbitrarily complex topology [146].

The following sections describe the level set method and provide detail on how the insertability constraint is implemented.

4.3.1 Design parametrization

The continuous body-cavity system is represented as a discrete nodal level set field on a regular grid, as shown in Fig. 4.5. The surface geometry is defined as the zero contour of the level set Γ, with $\phi_i > 0$ designating the interior of the body, and $\phi_i < 0$ designating the exterior. The positions of the zero contour vertices Γ_x are linearly interpolated from the nodal level set values according to:

Algorithm 1: INSERTABILITY

Input: A set of n interface vertex coordinates $\mathbf{\Gamma}_x$, unit normals $\mathbf{\Gamma}_{\hat{n}}$, and
      curvature values $\mathbf{\Gamma}_{\kappa}$, an immersed condition function, ψ, and a
      transformation T

Output: A scalar value $\mathcal{I}$ representing the degree of insertability of design $\mathbf{x}$
       with respect to the transformation T
---
1 **for** $i \leftarrow 1$ **to** n **do**
2      $\mathbf{x}_i \leftarrow \mathbf{\Gamma}_x[i]$
3      $\hat{\mathbf{n}}_i \leftarrow \mathbf{\Gamma}_{\hat{\mathbf{n}}}[i]$
4      $\kappa_i \leftarrow \mathbf{\Gamma}_{\kappa}[i]$
5      $\psi_i \leftarrow LERP(\boldsymbol{\psi}, \mathbf{x}_i)$
6   **if** $\psi_i > 0$ **then**
7          $\mathbf{v}_0 \leftarrow \mathbf{x}_i$
8          $\mathbf{v} \leftarrow T(\mathbf{x}_i)$
9          $\mathbf{r} \leftarrow \mathbf{v} - \mathbf{v}_0$
10         $r_n \leftarrow \mathbf{r} \cdot \hat{\mathbf{n}}$
11         $r_t \leftarrow ||\mathbf{r}|| - r_n \cdot \mathbf{r}$
12         $r_n^{min} \leftarrow$ Eq.5.2(κ_i, r_t)
13         $I[i] \leftarrow r_n^{min} - r_n$

14 $\mathcal{I} = KS(I)$
15 **return** $\mathcal{I}$

$$\mathbf{\Gamma}_{\mathbf{x}_i} = \frac{|\phi_i^{p1}|\mathbf{x}_i^{p2} + |\phi_i^{p2}|\mathbf{x}_i^{p1}}{|\phi_i^{p1}| + |\phi_i^{p2}|} \tag{4.10}$$

where $\mathbf{x}_i^{p1}$ and $\mathbf{x}_i^{p2}$ represents the field values of the parent nodes, associated with ϕ_i^{p1} and ϕ_i^{p2}, respectively.

This representation provides a crisp interface and automatically generates a set of sample interface points for assessing insertability, along with their respective surface normals and curvature.

Interface properties

The zero contour $\mathbf{\Gamma}$ provides a polygonal representation of the smooth geometry. In spite of this, the local normal and curvature information at the vertices can be readily obtained from the gradient of the level set field:
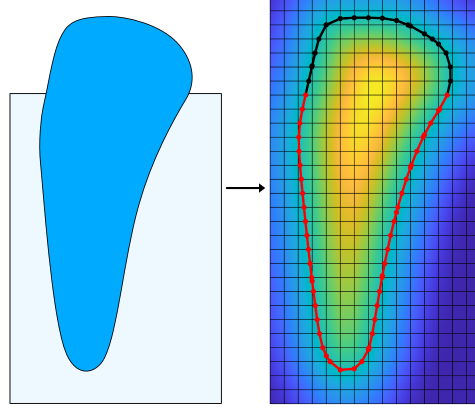
Fig. 4.5.: An illustration of a continuous body-cavity system (left), approximated as a discrete level set ϕ (right). The level set zero contour Γ is partitioned into interface vertices (red) and external vertices (black). By convention, $\phi > 0$ on the interior and $\phi < 0$ on the exterior.

$$\nabla \phi_{l,m,n} = \left[\frac{\partial \phi_{l,m,n}}{\partial x}, \frac{\partial \phi_{l,m,n}}{\partial y}, \frac{\partial \phi_{l,m,n}}{\partial z} \right]^T \tag{4.11}$$

$$\frac{\partial \phi_{l,m,n}}{\partial x} = \frac{\phi_{l+1,m,n} - \phi_{l-1,m,n}}{2\Delta x} \tag{4.12}$$

$$\tag{4.13}$$

where $\phi_{l-1,m,n}$ and $\phi_{l+1,m,n}$ are the neighboring level set values in the *x*-direction. The other terms are calculated accordingly for each physical dimension.

The nodal unit normal vectors are obtained by normalizing the local gradient, *i.e.*,

$$\hat{\mathbf{n}} = \frac{\nabla \phi}{||\nabla \phi||} \tag{4.14}$$

and the curvature is obtained as the divergence of the normalized gradient field:

$$\kappa = \nabla \cdot \frac{\nabla \phi}{||\nabla \phi||} \tag{4.15}$$

The zero contour unit normals $\mathbf{\Gamma_{\hat{n}}}$ and curvature $\mathbf{\Gamma_{\kappa}}$ are interpolated from $\hat{\mathbf{n}}$ and κ via Eq. 4.10.

Partitioning

Finally, the body level set zero contour vertices are partitioned into a set of body-cavity interface vertices and a set of external vertices. This is achieved by converting the immersed region (cavity body and interior) into a level set $\psi(\mathbf{x})$, and interpolating its value at each body contour vertex. Positive values correspond to interface vertices and negative values correspond to external vertices.

The discrete field of design variables is not used directly as a level set. Instead, we follow the filter-projection-scaling method presented in [5] to ensure stability and mesh independency. The three stages are described briefly here, for completeness.

Filtering

Firstly, the raw field of design variables, $\mathbf{s}$, is filtered to $\tilde{\mathbf{s}}$. The standard Helmholtz filter, introduced by [84], produces a smoothed field $\tilde{\mathbf{s}}$ as the solution of the equation

$$-r^2\nabla^2\tilde{\mathbf{s}} + \tilde{\mathbf{s}} = \mathbf{s} \tag{4.16}$$

with homogeneous Neumann boundary condition $\frac{\partial \tilde{s}}{\partial \mathbf{n}} = 0$ imposed on the boundary of the design domain. The radius parameter r defines the smoothing strength.

Projection

The projection stage applies the smoothed Heaviside function frequently used in robust topology optimization [148], to sharpen the filtered design. This stage helps stabilize the optimization procedure and can be used to generate additional eroded and dilated variants, in the case of robust optimization.

$$\hat{\mathbf{s}} = \frac{\tanh(\beta\eta) + \tanh(\beta(\tilde{\mathbf{s}} - \eta))}{\tanh(\beta\eta) + \tanh(\beta(1 - \eta))} \tag{4.17}$$

where η is a threshold parameter, and β controls the steepness of the projection. Throughout this work, $\eta = 0.5$ and $\beta = 12$.

Scaling

The final scaling step ensures that $\phi \in [\phi_{min}; \phi_{max}]$, through linear rescaling, *i.e.,*

$$\phi = \phi_{min} + (\phi_{max} - \phi_{min})\hat{s} \tag{4.18}$$

The interval is chosen as $\phi \in [-h/2; h/2]$, where h is the side length of a grid element, following [127] and [5].

4.3.2 Shape modification for insertability

As a first example, we consider a number of 2D and 3D body-cavity systems and use the proposed insertability metric to assess whether they are insertable and, if not, determine how they can be modified to ensure insertability. To that end, we formulate an optimization problem wherein the objective is to minimize a cost function, defined as total shape change (Eq. 4.19, and the insertability requirement (Eq. 4.8) is included as a constraint. This formulation ensures that the design will be rendered insertable while changing the shape as little as possible. The optimization routine then aims to simultaneously find the optimal shape, together with the optimal insertion motion, as defined by $\mathbf{s}$ and T.

The shape match function is defined as:

$$F_S = \frac{1}{n}\sum_{i=1}^{n}|\mathrm{d}(\mathbf{b}_i, S_0)| \tag{4.19}$$

where $\mathrm{d}(\mathbf{b}_i, S_0)$ is the closest distance from a point b_i on the evolving body surface to a point cloud describing the original geometry S_0, which can be interpolated from a pre-computed signed distance field. The resulting constrained optimization problem is solved by mathematical programming using the method of moving asymptotes (MMA) [144]. The procedure for optimizing a design for insertability is shown in Algo. 2. It is also necessary to exclude the trivial solution with transformation T resulting in a trivial zero displacement, as it does not guarantee insertability. This is achieved by imposing a constraint on the minimum net displacement of the body subject to T.

Four uninsertable designs are shown in the top row of Fig. 4.6. The corresponding optimized designs are shown in the bottom row. In each case, the extraction direction is shown by an arrow, and the areas which locally violate the insertability constraint are highlighted in red. Once the iterative optimization procedure has converged, the

---

Algorithm 2: MAKE INSERTABLE

Input: A discrete design field $\mathbf{s}_0$, an immersed condition function ψ

Output: A modified design field $\mathbf{s}$

---

1   $\mathbf{s} \leftarrow \mathbf{s}_0$

2   $T \leftarrow \mathbf{0}$

3   $i \leftarrow 0$

4   **do**

5      $i \leftarrow i + 1$

6      $(\mathbf{s}, T)_{prev} \leftarrow (\mathbf{s}, T)$

7      $\phi \leftarrow \mathcal{S}(\mathcal{P}(\mathcal{F}(\mathbf{s})))$

8      $\mathbf{\Gamma}_x \leftarrow \{(x, y, z) \mid \phi(x, y, z = 0)\}$

9      $\mathbf{\Gamma}_{\hat{n}} \leftarrow \{\frac{\nabla \phi}{\|\nabla \phi\|}(x, y, z) \mid \phi(x, y, z = 0)\}$

10     $\mathbf{\Gamma}_\kappa \leftarrow \{\nabla \cdot \frac{\nabla \phi}{\|\nabla \phi\|}(x, y, z) \mid \phi(x, y, z = 0)\}$

11   **if** $i = 1$ **then** $\mathbf{\Gamma}_x^0 \leftarrow \mathbf{\Gamma}_x$

12     $c_i \leftarrow INSERTABILITY(\mathbf{\Gamma}_x, \mathbf{\Gamma}_{\hat{n}}, \mathbf{\Gamma}_\kappa, \psi, T)$

13     $c_d \leftarrow -DISPLACEMENT(\mathbf{\Gamma}_x, T)$

14     $o_s \leftarrow SHAPECHANGE(\mathbf{\Gamma}_x, \mathbf{\Gamma}_x^0)$

15     $(\mathbf{s}, T) \leftarrow MMA(\min_{(\mathbf{s}, T)}(o_s), \; s.t.\{c_i, c_d\} \leq 0)$

16     $\delta \leftarrow |(\mathbf{s}, T) - (\mathbf{s}, T)_{prev}|$

17   **while** $c_i > 0 \mid c_d > 0 \mid \delta > \delta_{min}$

18   **return** $\mathbf{s}$

---

shape has been modified to eliminate all local interference. Magenta lines highlight the local shape change from the original design.

In the first case, the initial design is axisymmetric and the interference is localized around the undercuts, as shown. The modified design eliminates the undercuts to produce a straight shaft. In the second case, double-curvature is present, resulting in three regions with local interference. The algorithm simultaneously eliminates the double-curvature and modifies the extraction direction to eliminate the interference. The third case is similar to the first and is included to show that the algorithm can handle complex topology such as internal cavities. In this instance, a flooding algorithm [61] is used to distinguish the internal and external contours. Finally, case four highlights the algorithm's ability to handle large rotations. In this instance, the contour is modified to smooth out the protrusion, while largely maintaining its curvature.

Fig. 4.6.: Various 2D body-cavity systems modified for insertability using Eq. 4.19 as the design objective. The original designs (top row) fail to meet the local interference-free criterion at the highlighted points (red). The modified designs (bottom row) are presented along with the local shape change from the original design, shown as magenta vectors. The crosshatching designates the cavity wall. All designs use 2×10^4 node level set meshes with a filter radius of $r = 6$.

Space-filling

Another noteworthy feature of these results is that the algorithm tends to move interface inwards in some areas and outwards in others. In cases where both the body and cavity can be modified, this is adequate. However, in many cases, the cavity geometry is prescribed, and the objective may be to design a body that maximally fills the cavity. In this case, the space-filling version of the shape match function may be used:

$$F_{S^*} = \frac{1}{n} \sum_{i=1}^{n} \begin{cases} \alpha |\mathrm{d}(\mathbf{b}_i, S)| & \text{if } \mathrm{d}(\mathbf{b}_i, S) < 0 \\ \beta |\mathrm{d}(\mathbf{b}_i, S)| & \text{if } \mathrm{d}(\mathbf{b}_i, S) \geq 0 \end{cases} \qquad (4.20)$$

where α and β are tuning parameters, with $\alpha >> \beta$. This ensures that outwards changes are more expensive than inward changes. The same original designs presented in Fig. 4.6 are modified using the shape-filling objective. Results are shown in the top row of Fig. 4.7. In each case, the cavity is unchanged and the design is reduced in order to comply with the insertability constraint.
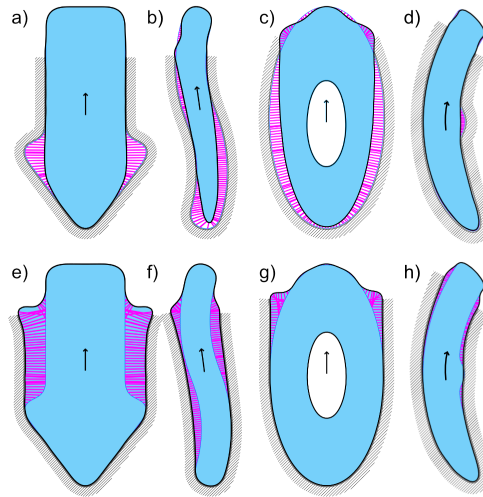
Fig. 4.7.: Results obtained by applying the space-filling (top row) and space-making (bottom row) objectives to the original designs from Fig. 4.6.

Space-making

We also consider a scenario in which only the cavity can be modified, or in which the body must at least occupy the same space as the original. The direction-distinguishing version of the shape-matching function Eq. 4.20 can be used with $\alpha << \beta$. Results obtained using this space-making version are presented in the bottom row of Fig. 4.7. Here, the results refer to the scenario where both body and cavity can be modified. In the case where only the cavity can be modified, the modified interface would be as shown, but the body would remain unchanged.

3D design

The same method is equally applicable to the modification of 3D designs. Various 3D original and modified designs are presented in Fig. 4.8. In 3D, more complex movements are possible. For example, the third example involves a corkscrew motion about the vertical axis. The algorithm successfully identifies the appropriate transformation vector automatically. As for the 2D case, the space-filling and space-making versions may be used instead of the original shape-matching function. Space-making and space-filling results are presented in the lower half of Fig. 4.8. Numerical results for all studies are included in Table 4.1.
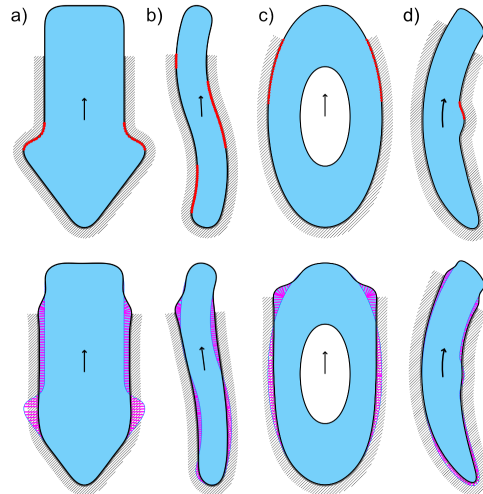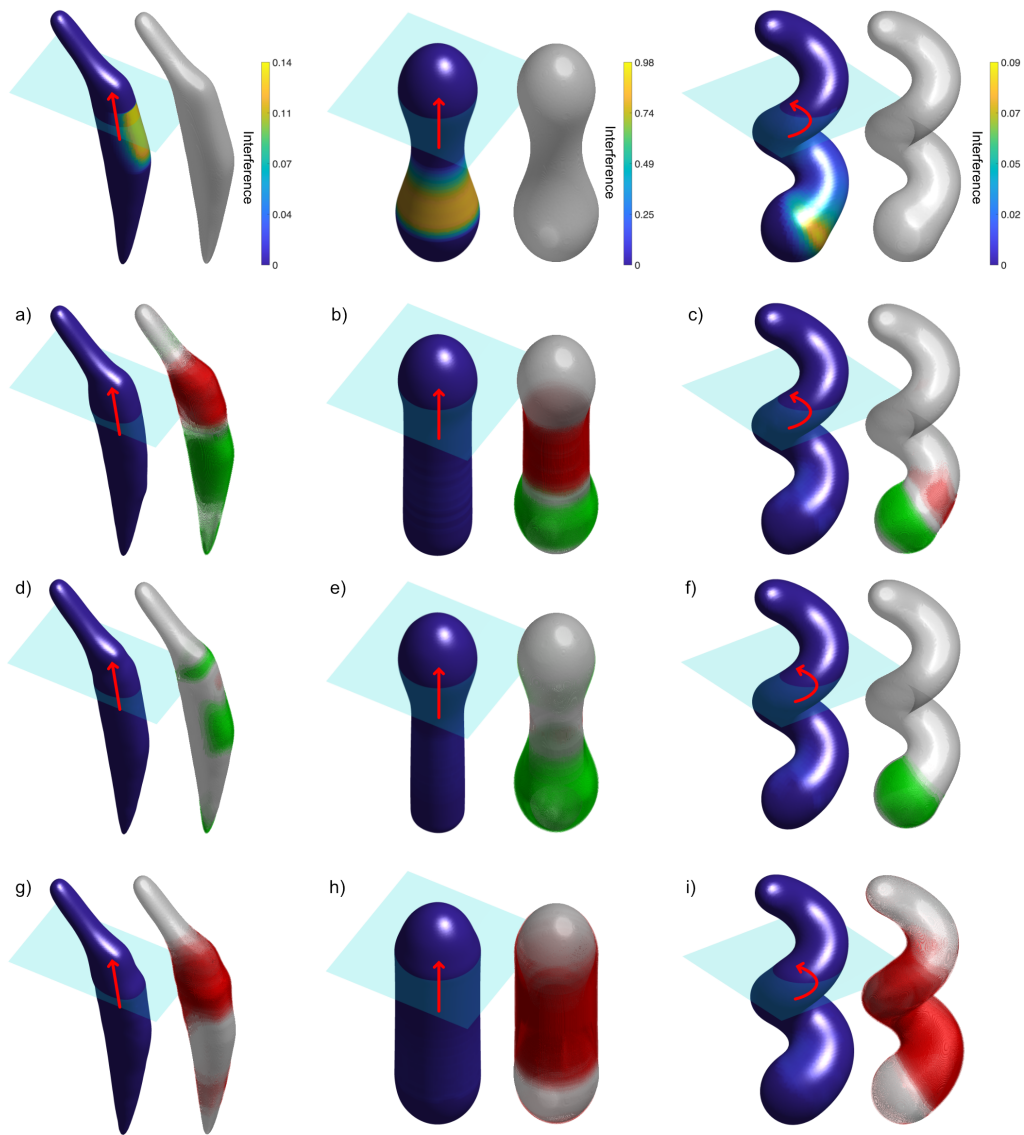
Fig. 4.8.: Various 3D body-cavity systems modified for insertability using Eq. 4.19 as design objective. The original designs (top row) fail to meet the local interference-free criterion at the highlighted areas (left). The modified designs (bottom rows) are presented along with the local shape change from the original design (right). Red and green refer to added and removed material, respectively. The third and fourth rows use the space-filling and space-making variations of the shape-match functions. All designs were generated on 500 000 node level set meshes with a filter radius of $r = 4$.
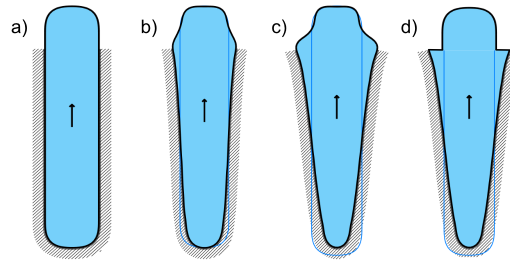
Fig. 4.9.: (a)-(c) Three versions of a straight rod, each modified for insertability with different ε values. From left to right, $\varepsilon = 0$, $\varepsilon = -1 \times 10^{-2}$, $\varepsilon = -1 \times 10^{-1}$. (d) shows how the exterior portion of the design in (c) can be overwritten with the original geometry from (a).

4.3.3 Discussion on parameters

Ease of insertion

The insertability constraint is defined as an inequality with the right side set to zero. This, in effect, allows for pure sliding motion along the body-cavity interface. In certain applications, such as in automated assembly, this can result in designs that are difficult to insert. If, for example, the body and cavity have rough surfaces, the resulting friction may require high forces or prevent insertion entirely. This can be addressed by setting the right side of the inequality constraint to $\varepsilon <= 0$. Fig. 4.9 shows how the design of a straight bar is affected for various values of ε.

Filter radius

A minor issue highlighted by these results is the unnecessary dilation near the cavity opening. This results from the filtering stage described above. While it may be possible to eliminate this issue by increasing the tuning parameters in the projection stage, it is generally sufficient to replace the exterior portion of the modified design with that of the original, as shown in Fig. 4.9(d).

We note that in some cases, the modified design does not maximally fill the cavity. In cases 2 and 3, for example, the implant should touch the bottom of the cavity, but does not. This is likely related to the filtering and may be addressed by either adjusting the tuning parameters or refining the level-set grid.
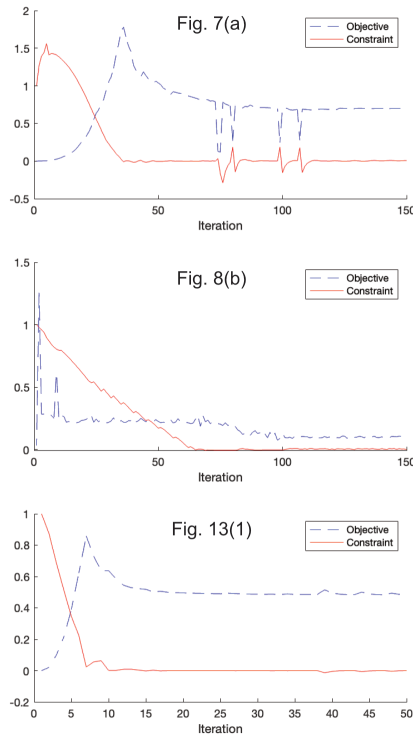
Fig. 4.10.: Optimization history for three case studies, one for each of the 2D, 3D and 3D acetabular cup sets.

4.3.4 Convergence

The convergence history for a selection of the case studies, chosen at random, is shown in Fig. 4.10. In all cases, the interference constraint is initially normalized. The optimization history reveals a generally smooth evolution in which the design is first changed significantly at the expense of the objective function, in order to bring the interference constraint below zero. Subsequent iterations minimize the shape match objective. The optimization tends to converge within less than 100 iterations. Note that in the 2D case (Fig. 7(a)), the observed instability between iterations 75 and 110 results from a coarse mesh discretization and a large step size.

4.4 Application to the design of acetabular cups

Orthopedic implants are medical devices used to replace damaged or missing bone tissue in an effort to improve the patient's mobility, reduce pain, and generally improve quality of life. Traditional implant systems include a set of generic implant
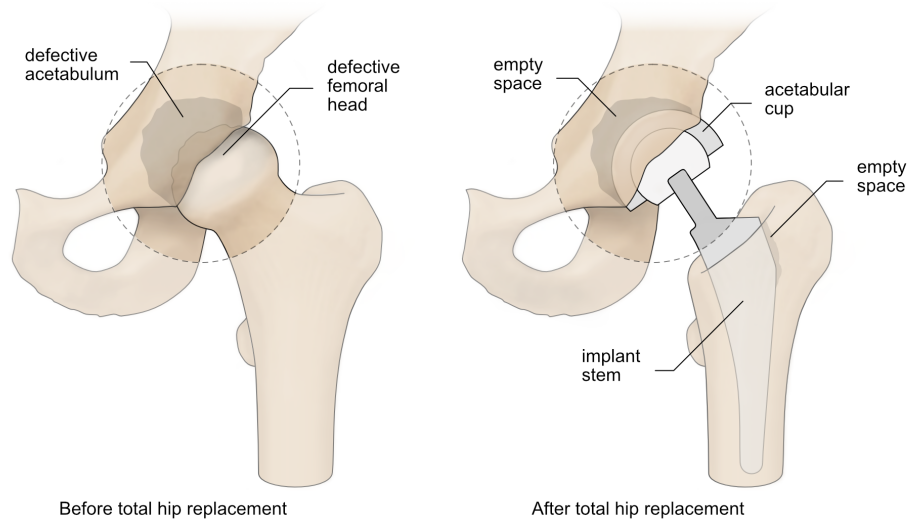
Fig. 4.11.: An illustration of the total hip replacement (THR) procedure with a generic hemispherical acetabular cup. Reaming ensures proper contact between the bone and cup along the exterior, but pockets are present on the interior. Screws (not shown) may be included to help stabilize the cup.

shapes and sizes to help find the best fit. However, patient-specific implants (PSI), designed according to a patient's unique anatomy, may offer better outcomes than their traditional counterparts. Some of the expected benefits of patient-specific implants include: better positional accuracy of the joint, reduced risk of complications, and reduced recovery times [138, 139, 93].

A particularly challenging aspect in the design of patient-specific implants is the need to optimize functional compatibility between the implant and the surrounding bone tissue, while also ensuring that the implant can be inserted without causing damage to itself or to the peri-prosthetic tissue. The method presented in this work is ideally suited to address these potentially conflicting design objectives. In this section, we demonstrate how our insertability constraint can be applied to the design of an acetabular cup, considering both geometric and structural objectives, via finite element analysis (FEM).

The acetabular cup is the female component of a hip replacement implant (Fig. 4.11). It is a typically hemispherical component that is placed in the acetabulum, which is the socket of the pelvis that forms the hip joint. Traditionally, orthopedic surgeons determine the ideal diameter of the cup from a range of options, based on patient-specific measurements. However, since the surface of the acetabulum is not perfectly hemispherical, there is always some morphological mismatch between the cup and the acetabulum. This mismatch may reduce the implant's stability and cause damage to the surrounding cortical bone.
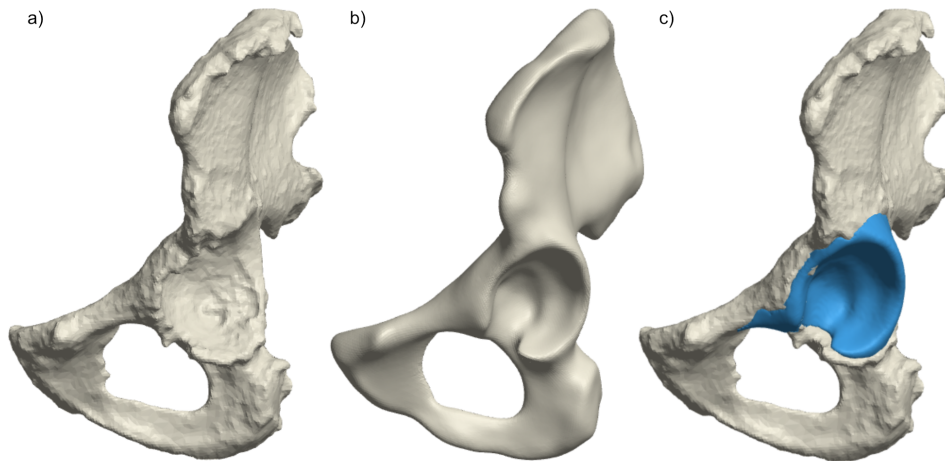
Fig. 4.12.: (a) A Paprosky classification type IIA defective pelvic bone extracted from CT data; (b) the reconstructed healthy bone obtained using the statistical shape modeling by [95]; (c) the defective pelvic bone with the recovered acetabular tissue highlighted.

As a first approach, we can apply the shape-matching formulation subject to our insertability constraint, as described above. However, we must first generate a morphologically matched implant design to use as a starting point. This can be achieved by performing a CT scan of both hips and extracting the difference between the healthy and defective anatomy. If both hips are anatomically defective, we may use a computational model to obtain an approximate reconstruction of the original healthy bone. In this work, we use a pre-processed set of defective and reconstructed pelvis geometry obtained from [95]. The defective pelvis, which is classified as type IIA according to the Paprosky classification system, is reconstructed using a statistical shape model based on data from 90 patients. By comparing the defective geometry, shown in Fig. 4.12)(a) with the reconstructed healthy geometry, shown in Fig. 4.12)(b), we can identify the missing acetabular tissue and the ideal bone-implant contact surface. The missing tissue geometry is then used to create an implant with a perfectly matching bone contact surface, as well as the required hemispherical bearing surface for the synthetic joint, as shown in Fig. 4.13.

Results of the design process are presented in Fig. 4.14. Each column shows a different view of the implant-bone contact surface. The top row shows the values of the local insertability metric. The areas which prevent insertability are highlighted with circles. The bottom row shows the optimized implant with the local shape change shown in red and green. In this case, since cortical bone tissue can be resected but not added, green areas represent gaps between the implant and the

Positioned acetabular implant   Segmented acetabular implant

Reconstructed hip geometry

Bone contact surface

Spherical bearing surface
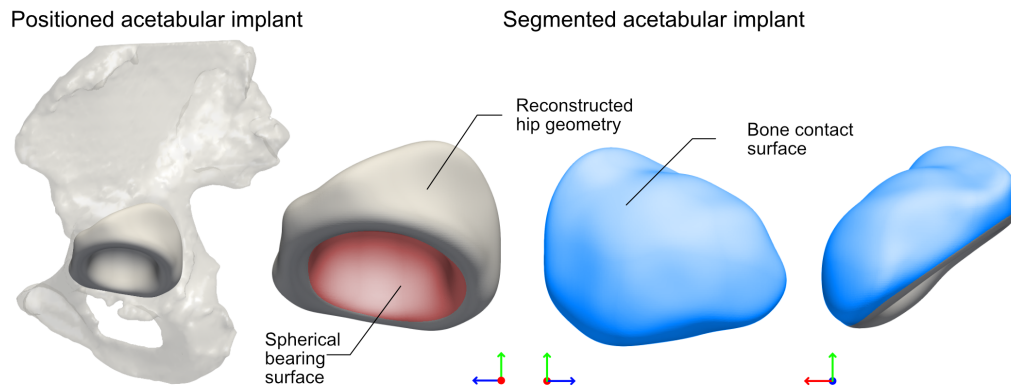
Fig. 4.13.: The initial implant level set based on the geometry of the missing acetabular tissue. The bone-implant interface is highlighted in blue while the modified spherical bearing surface, required for finite element analysis, is highlighted in red.

bone. We can observe that the shape changes are concentrated on either side of the implant and that, for each, inwards and outwards changes are paired. This coupling makes the local surface parallel to the insertion direction, as would be expected for the nearly linear insertion path shown.

If indicated, space-filling and space-making may be used instead. The space-filling design will preserve as much of the cortical bone tissue as possible but will result in some morphological mismatch. On the other hand, the space-making design will ensure a perfect contact surface but requires some bone resection.

Beyond the purely geometric shape-matching functions, more sophisticated objectives based on structural analysis of the bone-implant system may be considered. For example, we may aim to minimize the risk of implant slipping and loosening by assessing the global Hoffman failure criterion [64]. This function assesses the local risk of interface fracture based on the cortical bone properties and the local stress conditions throughout the interface. With the Hoffman index set as the optimization objective and the insertability criterion set as the only constraint, an reduction in the Hoffman index of 94% is achieved (Fig.4.15). The Hoffman criterion and the associated finite element methods are presented in [50]. Details regarding loads and boundary conditions are included in the supporting information section.

$V_{in} = 0.42\%$ $V_{out} = 0.35\%$

$V_{in} = 0.87\%$ $V_{out} = 0.00\%$

$V_{in} = 0.00\%$ $V_{out} = 0.76\%$
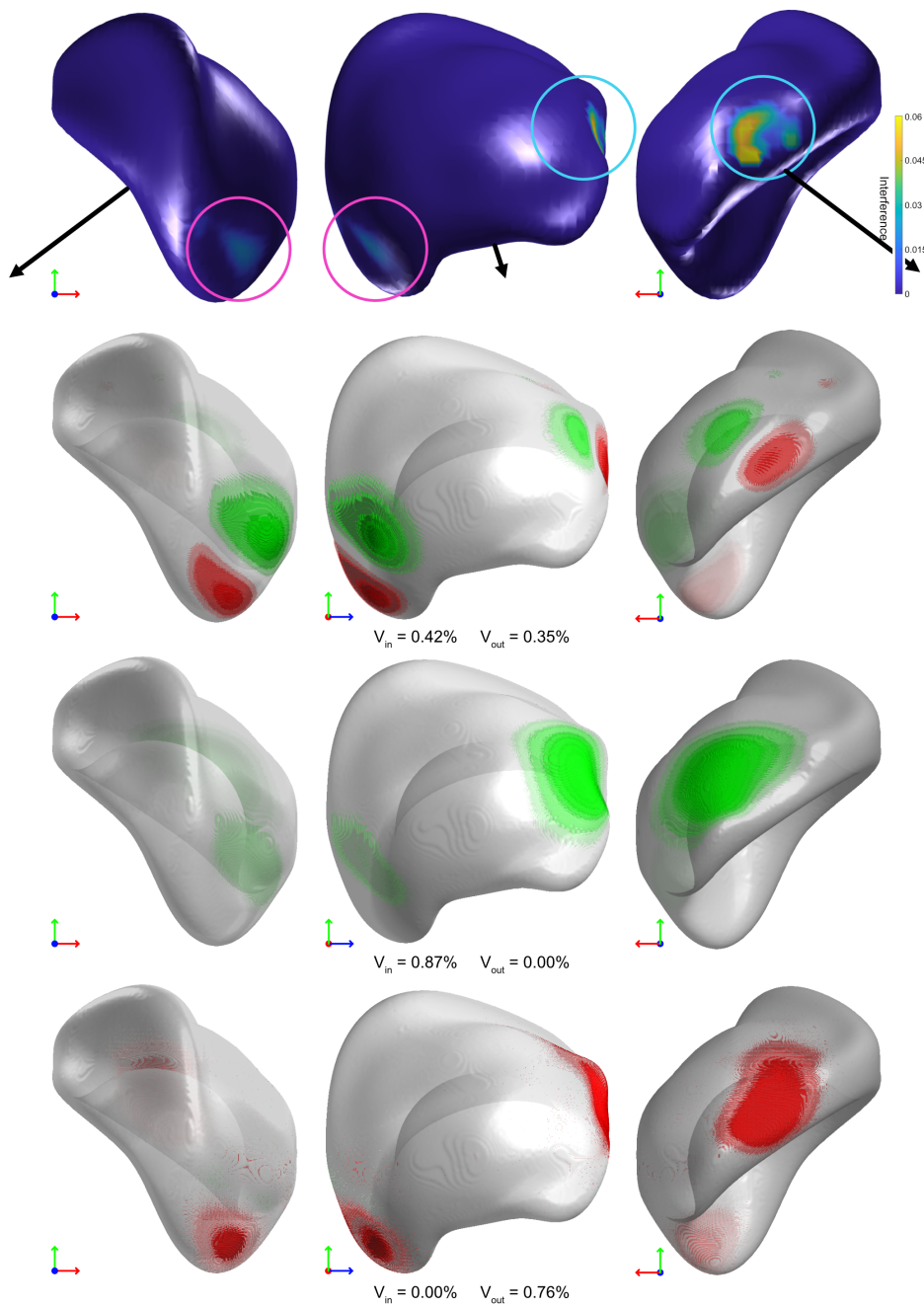
Fig. 4.14.: Row 1: Original implant design with local interference shown. Row 2: Implant modified using the standard shape-matching objective. Row 3: Implant modified using the space-filling objective. Row 4: Implant modified using the space-making objective. The added material (red) corresponds to local bone tissue resection, and the removed material (green) corresponds to gaps with the surrounding bone tissue. V_{in} and V_{out} represent the total inward and outward volumetric change, normalized to the initial design volume.

Fig.	Parameters			Initial insert. $\hat{\mathcal{I}}_0$	Final shape change			Hoffman risk	
	α	β	ε		In.	Out.	Total	Initial	Final
4.6(a)	1	1	0	0.5049	0.0379	0.0510	0.0889	—	—
4.6(b)	1	1	0	0.0456	0.0887	0.1116	0.2003	—	—
4.6(c)	1	1	0	0.0811	0.0253	0.0258	0.0511	—	—
4.6(d)	1	1	0	0.0814	0.0578	0.0443	0.1020	—	—
4.7(a)	1	1×10^2	0	0.5049	0.0635	0.0056	0.0691	—	—
4.7(b)	1	1×10^3	0	0.0456	0.2871	0.0122	0.2994	—	—
4.7(c)	1	1×10^2	0	0.0811	0.1758	0.0185	0.1943	—	—
4.7(d)	1	1×10^2	0	0.0814	0.0306	0.0009	0.0315	—	—
4.7(e)	1×10^3	1	0	0.5049	0.0021	0.2213	0.2234	—	—
4.7(f)	1×10^3	1	0	0.0456	0.0004	0.3192	0.3196	—	—
4.7(g)	1×10^3	1	0	0.0811	0.0007	0.0363	0.037	—	—
4.7(h)	1×10^3	1	0	0.0814	0.0022	0.0669	0.0691	—	—
4.8(a)	1	1	0	0.2560	0.1179	0.0776	0.1955	—	—
4.8(b)	1	1	0	0.6158	0.0955	0.1082	0.2037	—	—
4.8(c)	1	1	0	0.1906	0.0343	0.0170	0.0513	—	—
4.8(d)	1×10^3	1	0	0.2560	0.0700	0.0022	0.0721	—	—
4.8(e)	1×10^3	1	0	0.6158	0.3305	0.0061	0.3366	—	—
4.8(f)	1×10^3	1	0	0.1906	0.0549	0.0002	0.0551	—	—
4.8(g)	1	1×10^2	0	0.2560	0.0009	0.1539	0.1548	—	—
4.8(h)	1	1×10^2	0	0.6158	0.0002	0.2957	0.2959	—	—
4.8(i)	1	1×10^2	0	0.1906	0.1729	0.0000	0.1730	—	—
4.9(a)	1	1	0	0	0	0	0	—	—
4.9(b)	1	1	-5×10^{-3}	0	0.0794	0.0648	0.1442	—	—
4.9(c)	1	1×10^2	-1×10^{-2}	0	0.1443	0.1251	0.2694	—	—
4.14(1)	1	1	0	0.0455	0.0315	0.0261	0.0576	1	9.946
4.14(2)	1	1×10^2	0	0.0455	0.0640	0.0007	0.0647	1	7.843
4.14(3)	1×10^3	1	0	0.0455	0.0004	0.0704	0.0708	1	0.794
4.15	—	—	—	0.0455	0.0647	0.0240	0.0888	1	0.075

Tab. 4.1.: Problem parameters and performance values for each numerical experiment. The insertability metric values are normalized with respect to the mean body displacement, and the Hoffman risk index is normalized to that of the original design.

4.5 Discussion

The preceding examples demonstrate that the proposed insertability constraint can effectively and efficiently restrict the design of complex 2D and 3D structures subject to various geometry and structural requirements.

The method is implemented in MATLAB R2023a. All 2D and 3D results presented were computed on a laptop computer with M1 Max processor and 64 GB LPDDR5 RAM. The 2D shape optimization was performed with approximately $20\,000$ design variables and required 30 - 50 iterations, each performed in approximately 0.6 s.

The 3D results were performed with approximately $500\,000$ variables and required 40 - 100 iterations, at 8 - 10 seconds per iteration. Compared with our MATLAB implementation of the method presented by [69], the 2D insertability assessment was performed approximately $70\times$ faster, primarily due to the computation of a complete insertion path.

The level set-based optimization framework proved highly effective as a host for the insertability constraint. Performance improved monotonically throughout the optimization procedure and converged in less than 100 iterations for all the experiments. The algorithm proved capable of handling complex topology and cases with large rotations in both 2D and 3D. No parameter tuning was required between numerical studies.

4.5.1 Limitations

The main limitation of the insertability metric is that it reduces the cavity to an interface curve (2D) or surface (3D), thereby ignoring possible interference between the fixed cavity body and the external/extracted portion of the moving body. For this reason, under certain circumstances, the insertability criterion may potentially produce false positive results. Handling of this special case may require additional constraints and is left as a challenge for future research.

4.5.2 Notes on implementation

For problems in which significant rotation is required for insertion/extraction, it is critical to choose an appropriate reference frame origin. Otherwise, the sensitivities of the constraint with respect to the rotations in $\boldsymbol{\theta}$ may become very large. This is generally avoided by setting the origin to the centroid of the initial design.

The insertability constraint tends to be sensitive to the filter radius. In particular, significant instability has been observed for $r < 4$. While a relatively large filter radius does tend to reduce the design complexity for a given grid size, sharper projection and finer grid resolution help mitigate this issue.

In a real-world application, designs should take into account manufacturing-related uncertainties. Methods such as the one presented by [135] help account for local defects on internal stresses. In the case of the proposed insertability constraint, small surface imperfections may impede insertion. We demonstrated how this can potentially be mitigated by tailoring the ease of insertion parameter ε. However, a perfect

fit in the inserted configuration remains tied to the accuracy of the manufactured components. For this reason, manufacturing uncertainty should be incorporated into the optimization framework, alongside the insertability constraint.

4.6 Conclusion

We have demonstrated that the proposed insertability metric is able to efficiently assess the insertability of complex body-cavity systems, taking into account full 6 DOF motion. Beyond its use as a validation tool, the insertability metric can be applied as a constraint in the design and optimization of functional components where geometric or structural objectives are considered. The level set-based formulation allows for straightforward integration with many topology optimization approaches. Future work will focus on applying the insertability constraint to multi-scale optimization in which both the overall shape and the internal microarchitecture of the architected material are optimized simultaneously.

$V_{in} = 1.14\%$ $V_{out} = 0.95\%$
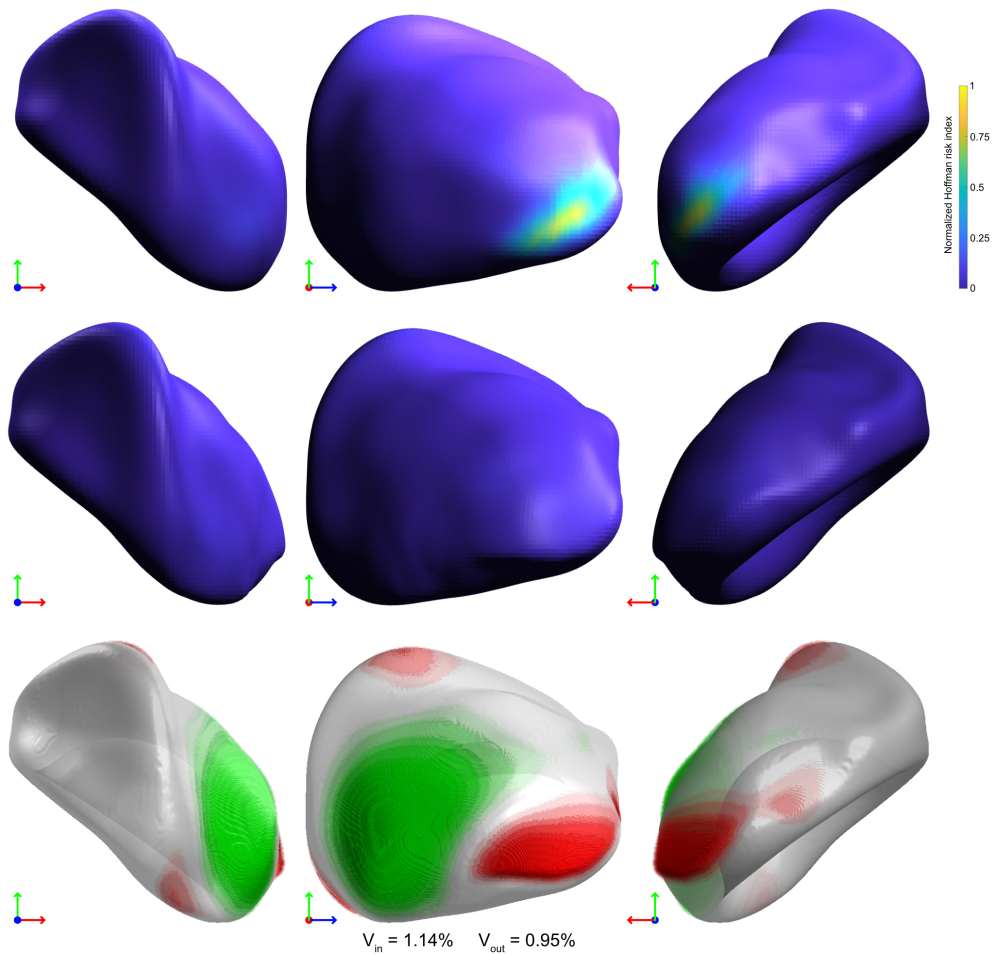
Fig. 4.15.: The original (top row) and modified (middle row) implant designs colored according to the local risk of interface fracture from [50]. In the bottom row, the local shape change is shown in terms of added (red) and removed (green) material. V_{in} and V_{out} represent the total inward and outward volumetric change, normalized to the initial design volume.

Automated design of bone-preserving, insertable, and shape-matching patient-specific acetabular components

Abstract

Effective treatment of severe acetabular defects is among the most challenging aspects of revision total hip arthroplasty (THA). Acetabular reconstruction requires careful consideration due to the deficiency of healthy bone stock and degradation of the support columns. Cementless hemispherical components with porous micro-architectures, which are largely preferred for their potential to provide biological fixation, are often unsuitable in revision cases, where the bone-implant contact may be insufficient for fixation, without significant reaming of the limited bone stock. A recently developed method for generating patient-specific acetabular components offers near-perfect bone-implant contact, with minimal reaming. These components can be manufactured using the same additive manufacturing methods as modern porous spherical components, and the associated implantation method is ideally suited to robotic arm-assisted surgery. This study simulates the performance of computationally designed patient-specific acetabular components from CT scans of patients set to undergo revision THA. The results show that the patient-specific components increase the bone-implant contact surface by $63 \pm 44\%$, and reduce the volume of reamed bone stock by $97 \pm 4\%$, (mean $\pm$ SD), as compared to standard hemispherical components.

5.1 Introduction

Total hip arthroplasty (THA) is one of the most frequently performed surgical procedures in current medical practice. In OECD (The Organisation for Economic Co-operation and Development) countries, 182 procedures were performed per 100 000 population in 2019, rising 22% since 2009 [102]). This increase is expected to be associated with a substantial rise in revision THA [137]. Revision procedures present significant challenges due to the loss of healthy bone stock and degradation of the load-bearing structures [108]. Acetabular reconstruction, in particular, requires careful pre-operative planning and may involve a variety of approaches, depending on the nature and severity of the defect [47].

In many revision cases, standard hemispherical components (with or without joint centroid offset) may not provide adequate bone-implant contact for biological fixation, without significant reaming of the remaining bone stock [129]. In these cases, surgeons typically opt for a cemented option [47]. Alternatively, they may use porous metal augments, which are placed in bone-deficient areas to help stabilize the acetabular component. Augments effectively extend the surface of the component to better match the defect morphology. They are, in a sense, built-in-place patient-specific implants. The use of these patient-specific components has revolutionized the treatment of severe acetabular defects over the last two decades, with mid-term reports showing excellent survivability [155, 140]. Nonetheless, the use of porous metal augments is labor-intensive and limited in its ability to accurately match the defect geometry, due to the finite set of augment shapes and sizes available [90].

Patient-specific acetabular components provide a more effective alternative. However, the typical approach involves manual analysis and design by expert engineers, surgeons, and technicians. This laborious and resource-intensive design process drives the cost of patient-specific implants out of reach, except in the most challenging cases. Recently, we have proposed an algorithm that can be used to automatically design shape-matching objects [49]. Here, we aim to apply this algorithm to automatically generate patient-specific acetabular components using standard-resolution CT scans while also maximizing bone-implant interface contact and simultaneously minimizing the volume of bone to be reamed.

The aim of this study, therefore, is to apply the above-mentioned algorithm to automatically generate implants based on a sample of real pelvis defects, and quantify the potential performance improvement as compared to traditional hemispherical components.

The remainder of this paper is organized as follows: Section 2 reviews the design algorithm and relevant performance metrics. Section 3 presents numerical results and analysis. Finally, section 4 concludes with comments and suggestions for future work.

5.2 Materials and Methods

5.2.1 Dataset of acetabular defects

A specific sample of 15 acetabular defects was selected from a dataset of 90 3D models generated by Meynen *et al.* [95]. The study, which was approved by the ethical committee of the university hospital Leuven (S61746), used unilateral CT scans of revision THA patients, after excision, and prior to re-implantation. The sample used in this study was selected based on the results of a statistical shape model analysis [96], accounting for 73% of the total shape variation found in the original dataset. For each of the first five shape modes, three cases were selected to represent the mean and mean $\pm$ one standard deviation.

5.2.2 Automated design of patient-specific cups

Patient-specific acetabular components were computationally generated using an algorithm presented in [49]. The design strategy aims to optimize the outer geometry of the component to best match the morphology of the acetabular defect, while ensuring that the optimized structure is insertable through rigid body motion, *i.e.*, without damaging the surrounding bony tissue.

Interface matching and insertability

An implant with surface geometry perfectly complementary to the acetabulum would produce ideal bone-implant contact. However, such an implant would not necessarily be insertable. The design strategy proposed in [49] addresses this issue by identifying the areas that inhibit insertion along a certain path, as shown in Fig. 5.1. Specifically, the algorithm simulates the implant in its inserted configuration, and assesses the surface translations induced by a small extractive movement along a specific path. Generally speaking, if the translation is *into* the interface at any point,
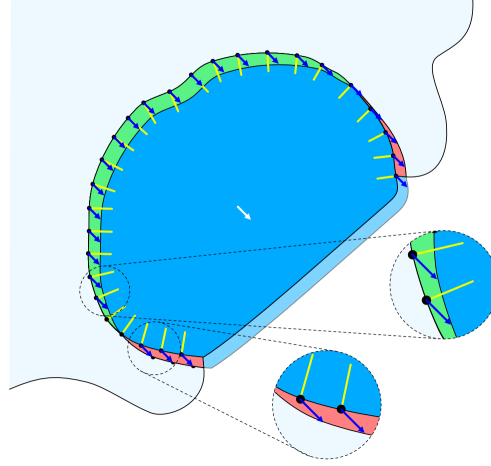
then local interference is detected, and the implant is deemed uninsertable along this insertion/extraction path.

Constrained by this insertability requirement, the algorithm iteratively modifies the implant geometry and the insertion path in order to find an insertable design, while minimizing changes to the implant's shape. Mathematically, we formulate an optimization problem in which the interface geometry, described by ρ, is modified to minimize a shape change function F_S, while respecting an insertability constraint:

$$\underset{\rho,(\mathbf{p},\boldsymbol{\theta})}{\text{minimize}} \quad F_S = \frac{1}{n}\sum_{i=1}^{n}|\mathrm{d}(\mathbf{b}_i, S_0)| \tag{5.1}$$
$$\text{subject to} \quad r_b^n(\mathbf{p},\boldsymbol{\theta}) \geq r_{min}^n(\mathbf{p},\boldsymbol{\theta})$$

where $\mathrm{d}(\mathbf{b}_i, S_0)$ is the closest distance from a point b_i on the evolving body surface to a point cloud describing the original geometry S_0. $(\mathbf{p},\boldsymbol{\theta})$ describes the insertion direction in terms of translation and rotation vectors $\mathbf{p}$ and $\boldsymbol{\theta}$, and r_{min}^n is a minimum local normal displacement defined by the local tangential displacement r_b^t and curvature κ_b:

$$r_{min}^n = \begin{cases} \kappa^{-1} - \sqrt{\frac{\kappa^{-2}(r_b^t(\mathbf{p},\boldsymbol{\theta}))^2}{\kappa^{-2}-(r_b^t(\mathbf{p},\boldsymbol{\theta}))^2}} & \text{if } \kappa_b > 0 \\ 0 & \text{otherwise} \end{cases} \tag{5.2}$$
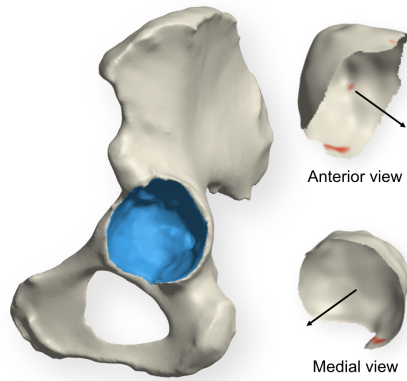
Fig. 5.2.: Left: A sample pelvis with acetabular surface highlighted. Right: The extracted acetabulum with insertion-inhibiting areas highlighted, for the insertion direction shown.

We refer to [49] for a detailed explanation of the optimization problem and solution strategy.

Anatomical restoration

The anatomical features surrounding the acetabulum, such as the acetabular margin and supraacetabular groove, are obtained from a statistical shape model reconstruction of the healthy pelvis [95]. This is achieved by superimposing the defect and reconstruction geometry and extracting the volumetric difference. The reconstructed healthy pelvis also provides the optimal center of rotation for the artificial joint. The reconstructed acetabular surface is replaced by a hemisphere component, so as to provide support for a standard $36\,\text{mm}$ polyethylene or ceramic liner (Fig. 5.3). In a real-world use case, additional features, such as holes for locking screws, friction-enhancing features, and liner-retaining lips or grooves may be added, as per surgical requirements.

5.2.3 Reference cup selection

In this study, standard hemispherical components were used as a performance benchmark. An automated selection and implantation strategy was designed to ensure optimal sizing and placement. First, the centroid of the defect was identified as the spatial coordinates that minimize the radial distance variance of rays projected onto the acetabulum, as shown in Fig. 5.4 (left). The component radius was then
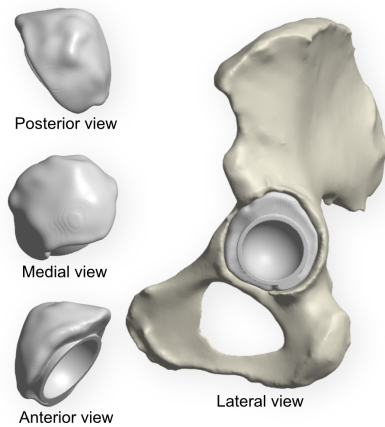
Fig. 5.3.: An automatically designed patient-specific acetabular component fitting the acetabular defect shown in Fig. 5.2. The acetabulum-side surface is optimized to fit the defect geometry while the outer geometry is designed to ensure accurate positioning of the synthetic joint.

chosen to provide a contact of 50%, with respect to the surface area of the component (Fig. 5.4 (right)). In many cases, achieving the desired contact ratio created or enlarged an already existing central segment discontinuity. In cases of extreme bone deficiency, 50% contact was not always possible. In these cases, the maximum a _____ id.
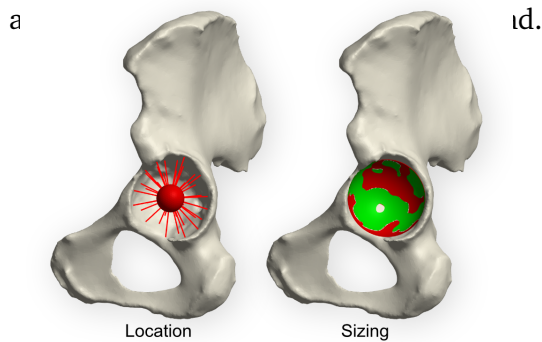
Fig. 5.4.: Selection of the reference hemispherical cup. The joint centroid is located by projecting rays onto the acetabulum (red lines). The contact and non-contact surfaces are shown in green and red, respectively. The white region along the central segment is a discontinuity created by the associated reaming process.
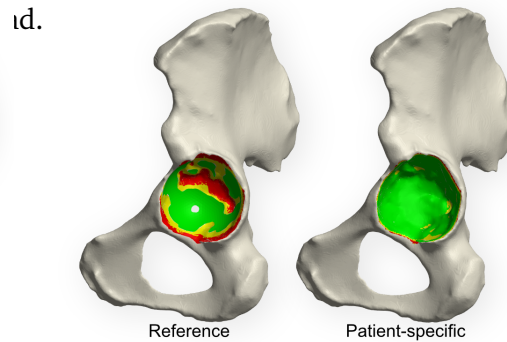
Fig. 5.5.: Bone-implant interface contact for the reference hemispherical component (left) and patient-specific optimized component (right). Contact regions and no-ingrowth regions are shown in green and red, respectively. Regions with interface gap smaller than $1\,\mathrm{mm}$ are shown in yellow.

5.2.4 Performance analysis

Performance was quantified based on two metrics: bone-implant interface contact and volumetric bone loss. Infection or inflammation-related failure, and instability-related issues are the most common diagnoses associated with implant failure [116, 89, 105]. While neither can be directly accounted for at the time of implantation, both are thought to be related to initial interface contact and/or volumetric bone loss [20, 140, 109].

Bone-implant interface contact

Interface contact was quantified in terms of the absolute contact surface area (within $50\,\mu\mathrm{m}$) and the fractional contact area relative to the surface area of the acetabulum prior to resection. The total area with gap larger than $1\,\mathrm{mm}$, for which no bone ingrowth is expected [37], was also measured. Fig. 5.5 shows the contact and no-ingrowth regions for the patient-specific and reference hemispherical implants, corresponding to the defect in Fig. 5.4. The relative improvement in terms of interface contact A_c^{rel} is defined as:

$$A_c^{rel} = \frac{A_c^{p.s.}}{A_c^{ref}} - 1 \qquad (5.3)$$

where $A_c^{p.s.}$ and A_c^{ref} are the total contact surface areas for the patient-specific and reference components, respectively.

In this case, the minor interface gaps correspond to small pitting along the acetabular surface, which are too small for the design algorithm to capture. The only exception is the larger cavity on the posterior-inferior surface, which could not be filled without sacrificing insertability, as highlighted in Fig. 5.2).

Volumetric bone loss

The total bone loss resulting from the required reaming was evaluated by simulating the resection process and measuring the total change in bone volume through high-resolution voxelization (1 million voxels). Fig. 5.6 shows the resection depth together with original and reamed pelvis geometry, corresponding to the defect shown in Fig. 5.4.
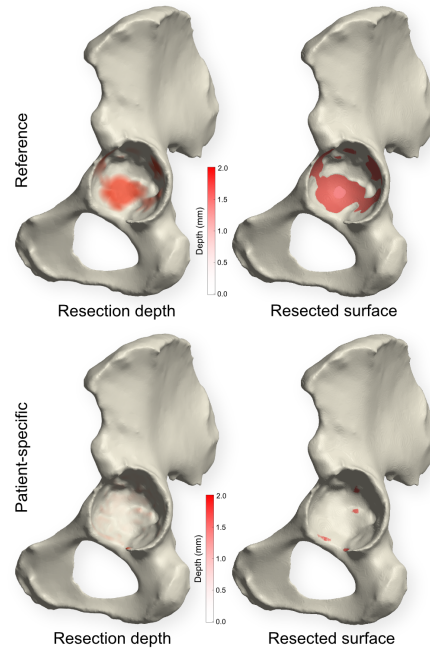
Fig. 5.6.: Resection depth (left) and the resected surface (right) for the reference hemispherical (top) and patient-specific optimized (bottom) components, for the defect shown in Fig. 5.4.

The relative reduction in bone loss V_{loss}^{rel} is defined as:

$$V_{loss}^{rel} = \frac{(V_{loss}^{ref} - V_{loss}^{p.s.})}{V_{loss}^{ref}} - 1 \tag{5.4}$$

where $V_{loss}^{p.s.}$ and $(V_{loss}^{ref}$ are the volume of bone resected for the patient-specific and reference components, respectively.

5.3 Results

Analysis of the specific defect case shown in the above figures reveals an increase in bone-implant contact area from $2494\,\mathrm{mm}^2$ to $4858\,\mathrm{mm}^2$, which corresponds to a 95% improvement. Additionally, the total acetabulum area with bone-implant gap larger than $1\,\mathrm{mm}$ decreased by 98%. With respect to bone preservation, the total volume of reamed bone decreased from $1995\,\mathrm{mm}^3$ to $36.63\,\mathrm{mm}^3$, representing a reduction of 98%. Analysis of the other defects sampled shows similar improvement, both in terms of contact area ($63 \pm 44\%$; mean $\pm$ SD), and bone preservation ($97 \pm 4\%$; mean $\pm$ SD). Results pertaining to each defect are presented in Figs. 5.7 - 5.8 and Table 5.1. In all the considered cases, a reduction in bone loss of at least 88%

Figure	Shape mode	Paprosky class.	Reference component			Patient-specific component		
			Contact (mm^2)	Contact ratio	Resection (mm^3)	Contact (mm^2)	Contact ratio	Resection (mm^3)
5.7(a)	1	2B	2512	42%	1667	5679	96%	9.45
5.7(b)	$1 + \sigma$	3A	3966	55%	1485	6589	91%	29.01
5.7(c)	$1 - \sigma$	2A	2494	48%	1995	4858	93%	36.63
5.7(d)	2	2B	4149	46%	12 394	6913	76%	83.86
5.7(e)	$2 + \sigma$	3B	4167	50%	28 527	3859	46%	3210.61
5.7(f)	$2 - \sigma$	2A	2264	46%	1638	3946	79%	188.37
5.7(g)	3	2B	2179	26%	9495	5405	64%	570.50
5.7(h)	$3 + \sigma$	3B	3099	40%	16 288	4664	60%	1252.45
5.8(i)	$3 - \sigma$	2C	3345	69%	8957	4042	83%	60.31
5.8(j)	4	3B	3049	42%	12 751	5159	71%	339.96
5.8(k)	$4 + \sigma$	3B	3284	86%	8791	2726	71%	100.27
5.8(l)	$4 - \sigma$	3B	2296	57%	1576	3466	86%	14.10
5.8(m)	5	3A	2901	50%	1459	5502	94%	4.59
5.8(n)	$5 + \sigma$	2B	4856	48%	30 251	7001	69%	775.37
5.8(o)	$5 - \sigma$	2C	2743	52%	1760	4664	89%	15.87

Tab. 5.1.: Performance results for all defects sampled.

was observed. Interface contact varied widely from one defect to another, with a minimum contact ratio of 64%, with respect to the acetabular surface, and a net improvement compared to the reference component in 13 of the 15 defects sampled.

Inspection of the reference and patient-specific designs also suggests a significant improvement in the structural integrity of the final reamed bone. In particular, the reaming associated with the reference components often resulted in the creation or enlargement of discontinuities along the central segment. In some cases, the anterior-superior or posterior-inferior support columns were also compromised. The reaming associated with the patient-specific components was typically localized around the acetabular margin and does not appear to affect the structural integrity of the bone.

5.4 Conclusions and discussion

The objective of this study was to evaluate the performance of a novel patient-specific acetabular component design strategy as compared to standard hemispherical components. Specifically, bone-implant interface contact and resected bone volume were selected as the most relevant performance indicators. The results indicate a marked improvement in both metrics, with near-complete bone preservation in all cases, and over 60% increase in bone-implant contact, on average.

5.4.1 Additional benefits

Beyond the performance metrics studied in this work, this patient-specific component design strategy offers several additional benefits. The complementary irregular

interface ensures proper orientation of the component, thereby guaranteeing the exact positioning of the artificial joint centroid. The irregular shape also naturally provides higher rotational resistance as compared to a hemispherical component, potentially reducing the required press-fitting load and the risk of press-fitting-related trauma. The automated design strategy can also be used to identify the ideal positions for additional fixation, such as screws, rings, or cages. Holes and attachment features can be added in the design stage, for a more streamlined surgical procedure.

5.4.2 Accuracy

The designs presented in this work are based on standard medical CT scans, with a resolution of approximately $0.5\,\mathrm{mm}$. While this is likely sufficient for the current application, small protrusions not visible in the scan may cause interference during insertion of the component. To address this issue, the 3D scanning system mounted to the robotic arm can be used to inspect the acetabulum prior to reaming, and adjust the reaming path if any sub-millimeter protrusions are detected. This can be achieved by comparing the original acetabular surface reconstruction with the one generated by 3D scanning. Protrusions are identified as any intersection between the two surface reconstructions.

5.4.3 Challenging cases

Cases with abnormal bone growth and lacking clear acetabular margins, such as the defect shown in Fig.5.7(g), may require user input to ensure that the algorithm correctly identifies the acetabulum. Otherwise, insertion-inhibiting structures may not be detected.

5.4.4 Future work

The automated design strategy studied in this work focused on the shape-matching aspect of patient-specific implant design. Another promising research direction involves the use of 3D-printable lattice structures to elicit favorable mechanical stress conditions in the surrounding bone tissue and along the bone-implant interface. Prior research has demonstrated that the predicted bone resorption and risk of interface fracture may be significantly reduced by employing such a design strategy [50].

In the future, these two approaches may be combined to simultaneously target geometric and structural performance objectives.
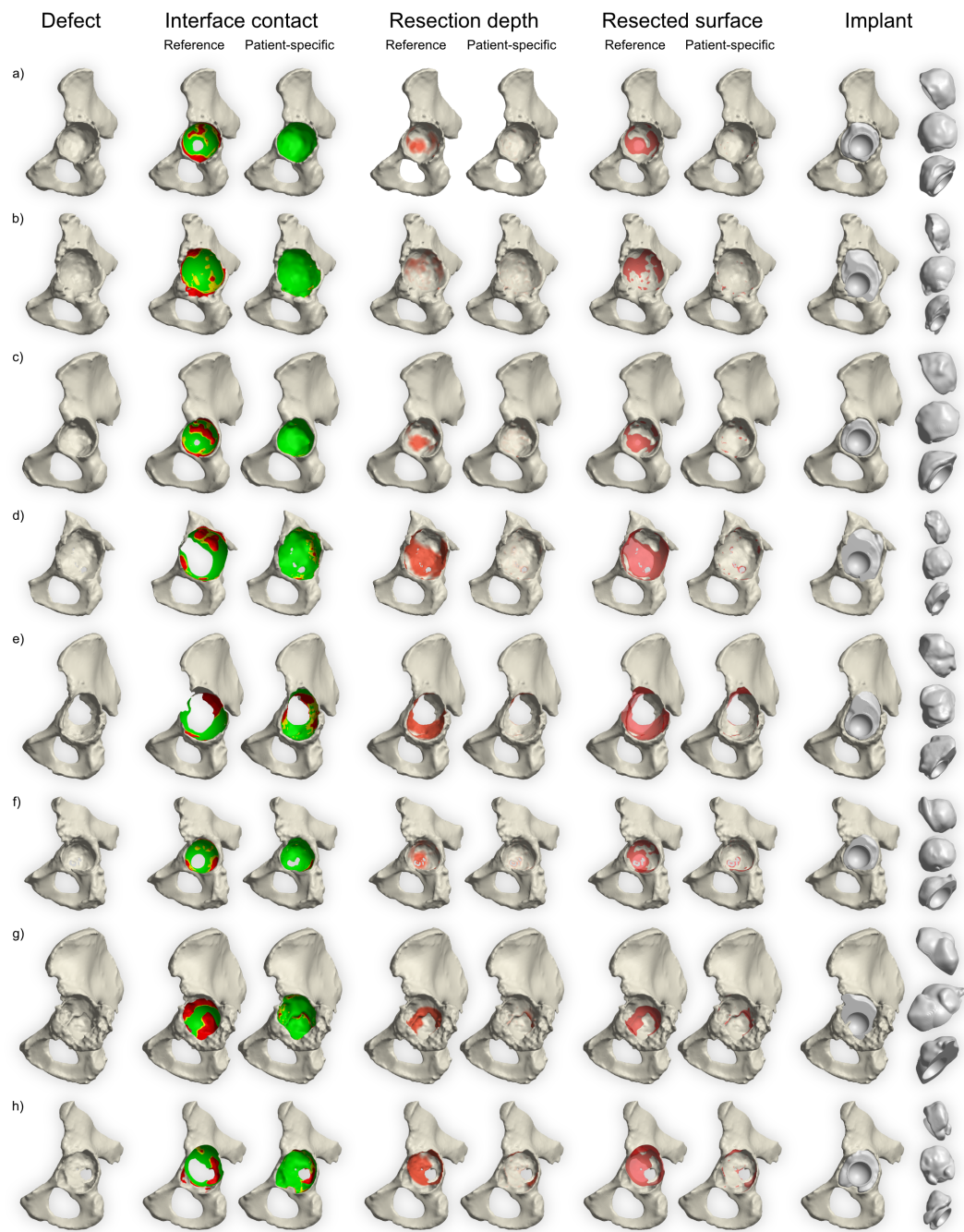
Fig. 5.7.: Results of the performance analysis for defects 1 through 8, shown in the left column. For each metric, the reference and patient-specific component performance are shown side-by-side.
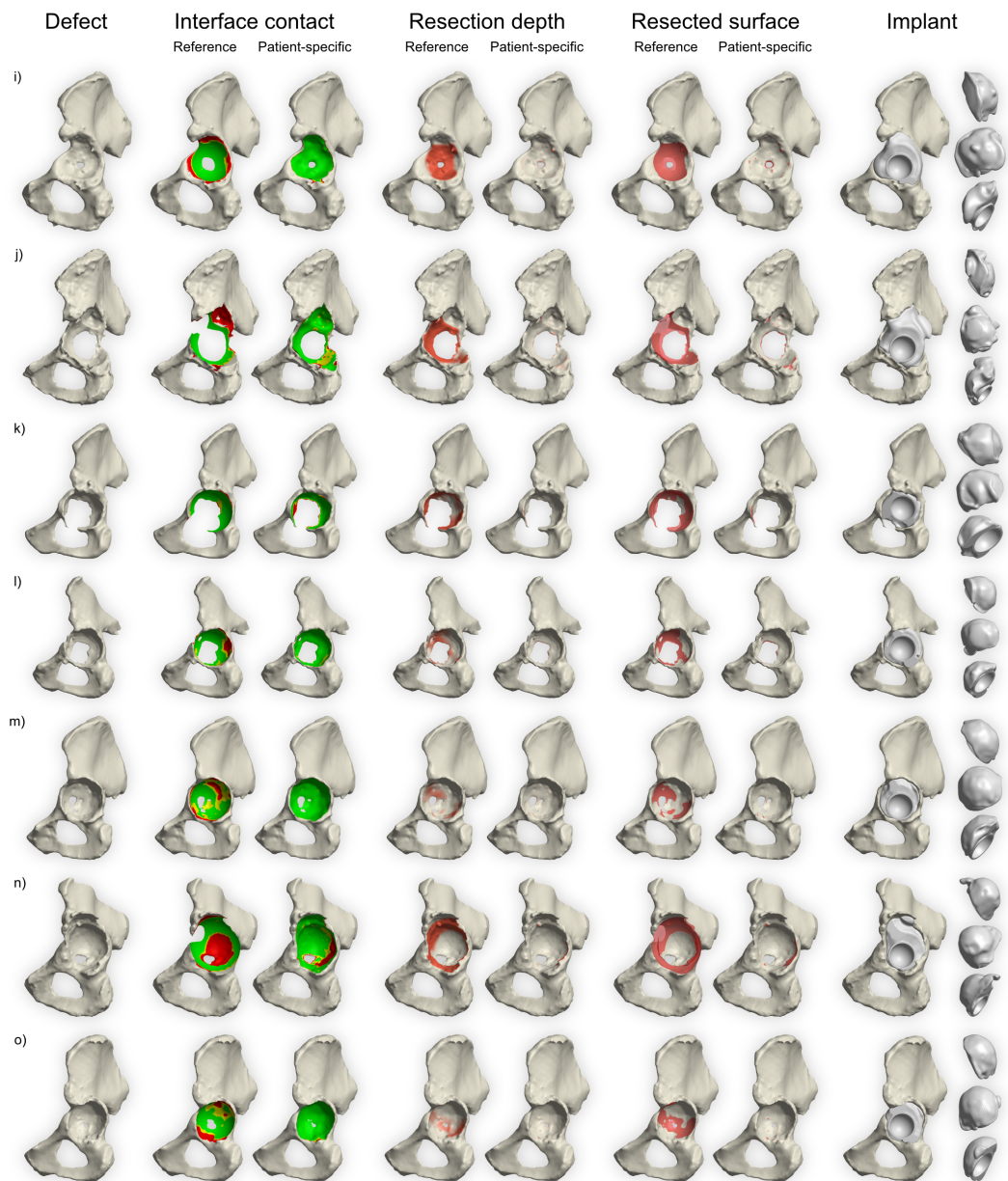
Fig. 5.8.: Results of the performance analysis for defects 9 through 15, shown in the left column. For each metric, the reference and patient-specific component performance are shown side-by-side.

Conclusions and discussion

6

6.1 Conclusions

From its inception, this research project set out to develop and apply methods from the field of numerical optimization to the design of orthopedic implants. In doing so, the work presented in this manuscript has made several contributions both to the field of numerical optimization and to the field of orthopedic research.

Chapter 2 presented a new strategy to address the issue of adjacent cell compatibility in multi-scale topology optimization. The proposed super-cell approach encourages individual unit cells to evolve towards compatible designs, without restricting the design space or imposing fixed geometry along their boundaries. This concept proved capable of generating mutually compatible unit cells, which could subsequently be used as a finite set of building blocks for decoupled multi-scale optimization. The proposed method was also successfully applied to concurrent multi-scale optimization, wherein each unit cell is allowed to evolve its own unique structure.

Chapter 3 presented an alternative to unconstrained multi-scale optimization. Instead, a novel parametric micro-architecture was developed to achieve a wide range of mechanical properties, while respecting local geometric constraints, such as a prescribed minimum length scale, bounded porosity, and bounded pore size. This parametrization was incorporated into a multi-scale formulation in which local mechanical and geometric properties are interpolated from pre-computed data. This allowed for a significant reduction in computational complexity, thus enabling the solution of 3D multi-scale structural optimization on a standard workstation.

Chapter 3 also introduced specially designed functions to quantify the impact of an implant design on the surrounding bone tissue. In particular, a new bone remodeling metric was devised to quantify the total fluctuation in bone density resulting from the introduction of the implant. A second function was devised to estimate the risk of bone-implant interface fracture, taking into account realistic failure modes associated with porous anisotropic materials.

The novel micro-architecture and stress-related functions were then applied to the design of orthopedic hip stems. This required addressing several additional technical

challenges. The non-rectangular parametric design space, for example, required that only valid parameter combinations be allowed, for a given unit cell. This constraint was handled using a distance field-based penalization method through which invalid or undesirable parameter combinations were penalized, based on their proximity to the nearest acceptable combination. The same strategy was used to apply local geometric constraints, at no additional computational cost. In the end, the optimization strategy proved extremely stable and was able to produce implants with significantly reduced predicted bone remodeling, as compared to their solid counterparts – all without increasing the risk of interface fracture. In fact, in most cases, the micro-architected implant induced less bone remodeling than the soft material version, and less interface fracture risk than the solid version, effectively outperforming both benchmarks in terms of their respective strengths.

An important aspect of this work is that the proposed multi-scale optimization strategy is not tied to any particular parametric micro-architecture. It can, in fact, be used to optimize the spatial configuration of any parametric micro-architecture with desirable geometric or mechanical properties. For example, minimal surface micro-architectures that have recently been shown to improve osseointegration and possess predictable bio-degradation [166, 18, 167], could be parametrized for use with the proposed multi-scale approach.

Aside from mechanical compatibility, patient-specific implants should be optimized in terms of specific geometry-related objectives. They should avoid unnecessary bone resection, and they should provide maximum interface contact for optimal osseointegration. Well-established shape optimization strategies can normally handle these objectives. However, this specific application also requires that the implants be insertable. Chapter 4 presented an insertability metric which can be used to determine if a particular design is insertable into a matching cavity. It does so without information on the insertion direction, and without computing a complete insertion path. Beyond simple insertability analysis, the new metric is fully differentiable and can, therefore, be used to optimize body-cavity systems for insertability. Applied as a constraint and coupled with a shape preservation objective, the insertability metric has proven capable of handling 2D and 3D cases with complex geometry and topology. It was also able to handle cases of significant rotation along the insertion path and minimal clearance.

In Chapter 5, the insertability metric was used as a constraint in the design of patient-specific acetabular cups. There, the design objective was to minimize the amount of bone loss due to implant-associated reaming. For this, a biased shape-matching function was introduced. It ensured that, wherever possible, the implant surface

would match the local bone morphology. If not possible, the algorithm would favor small interface gaps over bone resection. The resulting designs demonstrated an impressive reduction in bone loss in all cases, and a significant increase in interface contact area, in most cases. Additionally, the fact that the proposed design strategy is fully automated is expected to significantly reduce the labour costs associated patient-specific implants, thereby potentially promoting more widespread availability.

Together, the methods developed and presented in this work have addressed some of the main impediments to the widespread use of numerical methods in the design of orthopedic implants. In doing so, we were able to create robust design routines that autonomously generated designs with significantly improved performance. In all, these results represent an encouraging first step toward the development and adoption of patient-specific implant design strategies in the orthopedics community.

6.2 Implications for future research

The work presented in this manuscript accounts for only a small part of a broad and extensive field of research and development. Research in material science continues to produce ever-better metallic and synthetic materials. Advances in chemical and bio-engineering have led to the development of bone ingrowth-inducing surface coatings [74, 4, 88], micro-architected materials designed to guide stem cell differentiation [29, 101], and even biodegradable materials [153, 30]. From the world of computational methods, statistical modeling, geometry processing and artificial intelligence have produced methods to categorize morphological variations [96], identify pathological features [103], and even reconstruct healthy bone geometry [95].

Nonetheless, the methods presented here represent a significant step in the development of patient-specific implants. In the future, alternative micro-architectures with desirable properties may be incorporated into the proposed multi-scale optimization strategy. The micro-architecture optimization and shape optimization strategies could also be combined to simultaneously target structural and geometric objectives. And, of course, ex vivo and, eventually, in vivo experimentation could be performed to validate these computational results.

Future research may also see the design and incorporation of other application-specific requirements. New design objectives may, for example, target the promotion of strain and surface geometry-related bone ingrowth. Future design strategies may attempt to model the effects of growth hormone on osseointegration, or even include

biodegradable materials in the design process. The world of orthopedic implant design is full of open challenges and promising design directions to explore.

6.3 Outlook and utilization in commercial applications

While still very much in the conceptual stage, these new design strategies represent a promising avenue for eventual commercialization. This path, though not without risks and challenges, would not necessarily require significant retooling of the current process. State-of-the-art prototyping and manufacturing using selective laser melting (SLM), for example, are ideally suited to the proposed design methods. Other aspects of the design and validation process, such as risk analysis and clinical validation would, of course, are required – but the necessary investment seems worthwhile, given these promising results.

Appendix: Chapter 3

<div style="text-align: right">A</div>

A.1 Sensitivity Analysis

In gradient-based optimization, the sensitivity of the objectives and constraints with respect to the design variables is required. In this work, both the bone remodelling and interface fracture risk objective functions sensitivity with respect to a generic design variable ϕ_i are computed via chain rule:

$$\frac{\partial F_x}{\partial \phi_e} = \sum_{i \in \mathbb{M}} \left(\frac{\partial F_x}{\partial \tilde{\phi}_i} \frac{\partial \tilde{\phi}_i}{\partial \phi_e} \right) \tag{A.1}$$

where F_x is either the remodelling function F_r or the interface fracture objective F_σ and $\tilde{\phi}_i$ is the filtered design variable ϕ_i.

The sensitivity of the objective with respect to the filtered design variable $\tilde{\phi}_i$ is obtained via an adjoint analysis

$$\frac{\partial F_x}{\partial \phi_i} = -\boldsymbol{\lambda}_i^x \frac{\partial \mathbf{k}_i}{\partial \phi_i} \mathbf{u}_i \tag{A.2}$$

where $\mathbf{u}_i$ are the displacements of the DOFs corresponding to element i, $\frac{\partial \mathbf{k}_i}{\partial \phi_i}$ is the sensitivity of the element stiffness matrix with respect to the design variable, and the vector $\boldsymbol{\lambda}_i$ contains the i'th element's DOFs of the adjoint vector. The adjoint field $\boldsymbol{\lambda}^x$ is the solution of the adjoint problem:

$$\mathbf{K} \boldsymbol{\lambda}^x = \frac{\partial F_x}{\partial \mathbf{u}} \tag{A.3}$$

where the right hand side is obtained through the finite element assembly of the element contributions of, in the case of the bone remodelling objective

$$\frac{\partial F_r}{\partial \mathbf{u}_i} = \frac{2\ sign(\frac{\partial \rho_i}{\partial t})}{\rho_i} \frac{\partial (\frac{\partial \rho_i}{\partial t})}{\partial \Xi_i} \mathbf{u}_i^T \mathbf{k}_i \tag{A.4}$$

and in the case of the interface fracture risk objective,

$$\frac{F_\sigma}{\partial \boldsymbol{\sigma}_e} = \sum_{i \in \mathbb{M}} \frac{\left(\sum \tilde{f}(\sigma_i, \tau_i)^p \right)^{\frac{1}{p}-1}}{d(x_e)} \frac{\partial \tilde{f}(\sigma_i, \tau_i)}{\partial f(\sigma_e, \tau_e)} \frac{\partial \tilde{f}(\sigma_i, \tau_i)}{\partial \boldsymbol{\sigma}_i} \tag{A.5}$$

$$\frac{\partial \tilde{f}(\sigma_i, \tau_i)}{\partial \boldsymbol{\sigma}_i} = \left(\frac{2}{S_t S_c} \sigma_i + \left(\frac{1}{S_t} + \frac{1}{S_c} \right) \right) \frac{\partial \sigma_i}{\partial \boldsymbol{\sigma}_i} + \frac{2}{S_s^2} \tau_i \frac{\partial \tau_i}{\partial \boldsymbol{\sigma}_i} \tag{A.6}$$

where

$$\frac{\partial \sigma_i}{\partial \boldsymbol{\sigma}_i} = e_{11} \tag{A.7}$$

with e_{11} defined as a 3×3 matrix of zeros with 1 at position $(1,1)$. Similarly,

$$\frac{\partial \tau_i}{\partial \boldsymbol{\sigma}_i} = \frac{1}{2\sqrt{\tau_i}} \begin{bmatrix} 0 & \boldsymbol{\sigma}_{12}^i & \boldsymbol{\sigma}_{13}^i \\ \boldsymbol{\sigma}_{21}^i & 0 & 0 \\ \boldsymbol{\sigma}_{31}^i & 0 & 0 \end{bmatrix} \tag{A.8}$$

where $\boldsymbol{\sigma}_{jk}^i$ is the component of the full rank stress tensor at position (j,k). Finally, the sensitivities of the stress tensor with respect to the element DOF displacements is

$$\frac{\partial \boldsymbol{\sigma}_i}{\partial \mathbf{u}_i} = \mathbf{Q}(\mathbf{n}_e)(\mathbf{C}_i \mathbf{B}_i)^{full} \mathbf{Q}^T(\mathbf{n}_e) \tag{A.9}$$

A.2 Loads and boundary conditions

In this work, the proximal part of the femur is modelled in isolation, with the sectioned distal face fully constrained and a set of static loads applied over $1\,\text{cm}^3$ regions. Load cases for walking and stair climbing, presented in Fig. A.1, were retrieved from [62], with slight modification to the load application points to fit the bone model.

Load case: Walking (BW = 836N)

Force	x	y	z	Locus
hip contact	-54.0	-32.8	-229.2	P0
intersegmental resultant	-8.1	-12.8	-78.2	P0
abductor	58.0	4.3	86.5	P1
tensor fascia latae, proximal part	7.2	11.6	13.2	P1
tensor fascia latae, distal part	-0.5	-0.7	-19.0	P1
vastus lateralis	-0.9	18.5	-92.9	P2

Load case: Stair Climbing (BW = 847N)

Force	x	y	z	Locus
hip contact	-59.3	-60.6	-236.3	P0
intersegmental resultant	-13.0	-28.0	-70.1	P0
abductor	70.1	28.8	84.9	P1
ilio-tibial tract, proximal part	10.5	3.0	12.8	P1
ilio-tibial tract, distal part	-0.5	-0.8	-16.8	P1
tensor fascia latae, proximal part	3.1	4.9	2.9	P1
tensor fascia latae, distal part	-0.2	-0.3	-6.5	P1
vastus lateralis	-2.2	22.4	-135.1	P2
vastus medialis	-8.8	39.6	-267.1	P3

Coordinates

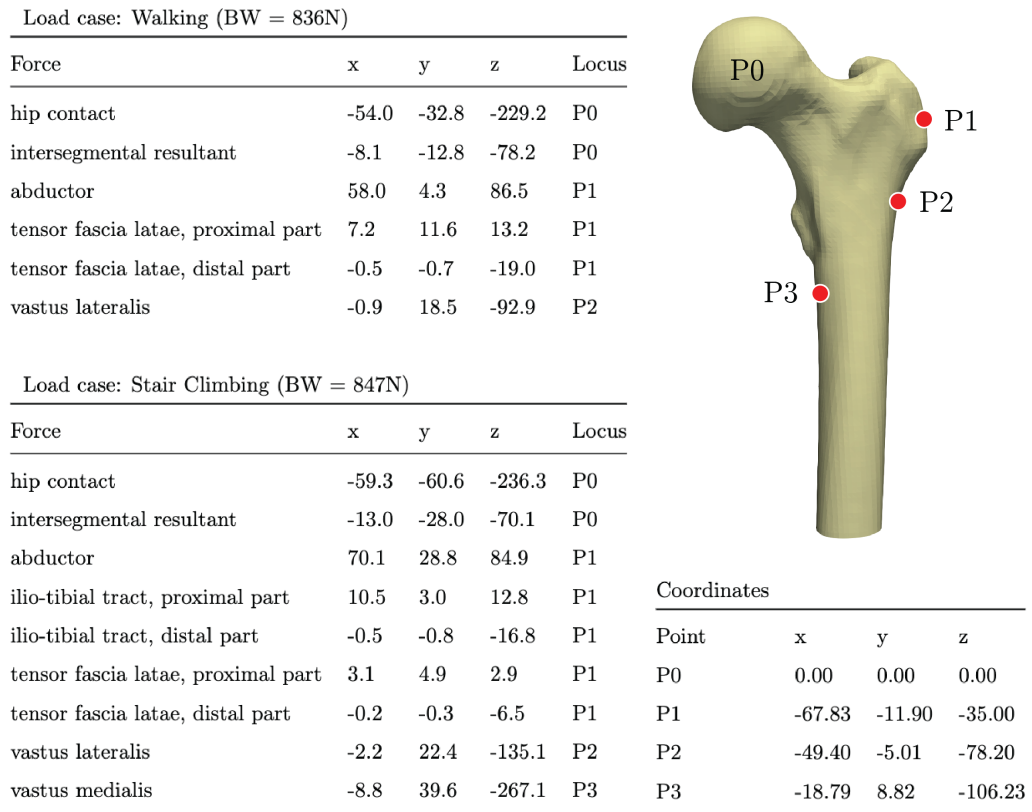| Point	x	y	z
P0	0.00	0.00	0.00
P1	-67.83	-11.90	-35.00
P2	-49.40	-5.01	-78.20
P3	-18.79	8.82	-106.23

Fig. A.1.: Load profiles used in the finite element analysis, obtained from [62]. The forces (in percentage of body weight), and the coordinates (in millimetres) are given in a local coordinate system of the femur [16]. The hip contact force acts at the origin of the coordinate system labelled as P0. The attachments or wrapping points of the muscles are labelled P1 to P3.

Appendix: Chapter 4

B.1 Finite element methods

The finite element analysis used to assess the risk of interface fracture is based on an enriched XFEM model with second-order displacement discontinuities along the bone-implant interface. The fixed isometric grid is extended from the design level set grid to encompass the entire pelvic bone and is comprised of tri-linear hexahedral elements with 1.45 mm side length. A detailed description of the XFEM strategy can be found in [97].

In order to assess the stress conditions along the bone-implant interface, appropriate loads and boundary conditions are essential. [53] proposed modeling both the sacroiliac joint and pubic symphysis as fully constrained. Instead, we apply an in-plane constraint on the pubic symphysis, which, we argue, more accurately reflects the bilateral symmetry of the full pelvis. The joint reaction force is distributed on the implant's inner surface, following the elastic body bearing pressure model described in [113]. All loads and boundary conditions are shown in Fig. B.1. The total magnitude and orientation correspond to the walking case described in [62].

Approximate bone densities and mechanical properties are mapped from the CT scan. Densities are obtained by linearly rescaling the Hounsfield values to a typical range of [0.04; 1.9] $\mathrm{g\,cm^{-3}}$ in accordance with [36]. The elastic moduli are then interpolated from the densities according to [98]. The density-dependent material strengths used to assess the Hoffman failure risk index are computed as per [142].

B.2 Sensitivity analysis

In order to use the insertability function in an optimization setting, we require the sensitivities with respect to the field of design variables. They are computed analytically with respect to the processed design variables as:
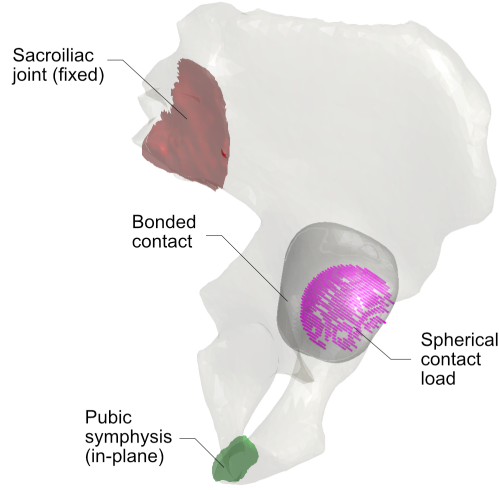
Fig. B.1.: An illustration of the loads and boundary conditions applied on the pelvis-implant system. The pelvis is fully fixated along the sacroiliac joint, and an in-plane constraint on the pubic symphysis prevents motion in the lateral direction. The implant-acetabulum interface is modeled as fully bonded. A joint reaction force corresponding to the walking case described in [62] is distributed on the spherical contact surface, following the elastic body bearing pressure model described in [113].

$$\frac{\partial F}{\partial \phi_j} = \frac{1}{\sum e^{\rho f_i}} \sum_{i=1}^{n} e^{\rho f_i} \frac{\partial f_i}{\partial \phi_j} \tag{B.1}$$

where the partial sensitivities of the local interference function at each vertex i are:

$$\frac{\partial f_i}{\partial \phi_j} = -\frac{\partial r_i^n}{\partial \phi_j} - \frac{r_i^t}{2\kappa_i^2} \sqrt{\frac{\kappa^{-2} - (r_i^t)^2}{\kappa^{-2}(r_i^t)^2}} \frac{\kappa_i^{-2} - 2(r_i^t)^2}{(\kappa_i^{-2} - (r_i^t)^2)^2} \frac{\partial r_i^t}{\partial \phi_j} + \frac{2\kappa_i^{-3}(r_i^t)^4}{(\kappa_i^{-2} - (r_i^t)^2)^2} \frac{\partial \kappa_i}{\partial \phi_j} \tag{B.2}$$

with

$$\frac{\partial r_i^n}{\partial \phi_j} = \hat{\mathbf{n}}_i^T \frac{\partial \mathbf{r}_i}{\partial \phi_j} + \mathbf{r}_i^T \frac{\partial \hat{\mathbf{n}}_i}{\partial \phi_j} \tag{B.3}$$

$$\frac{\partial r_i^t}{\partial \phi_j} = \left(\frac{\mathbf{r}_i^T - r_i^n \hat{\mathbf{n}}_i^T}{||\mathbf{r}_i - r_i^n \hat{\mathbf{n}}_i||} \right) \left(\frac{\partial \mathbf{r}_i}{\partial \phi_j} - r_i^n \frac{\partial \hat{\mathbf{n}}_i}{\partial \phi_j} \right) \tag{B.4}$$

and

$$\frac{\partial \mathbf{r}_i}{\partial \phi_j} = I_3 \Big(\mathrm{Rot}(\boldsymbol{\theta}) - 1 \Big) \frac{\partial \mathbf{b}_i}{\partial \phi_j} \tag{B.5}$$

$$\frac{\partial \hat{\mathbf{n}}_i}{\partial \phi_j} = \left(\frac{||\nabla \phi_i|| + \nabla \phi_i}{||\nabla \phi_i||^2} \right) \frac{\partial \nabla \phi_i}{\partial \phi_j} \tag{B.6}$$

$$\frac{\partial \nabla \phi_{q,r,s}}{\partial \phi_{q \pm 1,r,s}} = \pm \frac{1}{2} e_1 \tag{B.7}$$

$$\frac{\partial \nabla \phi_{q,r,s}}{\partial \phi_{q,r \pm 1,s}} = \pm \frac{1}{2} e_2 \tag{B.8}$$

$$\frac{\partial \nabla \phi_{q,r,s}}{\partial \phi_{q,r,s \pm 1}} = \pm \frac{1}{2} e_3 \tag{B.9}$$

Finally, the sensitivities of the interpolated vertex position $\mathbf{b}_i$ and gradient $\nabla \phi_i$ are equal to zero everywhere except at their respective edge parent nodes $p1$ and $p2$, for which:

$$\frac{\partial \mathbf{x}_i}{\partial \phi_{p1}} = \frac{\phi_{p2}}{(\phi_{p2} - \phi_{p1})^2} (\mathbf{x_{p1}} - \mathbf{x_{p2}}) \tag{B.10}$$

and

$$\frac{\partial \mathbf{x}_i}{\partial \phi_{p2}} = \frac{\phi_{p1}}{(\phi_{p2} - \phi_{p1})^2} (\mathbf{x_{p2}} - \mathbf{x_{p1}}) \tag{B.11}$$

where $\mathbf{x}$ represents either $\mathbf{b}_i$ or $\nabla \phi_i$.

Note that these sensitivities are computed with respect to the processed design variables ϕ. To obtain the sensitivities with respect to the actual design variables, the chain rule is applied.

$$\sum_{i \in N_{j,i}} \frac{\partial F}{\partial \phi_j} \frac{\partial \phi_j}{\partial \hat{s}_i} \frac{\partial \hat{s}_i}{\partial s_j} \tag{B.12}$$

Additionally, to automatically determine the appropriate extraction direction, we require the sensitivities with respect to the transformation T.

$$\frac{\partial F}{\partial T_j} = \frac{1}{\sum e^{\rho f_i}} \sum_{i=1}^{n} e^{\rho f_i} \frac{\partial f_i}{\partial T} \tag{B.13}$$

$$\frac{\partial f_i}{\partial T} = -\frac{\partial r_i^n}{\partial T}$$

$$-\frac{r_i^t}{2\kappa_i^2}\sqrt{\frac{\kappa^{-2} - (r_i^t)^2}{\kappa^{-2}(r_i^t)^2}}\,\frac{\kappa_i^{-2} - 2(r_i^t)^2}{(\kappa_i^{-2} - (r_i^t)^2)^2}\,\frac{\partial r_i^t}{\partial T} \tag{B.14}$$

$$\frac{\partial r_i^n}{\partial T} = \hat{\mathbf{n}}_i^T \frac{\partial \mathbf{r}_i}{\partial T} \tag{B.15}$$

$$\frac{\partial r_i^t}{\partial T} = \left(\frac{\mathbf{r}_i^T - r_i^n \hat{\mathbf{n}}_i^T}{||\mathbf{r}_i - r_i^n \hat{\mathbf{n}}_i||}\right)\frac{\partial \mathbf{r}_i}{\partial T} \tag{B.16}$$

$$\frac{\partial \mathbf{r}_i}{\partial T} = \left(\frac{\partial \mathbf{r}_i}{\partial \mathbf{p}}, \frac{\partial \mathbf{r}_i}{\partial \boldsymbol{\theta}}\right) \tag{B.17}$$

$$\frac{\partial \mathbf{r}_i}{\partial \theta_j} = \frac{\partial}{\partial \theta_j}\mathrm{Rot}(\boldsymbol{\theta}) \cdot \mathbf{b}_i \tag{B.18}$$

$$\frac{\partial \mathbf{r}_i}{\partial p_j} = e_j \tag{B.19}$$

where e_j is a null 3×1 vector with 1 at index j

The sensitivities of the shape-matching functions are given as:

$$\frac{\partial F_{S^*}}{\partial \phi_i} = \frac{1}{n}\sum_{i=1}^{n}\zeta\frac{d(\mathbf{b}_i, S)}{|d(\mathbf{b}_i, S)|}\frac{\partial \mathbf{b}_i}{\partial \phi_i} \tag{B.20}$$

where $\zeta = \alpha \;\; \forall d(\mathbf{b}_i, S) < 0$ and $\zeta = \beta \;\; \forall d(\mathbf{b}_i, S) \geq 0$

Appendix: Chapter 5 — C

C.1 Implementation

Results presented in this work were generated from code written and run in MATLAB R2023b on a MacBook Pro with M1 Max chip and 64 GB of unified memory. Details regarding the component design algorithm are included in [49]. Note that the standard (unbiased) shape matching objective was used. The designs presented in this work were generated on a normalized uniform design grid with $1.0\,\mathrm{mm}$ element side length, or roughly $500\,000$ nodal degrees of freedom. Run time varied between $1\,\mathrm{h}$ and $2\,\mathrm{h}$. It is expected that a significant reduction in run time could be achieved with code optimization and parallelization.

List of publications

Garner, E., Kolken, H. M., Wang, C. C., Zadpoor, A. A., & Wu, J. (2019). Compatibility in microstructural optimization for additive manufacturing. Additive Manufacturing, 26, 65-75.

Garner, E., Wu, J., & Zadpoor, A. A. (2022). Multi-objective design optimization of 3D micro-architected implants. Computer Methods in Applied Mechanics and Engineering, 396, 115102.

Garner, E., Wu, J., & Zadpoor, A.A. (2023). An insertability constraint for shape optimization. Structural and Multidisciplinary Optimization, 66:220.

Garner, E., Meynen, A., Scheys, L., Wu, J., & Zadpoor, A. A. (2023). Automated design of bone-preserving, insertable, and shape-matching patient-specific acetabular components. (submitted).

Biography

Eric Garner was born in Montreal, Canada, on December 7, 1992. He completed a B.Sc. degree in Mechanical Engineering (with distinction) at the University of Waterloo from 2011 to 2016, during which time he also worked in the industrial automation and consumer product design industries. He received an M.Sc. in Industrial Design Engineering from Delft University of Technology, in 2018. During his masters studies, he developed consumer-oriented products intended to create strong bonds between users and their products. He also designed a concept to promote worker satisfaction in Industry 4.0 for Canon Océ, which has since been patented. For his thesis, he pivoted to structural optimization, developing a solution to the problem of inter-cell connectivity in multi-scale topology optimization. In 2018, he accepted a PhD position in the department of Biomechanical Engineering, with the intention of applying new developments from the field of structural optimization to challenging problems in biomechanics.

Declaration

The author conceived and implemented all of the ideas presented in this document. Co-authors provided access to their prior research, participated in discussions, and assisted in the editing and revision of the manuscripts.

Delft, The Netherlands, March 12, 2024

_____

Eric Garner

Bibliography

[1] Mehmet Akgun, Raphael Haftka, K Wu, and Joanne Walsh. "Sensitivity of lumped constraints using the adjoint method". In: *40th structures, structural dynamics, and materials conference and exhibit*. 1999, p. 1314 (cit. on p. 66).

[2] Joe Alexandersen and Boyan S. Lazarov. "Topology optimisation of manufacturable microstructural details without length scale separation using a spectral coarse basis preconditioner". In: *Computer Methods in Applied Mechanics and Engineering* 290 (2015), pp. 156–182 (cit. on p. 11).

[3] Oded Amir, Niels Aage, and Boyan Lazarov. "On multigrid-CG for efficient topology optimization". In: *Structural and Multidisciplinary Optimization* 49 (May 2014), pp. 815–829 (cit. on pp. 24, 36).

[4] Ole Z Andersen, Vincent Offermanns, Michael Sillassen, et al. "Accelerated bone ingrowth by local delivery of strontium from surface functionalized titanium implants". In: *Biomaterials* 34.24 (2013), pp. 5883–5890 (cit. on p. 103).

[5] Casper Schousboe Andreasen, Martin Ohrt Elingaard, and Niels Aage. "Level set topology and shape optimization by density methods using cut elements with length scale control". In: *Structural and Multidisciplinary Optimization* 62.2 (2020), pp. 685–707 (cit. on pp. 68, 71, 72).

[6] Erik Andreassen, Boyan S. Lazarov, and Ole Sigmund. "Design of manufacturable 3D extremal elastic microstructure". In: *Mechanics of Materials* 69.1 (2014), pp. 1–10 (cit. on p. 8).

[7] Sajad Arabnejad and Damiano Pasini. "Mechanical properties of lattice materials via asymptotic homogenization and comparison with alternative homogenization methods". In: *International Journal of Mechanical Sciences* 77 (2013), pp. 249–262 (cit. on p. 52).

[8] Sajad Arabnejad and Damiano Pasini. "Multiscale Design and Multiobjective Optimization of Orthopedic Hip Implants with Functionally Graded Cellular Material". In: *Journal of Biomechanical Engineering* 134 (Mar. 2012), p. 031004 (cit. on pp. 35, 43).

[9] Rebecca L Austman, Jaques S Milner, David W Holdsworth, and Cynthia E Dunning. "The effect of the density–modulus relationship selected to apply material properties in a finite element model of long bone". In: *Journal of Biomechanics* 41.15 (2008), pp. 3171–3176 (cit. on p. 49).

[10] Ben Beklisi Kwame Ayawli, Ryad Chellali, Albert Yaw Appiah, and Frimpong Kyeremeh. "An overview of nature-inspired, conventional, and hybrid methods of autonomous vehicle path planning". In: *Journal of Advanced Transportation* 2018 (2018) (cit. on p. 61).

[11] Vamsi Krishna Balla, Subhadip Bodhak, Susmita Bose, and Amit Bandyopadhyay. "Porous tantalum structures for bone implants: fabrication, mechanical and in vitro biological properties". In: *Acta Biomaterialia* 6.8 (2010), pp. 3349–3359 (cit. on pp. 8, 35).

[12] Caterina Balletti, Martina Ballarin, and Francesco Guerra. "3D printing: State of the art and future perspectives". In: *Journal of Cultural Heritage* 26 (2017), pp. 172–182 (cit. on p. 56).

[13] Bernd-Arno Behrens, CJ Wirth, H Windhagen, et al. "Numerical investigations of stress shielding in total hip prostheses". In: *Proceedings of the Institution of Mechanical Engineers, Part H: Journal of Engineering in Medicine* 222.5 (2008), pp. 593–600 (cit. on p. 35).

[14] M.P. Bendsøe and O. Sigmund. *Topology Optimization: Theory, Methods, and Applications*. Springer Berlin Heidelberg, 2011 (cit. on pp. 8, 16).

[15] Martin P Bendsøe and Ole Sigmund. "Material interpolation schemes in topology optimization". In: *Archive of applied mechanics* 69.9-10 (1999), pp. 635–654 (cit. on p. 12).

[16] G Bergmann, F Graichen, and A Rohlmann. "Hip joint forces in sheep". In: *Journal of biomechanics* 32.8 (1999), pp. 769–777 (cit. on p. 107).

[17] Daniel J Berry, Richard A Berger, John J Callaghan, et al. "Symposium: Minimally invasive total hip arthroplasty". In: *The Journal of Bone and Joint Surgery* 85.11 (2003), pp. 2235–2246 (cit. on p. 53).

[18] FSL Bobbert, K Lietaert, Ali Akbar Eftekhari, et al. "Additively manufactured metallic porous biomaterials based on minimal surfaces: A unique combination of topological, mechanical, and mass transport properties". In: *Acta biomaterialia* 53 (2017), pp. 572–584 (cit. on p. 102).

[19] Nicolae Ciprian Bota, Dan-Viorel Nistor, Sergiu Caterev, and Adrian Todor. "Historical overview of hip arthroplasty: From humble beginnings to a high-tech future". In: *Orthopedic Reviews* 13.1 (2021) (cit. on p. 1).

[20] Kevin J Bozic, Steven M Kurtz, Edmund Lau, et al. "The epidemiology of revision total hip arthroplasty in the United States". In: *JBJS* 91.1 (2009), pp. 128–133 (cit. on p. 93).

[21] Frederick F Buechel and Michael J Pappas. "Properties of materials used in orthopaedic implant systems". In: *Principles of Human Joint Replacement*. Springer, 2015, pp. 1–32 (cit. on p. 34).

[22] William D Bugbee, William J Culpepper, C Anderson Engh, and CHARLES A Engh. "Long-term clinical consequences of stress-shielding after total hip arthroplasty without cement". In: *The Journal of Bone and Joint Surgery* 79.7 (1997), pp. 1007–1012 (cit. on p. 35).

[23] Joseph E. Cadman, Shiwei Zhou, Yuhang Chen, and Qing Li. "On design of multifunctional microstructural materials". In: *Journal of Materials Science* 48.1 (Jan. 2013), pp. 51–66 (cit. on p. 8).

[24] John Canny. *The complexity of robot motion planning*. MIT press, 1988 (cit. on p. 60).

[25] James F Carley. *Whittington's dictionary of plastics*. CRC Press, 1993 (cit. on p. 60).

[26] Isabelle Catelas and Joshua J Jacobs. "Biologic activity of wear particles". In: *Instructional Course Lectures* 59 (2010), pp. 3–16 (cit. on p. 35).

[27] V.J. Challis, A.P. Roberts, and A.H. Wilkins. "Design of three dimensional isotropic microstructures for maximized stiffness and conductivity". In: *International Journal of Solids and Structures* 45.14 (2008), pp. 4130–4146 (cit. on p. 8).

[28] Ao Chamay. "Mechanical and morphological aspects of experimental overload and fatigue in bone". In: *Journal of Biomechanics* 3.3 (1970), pp. 263–270 (cit. on p. 44).

[29] Guobao Chen, Chanjuan Dong, Li Yang, and Yonggang Lv. "3D scaffolds with different stiffness but the same microstructure for bone tissue engineering". In: *ACS applied materials & interfaces* 7.29 (2015), pp. 15790–15802 (cit. on p. 103).

[30] Yongjun Chen, Zhigang Xu, Christopher Smith, and Jag Sankar. "Recent advances on the development of magnesium alloys for biodegradable implants". In: *Acta biomaterialia* 10.11 (2014), pp. 4561–4573 (cit. on p. 103).

[31] AJT Clemow, AM Weinstein, JJ Klawitter, J Koeneman, and J Anderson. "Interface mechanics of porous titanium implants". In: *Journal of Biomedical Materials Research* 15.1 (1981), pp. 73–82 (cit. on p. 46).

[32] P. Coelho, Paulo Fernandes, Jose Guedes, and Hélder Rodrigues. "A hierarchical model for concurrent material and topology optimisation of three-dimensional structures". In: *Structural and Multidisciplinary Optimization* 35 (Feb. 2008), pp. 107–115 (cit. on pp. 11, 36).

[33] Andrew D. Cramer, Vivien J. Challis, and Anthony P. Roberts. "Microstructure interpolation for macroscopic design". In: *Structural and Multidisciplinary Optimization* 53.3 (Mar. 2016), pp. 489–500 (cit. on pp. 9, 25).

[34] Andrew D. Cramer, Vivien J. Challis, and Anthony P. Roberts. "Microstructure interpolation for macroscopic design". In: *Structural and Multidisciplinary Optimization* 53.3 (Mar. 2016), pp. 489–500 (cit. on p. 36).

[35] RD Crowninshield, RA Brand, RC Johnston, and JC Milroy. "An analysis of femoral component stem design in total hip arthroplasty". In: *The Journal of bone and joint surgery* 62.1 (1980), pp. 68–78 (cit. on p. 35).

[36] M Dalstra, R Huiskes, AV Odgaard, and L Van Erning. "Mechanical and textural properties of pelvic trabecular bone". In: *Journal of biomechanics* 26.4-5 (1993), pp. 523–535 (cit. on p. 109).

[37] Jeanette E Dalton, Stephen D Cook, Kevin A Thomas, and John F Kay. "The effect of operative fit and hydroxyapatite coating on the mechanical and biological response to porous implants." In: *JBJS* 77.1 (1995), pp. 97–110 (cit. on p. 93).

[38] John E Davies, Elnaz Ajami, Rahim Moineddin, and Vanessa C Mendes. "The roles of different scale ranges of surface implant topography on the stability of the bone/implant interface". In: *Biomaterials* 34.14 (2013), pp. 3535–3546 (cit. on p. 46).

[39] Guoying Dong, Yunlong Tang, and Yaoyao Fiona Zhao. "A 149 line homogenization code for three-dimensional cellular materials written in matlab". In: *Journal of Engineering Materials and Technology* 141.1 (2019), p. 011005 (cit. on p. 40).

[40] Zongliang Du, Xiao-Yi Zhou, Renato Picelli, and H Alicia Kim. "Connecting microstructures for multiscale topology optimization with connectivity index constraints". In: *Journal of Mechanical Design* 140.11 (2018), p. 111417 (cit. on pp. 11, 38).

[41] Ch A Engh, JD Bobyn, and Andrew H Glassman. "Porous-coated hip replacement. The factors governing bone ingrowth, stress shielding, and clinical results". In: *The Journal of Bone and Joint Surgery* 69-B.1 (1987), pp. 45–55 (cit. on p. 36).

[42] CHARLES A Engh, ANDREW H Glassman, and KATHLEEN E Suthers. "The case for porous-coated hip implants. The femoral side". In: *Clinical Orthopaedics and Related Research* 261 (1990), pp. 63–81 (cit. on p. 35).

[43] VA Eremeyev, A Skrzat, and F Stachowicz. "Linear micropolar elasticity analysis of stresses in bones under static loads". In: *Strength of Materials* 49.4 (2017), pp. 575–585 (cit. on p. 50).

[44] SL Evans and PJ Gregson. "Composite technology in load-bearing orthopaedic implants". In: *Biomaterials* 19.15 (Aug. 1998), pp. 1329–1342 (cit. on p. 35).

[45] Bernard Faverjon. "Obstacle avoidance using an octree in the configuration space of a manipulator". In: *Proceedings. 1984 IEEE International Conference on Robotics and Automation*. Vol. 1. IEEE. 1984, pp. 504–512 (cit. on p. 61).

[46] M Fraldi, L Esposito, G Perrella, A Cutolo, and SC Cowin. "Topological optimization in hip prosthesis design". In: *Biomechanics and Modeling in Mechanobiology* 9 (2010), pp. 389–402 (cit. on pp. 35, 43).

[47] George W Fryhofer, Sireesh Ramesh, and Neil P Sheth. "Acetabular reconstruction in revision total hip arthroplasty". In: *Journal of Clinical Orthopaedics and Trauma* 11.1 (2020), pp. 22–28 (cit. on pp. 3, 88).

[48] Eric Garner, Helena MA Kolken, Charlie CL Wang, Amir A Zadpoor, and Jun Wu. "Compatibility in microstructural optimization for additive manufacturing". In: *Additive Manufacturing* 26 (2019), pp. 65–75 (cit. on pp. 36, 38).

[49] Eric Garner, Jun Wu, and Amir Zadpoor. "An insertability constraint for shape optimization [Manuscript submitted for publication]." In: *Structural and multidisciplinary optimization* (2023) (cit. on pp. 88, 89, 91, 113).

[50] Eric Garner, Jun Wu, and Amir A Zadpoor. "Multi-objective design optimization of 3D micro-architected implants". In: *Computer Methods in Applied Mechanics and Engineering* 396 (2022), p. 115102 (cit. on pp. 81, 86, 96).

[51] Olivier Gauthier, Jean-Michel Bouler, Eric Aguado, Paul Pilet, and Guy Daculsi. "Macroporous biphasic calcium phosphate ceramics: influence of macropore diameter and macroporosity percentage on bone ingrowth". In: *Biomaterials* 19.1-3 (1998), pp. 133–139 (cit. on p. 36).

[52] Naeim Ghavidelnia, Mahdi Bodaghi, and Reza Hedayati. "Femur auxetic meta-implants with tuned micromotion distribution". In: *Materials* 14.1 (2021), p. 114 (cit. on pp. 5, 38).

[53] Rajesh Ghosh, Bidyut Pal, Debatri Ghosh, and Sanjay Gupta. "Finite element analysis of a hemi-pelvis: the effect of inclusion of cartilage layer on acetabular stresses and strain". In: *Computer methods in biomechanics and biomedical engineering* 18.7 (2015), pp. 697–710 (cit. on p. 109).

[54] AH Glassman, JD Bobyn, and M Tanzer. "New femoral designs: do they influence stress shielding?" In: *Clinical Orthopaedics and Related Research* 453 (2006), pp. 64–74 (cit. on p. 35).

[55] ST Gross and EW Abel. "A finite element analysis of hollow stemmed hip prostheses as a means of reducing stress shielding of the femur". In: *Journal of Biomechanics* 34.8 (2001), pp. 995–1003 (cit. on p. 35).

[56] JoséMiranda Guedes and Noboru Kikuchi. "Preprocessing and postprocessing for materials based on the homogenization method with adaptive finite element methods". In: *Computer Methods in Applied Mechanics and Engineering* 83.2 (1990), pp. 143–198 (cit. on pp. 13, 23).

[57] J. K. Guest, J. H. Prévost, and T. Belytschko. "Achieving minimum length scale in topology optimization using nodal design variables and projection functions". In: *International Journal for Numerical Methods in Engineering* 61.2 (2004), pp. 238–254 (cit. on p. 16).

[58] Z. Hashin. "Analysis of Composite Materials—A Survey". In: *Journal of Applied Mechanics* 50.3 (Sept. 1983), pp. 481–505 (cit. on p. 14).

[59] Z. Hashin and S. Shtrikman. "A variational approach to the theory of the elastic behaviour of multiphase materials". In: *Journal of the Mechanics and Physics of Solids* 11.2 (1963), pp. 127–140 (cit. on p. 19).

[60] Yuhao He, Drew Burkhalter, David Durocher, and James M Gilbert. "Solid-Lattice Hip Prosthesis Design: Applying Topology and Lattice Optimization to Reduce Stress Shielding From Hip Implants". In: *2018 Design of Medical Devices Conference*. V001T03A001. ASME. 2018 (cit. on p. 35).

[61] Paul S Heckbert. "A seed fill algorithm". In: *Graphics gems* 275 (1990), pp. 721–722 (cit. on p. 73).

[62] MO Heller, Georg Bergmann, J-P Kassi, et al. "Determination of muscle loading at the hip joint for use in pre-clinical testing". In: *Journal of Biomechanics* 38.5 (2005), pp. 1155–1163 (cit. on pp. 41, 50, 106, 107, 109, 110).

[63] PA Hill. "Bone remodelling". In: *British journal of orthodontics* 25.2 (1998), pp. 101–107 (cit. on pp. 1, 35).

[64] Oscar Hoffman. "The brittle strength of orthotropic materials". In: *Journal of Composite Materials* 1.2 (1967), pp. 200–206 (cit. on pp. 46, 81).

[65] R. Huiskes, H. Weinans, and B. van Rietbergen. "The relationship between stress shielding and bone resorption around total hip stems and the effects of flexible materials". In: *Clinical Orthopaedics and Related Research* 274 (1992), pp. 124–34 (cit. on p. 35).

[66] Rik Huiskes, Harrie Weinans, HJ Grootenboer, et al. "Adaptive bone-remodeling theory applied to prosthetic-design analysis". In: *Journal of Biomechanics* 20.11-12 (1987), pp. 1135–1150 (cit. on pp. 1, 2, 44, 51).

[67] Joo Young Hwang, Jun Song Kim, Sang Seok Lim, and Kyu Ho Park. "A fast path planning by path graph optimization". In: *IEEE Transactions on systems, man, and cybernetics-part a: systems and humans* 33.1 (2003), pp. 121–129 (cit. on p. 61).

[68] Mike Itagaki. *Lower extremity CTS*. Feb. 2020 (cit. on p. 40).

[69] Leo Joskowicz and Russell H Taylor. "Interference-free insertion of a solid body into a cavity: An algorithm and a medical application". In: *The International journal of robotics research* 15.3 (1996), pp. 211–229 (cit. on pp. 60, 61, 84).

[70] Sertac Karaman and Emilio Frazzoli. "Sampling-based algorithms for optimal motion planning". In: *The international journal of robotics research* 30.7 (2011), pp. 846–894 (cit. on p. 61).

[71] Sadaf Kashef, Alireza Asgari, Timothy B Hilditch, et al. "Fracture toughness of titanium foams for medical applications". In: *Materials Science and Engineering: A* 527.29-30 (2010), pp. 7689–7693 (cit. on p. 35).

[72] Lydia Kavraki and J-C Latombe. "Randomized preprocessing of configuration for fast path planning". In: *Proceedings of the 1994 IEEE International Conference on Robotics and Automation*. IEEE. 1994, pp. 2138–2145 (cit. on p. 61).

[73] Sajad Arabnejad Khanoki and Damiano Pasini. "Fatigue design of a mechanically biocompatible lattice for a proof-of-concept femoral stem". In: *Journal of the Mechanical Behavior of Biomedical Materials* 22 (2013), pp. 65–83 (cit. on p. 43).

[74] H Kienapfel, C Sprey, A Wilke, and P Griss. "Implant fixation by bone ingrowth". In: *The Journal of arthroplasty* 14.3 (1999), pp. 355–368 (cit. on p. 103).

[75] Jung Taek Kim and Jeong Joon Yoo. "Implant design in cementless hip arthroplasty". In: *Hip & pelvis* 28.2 (2016), pp. 65–75 (cit. on p. 53).

[76] Helena MA Kolken, Shahram Janbaz, Sander MA Leeflang, et al. "Rationally designed meta-implants: a combination of auxetic and conventional meta-biomaterials". In: *Materials Horizons* 5.1 (2018), pp. 28–35 (cit. on p. 38).

[77] P Kowalczyk. "Design optimization of cementless femoral hip prostheses using finite element analysis". In: *Journal of Biomechanical Engineering* 123.5 (Oct. 2001), pp. 396–402 (cit. on p. 34).

[78] G Kreisselmeier and R Steinhauser. "Systematic control design by optimizing a vector performance index". In: *Computer aided design of control systems*. Elsevier, 1980, pp. 113–117 (cit. on p. 66).

[79] J.H. Kuiper and H.W.J. Huiskes. "Numerical optimization of hip-prosthetic stem material". In: *Recent advances in computer methods in biomechanics and biomedical engineering ams*. Ed. by J. Middleton, G.N. Pande, and K.R. Williams. Books and Journals International, 1992, pp. 76–84 (cit. on pp. 2, 35, 43).

[80] JH Kuiper and R Huiskes. "Mathematical optimization of elastic properties: application to cementless hip stem design". In: *Journal of Biomechanical Engineering* 119.2 (May 1997), pp. 166–174 (cit. on p. 35).

[81] Steven Kurtz, Fionna Mowat, Kevin Ong, et al. "Prevalence of primary and revision total hip and knee arthroplasty in the United States from 1990 through 2002". In: *The Journal of Bone and Joint Surgery* 87.7 (2005), pp. 1487–1497 (cit. on p. 34).

[82] Matthijs Langelaar. "Topology optimization for multi-axis machining". In: *Computer Methods in Applied Mechanics and Engineering* 351 (2019), pp. 226–252 (cit. on p. 62).

[83] Jean-Claude Latombe. *Robot motion planning*. Vol. 124. Springer Science & Business Media, 2012 (cit. on p. 60).

[84] Boyan Stefanov Lazarov and Ole Sigmund. "Filters in topology optimization based on Helmholtz-type differential equations". In: *International Journal for Numerical Methods in Engineering* 86.6 (2011), pp. 765–781 (cit. on p. 71).

[85] Dawei Li, Wenhe Liao, Ning Dai, et al. "Optimal design and modeling of gyroid-based functionally graded cellular structures for additive manufacturing". In: *Computer-Aided Design* 104 (2018), pp. 87–99 (cit. on pp. 9, 26).

[86] Hao Li, Zhen Luo, Liang Gao, and Paul Walker. "Topology optimization for functionally graded cellular composites with metamaterials by level sets". In: *Computer Methods in Applied Mechanics and Engineering* 328 (2018), pp. 340–364 (cit. on p. 9).

[87] Hao Li, Zhen Luo, Liang Gao, and Paul Walker. "Topology optimization for functionally graded cellular composites with metamaterials by level sets". In: *Computer Methods in Applied Mechanics and Engineering* 328 (2018), pp. 340–364 (cit. on p. 38).

[88] Panjian Li. "Biomimetic nano-apatite coating capable of promoting bone ingrowth". In: *Journal of Biomedical Materials Research Part A: An Official Journal of The Society for Biomaterials, The Japanese Society for Biomaterials, and The Australian Society for Biomaterials and the Korean Society for Biomaterials* 66.1 (2003), pp. 79–85 (cit. on p. 103).

[89] Hans Lindahl, Henrik Malchau, Peter Herberts, and Göran Garellick. "Periprosthetic femoral fractures: classification and demographics of 1049 periprosthetic femoral fractures from the Swedish National Hip Arthroplasty Register". In: *The Journal of arthroplasty* 20.7 (2005), pp. 857–865 (cit. on p. 93).

[90] K Lingaraj, YH Teo, and N Bergman. "The management of severe acetabular bone defects in revision hip arthroplasty using modular porous metal components". In: *The Journal of Bone & Joint Surgery British Volume* 91.12 (2009), pp. 1555–1560 (cit. on p. 88).

[91] Giselle Hsiang Loh, Eujin Pei, David Harrison, and Mario D. Monzón. "An overview of functionally graded additive manufacturing". In: *Additive Manufacturing* 23 (2018), pp. 34–44 (cit. on p. 8).

[92] Thi Thoa Mac, Cosmin Copot, Duc Trung Tran, and Robin De Keyser. "Heuristic approaches in robot path planning: A survey". In: *Robotics and Autonomous Systems* 86 (2016), pp. 13–28 (cit. on p. 61).

[93] Rajesh N Maniar and Tushar Singhi. "Patient specific implants: Scope for the future". In: *Current reviews in musculoskeletal medicine* 7 (2014), pp. 125–130 (cit. on p. 79).

[94] Fabrizio Matassi, Alessandra Botti, Luigi Sirleo, Christian Carulli, and Massimo Innocenti. "Porous metal for orthopedics implants". In: *Clinical Cases in Mineral and Bone Metabolism* 10.2 (2013), pp. 111–115 (cit. on p. 35).

[95] Alexander Meynen, Harold Matthews, Nele Nauwelaers, et al. "Accurate reconstructions of pelvic defects and discontinuities using statistical shape models". In: *Computer methods in biomechanics and biomedical engineering* 23.13 (2020), pp. 1026–1033 (cit. on pp. 80, 89, 91, 103).

[96] Alexander Meynen, Georges Vles, Amir A Zadpoor, Michiel Mulier, and Lennart Scheys. "The morphological variation of acetabular defects in revision total hip arthroplasty—a statistical shape modeling approach". In: *Journal of Orthopaedic Research®* 39.11 (2021), pp. 2419–2427 (cit. on pp. 89, 103).

[97] Nicolas Moës, John Dolbow, and Ted Belytschko. "A finite element method for crack growth without remeshing". In: *International Journal for Numerical Methods in Engineering* 46.1 (1999), pp. 131–150 (cit. on pp. 42, 109).

[98] Elise F Morgan, Ginu U Unnikrisnan, and Amira I Hussein. "Bone Mechanical Properties in Healthy and Diseased States". In: *Annual Review of Biomedical Engineering* 20 (2018), pp. 119–143 (cit. on pp. 34, 109).

[99] Lawrence E Murr, SM Gaytan, F Medina, et al. "Next-generation biomedical implants using additive manufacturing of complex, cellular and functional mesh arrays". In: *Philosophical Transactions of the Royal Society A: Mathematical, Physical and Engineering Sciences* 368.1917 (2010), pp. 1999–2032 (cit. on p. 36).

[100] Timo Niinimäki, Juhani Junila, and P Jalovaara. "A proximal fixed anatomic femoral stem reduces stress shielding". In: *International Orthopaedics* 25 (2001), pp. 85–88 (cit. on p. 35).

[101] Margaret A Nowicki, Nathan J Castro, Michael W Plesniak, and Lijie Grace Zhang. "3D printing of novel osteochondral scaffolds with graded microstructure". In: *Nanotechnology* 27.41 (2016), p. 414001 (cit. on p. 103).

[102] OECD. *Health at a Glance 2021*. 2021, p. 274 (cit. on p. 88).

[103] Jakub Olczak, Niklas Fahlberg, Atsuto Maki, et al. "Artificial intelligence for analyzing orthopedic trauma radiographs: deep learning algorithms—are they on par with humans for diagnosing fractures?" In: *Acta orthopaedica* 88.6 (2017), pp. 581–586 (cit. on p. 103).

[104] James H Oliver and H-T Huang. "Automated path planning for integrated assembly design". In: *Computer-aided design* 26.9 (1994), pp. 658–666 (cit. on p. 60).

[105] Kevin L Ong, Steven M Kurtz, Edmund Lau, et al. "Prosthetic joint infection risk after total hip arthroplasty in the Medicare population". In: *The Journal of arthroplasty* 24.6 (2009), pp. 105–109 (cit. on p. 93).

[106] Mikhail Osanov and James K. Guest. "Topology Optimization for Architected Materials Design". In: *Annual Review of Materials Research* 46.1 (2016), pp. 211–233 (cit. on p. 8).

[107] Ajit Panesar, Meisam Abdi, Duncan Hickman, and Ian Ashcroft. "Strategies for functionally graded lattice structures derived using topology optimisation for Additive Manufacturing". In: *Additive Manufacturing* 19 (2018), pp. 81–94 (cit. on pp. 9, 26).

[108] Wayne G Paprosky, Michael O'Rourke, and Scott M Sporer. "The treatment of acetabular bone defects with an associated pelvic discontinuity." In: *Clinical Orthopaedics and Related Research (1976-2007)* 441 (2005), pp. 216–220 (cit. on p. 88).

[109] Wayne G Paprosky, Paul G Perona, and Jeffrey M Lawrence. "Acetabular defect classification and surgical reconstruction in revision arthroplasty: a 6-year follow-up evaluation". In: *The Journal of arthroplasty* 9.1 (1994), pp. 33–44 (cit. on p. 93).

[110] Jayanthi Parthasarathy, Binil Starly, Shivakumar Raman, and Andy Christensen. "Mechanical evaluation of porous titanium (Ti6Al4V) structures with electron beam melting (EBM)". In: *Journal of the Mechanical Behavior of Biomedical Materials* 3.3 (2010), pp. 249–259 (cit. on p. 36).

[111] Robert Pivec, Aaron J. Johnson, Simon C. Mears, and Michael A. Mont. "Hip arthroplasty". In: *The Lancet* 380.9855 (2012), pp. 1768–1777 (cit. on pp. 1, 34).

[112] Nicholas MK Poon and Joaquim RRA Martins. "An adaptive approach to constraint aggregation using adjoint sensitivity analysis". In: *Structural and Multidisciplinary Optimization* 34 (2007), pp. 61–73 (cit. on p. 66).

[113] Valentin L Popov, Markus Heß, and Emanuel Willert. *Handbook of contact mechanics: exact solutions of axisymmetric contact problems*. Springer Nature, 2019 (cit. on pp. 109, 110).

[114] A. Radman, X. Huang, and Y. M. Xie. "Topology optimization of functionally graded cellular materials". In: *Journal of Materials Science* 48.4 (Feb. 2013), pp. 1503–1510 (cit. on pp. 9, 17, 26).

[115] JAMES A Rand and MB Coventry. "Stress fractures after total knee arthroplasty". In: *The Journal of Bone and Joint Surgery* 62.2 (1980), pp. 226–233 (cit. on p. 44).

[116] The American Joint Replacement Registry. "AAOS American Joint Replacement Registry 2022 Annual Report". In: *JAAOS-Journal of the American Academy of Orthopaedic Surgeons* (2022), p. 51 (cit. on p. 93).

[117] Ashley Reichardt, Andrew A. Shapiro, Richard Otis, et al. "Advances in additive manufacturing of metal-based functionally graded materials". In: *International Materials Reviews* 66.1 (2021), pp. 1–29 (cit. on p. 36).

[118] Ke Ren, P Edward Purdue, Lyndsey Burton, et al. "Early detection and treatment of wear particle-induced inflammation and bone loss in a mouse calvarial osteolysis model using HPMA copolymer conjugates". In: *Molecular pharmaceutics* 8.4 (2011), pp. 1043–1051 (cit. on p. 3).

[119] Tobias Renkawitz, Francesco S Santori, Joachim Grifka, et al. "A new short uncemented, proximally fixed anatomic femoral implant with a prominent lateral flare: design rationals and study design of an international clinical trial". In: *BMC Musculoskeletal Disorders* 9 (2008), p. 147 (cit. on p. 35).

[120] Mohamad Ridzwan, Solehuddin Shuib, Hassan A.Y, Amran Ahmed Shokri, and Mohamad Ibrahim. "Problem of Stress Shielding and Improvement to the Hip Implant Designs: A Review". In: *Journal of Medical Sciences* 7.3 (2007), pp. 460–467 (cit. on p. 34).

[121] H. Rodrigues, J.M. Guedes, and M.P. Bendsøe. "Hierarchical optimization of material and structure". In: *Structural and Multidisciplinary Optimization* 24.1 (Aug. 2002), pp. 1–10 (cit. on pp. 11, 25, 29).

[122] A Rohlmann, U Mössner, G Bergmann, G Hees, and R Kölbel. "Effects of stem design and material properties on stresses in hip endoprostheses". In: *Journal of Biomedical Engineering* 9.1 (1987), pp. 77–83 (cit. on p. 35).

[123] E. Sacks and L. Joskowicz. "Computational Kinematic Analysis of Higher Pairs with Multiple Contacts". In: *Journal of Mechanical Design* 117.2A (June 1995), pp. 269–277 (cit. on p. 60).

[124] Gurunathan Saravana Kumar and Subin Philip George. "Optimization of custom cementless stem using finite element analysis and elastic modulus distribution for reducing stress-shielding effect". In: *Proceedings of the Institution of Mechanical Engineers, Part H: Journal of Engineering in Medicine* 231.2 (2017), pp. 149–159 (cit. on p. 43).

[125] J Schmidt and MH Hackenbroch. "The Cenos hollow stem in total hip arthroplasty: first experiences in a prospective study". In: *Archives of Orthopaedic and Trauma Surgery* 113.3 (1994), pp. 117–120 (cit. on p. 35).

[126] Marc-S Scholz, J.P. Blanchfield, L Dominic Bloom, et al. "The use of composite materials in modern orthopaedic medicine and prosthetic devices: A review". In: *Composites Science and Technology* 71 (Nov. 2011), pp. 1791–1803 (cit. on p. 35).

[127] Ashesh Sharma and Kurt Maute. "Stress-based topology optimization using spatial gradient stabilized XFEM". In: *Structural and Multidisciplinary Optimization* 57 (2018), pp. 17–38 (cit. on p. 72).

[128] Zhengshu Shen, Gaurav Ameta, Jami J. Shah, and Joseph K. Davidson. "A Comparative Study Of Tolerance Analysis Methods". In: *Journal of Computing and Information Science in Engineering* 5.3 (May 2005), pp. 247–256 (cit. on p. 60).

[129] Neil P Sheth, Charles L Nelson, Bryan D Springer, Thomas K Fehring, and Wayne G Paprosky. "Acetabular bone loss in revision total hip arthroplasty: evaluation and management". In: *JAAOS-Journal of the American Academy of Orthopaedic Surgeons* 21.3 (2013), pp. 128–139 (cit. on p. 88).

[130] Bruno Siciliano, Oussama Khatib, and Torsten Kröger. *Springer handbook of robotics*. Vol. 200. Springer, 2008 (cit. on p. 61).

[131] Nazmul Siddique and Hojjat Adeli. "Nature inspired computing: an overview and some future directions". In: *Cognitive computation* 7 (2015), pp. 706–714 (cit. on p. 61).

[132] O. Sigmund and S. Torquato. "Design of materials with extreme thermal expansion using a three-phase topology optimization method". In: *Journal of the Mechanics and Physics of Solids* 45.6 (1997), pp. 1037–1067 (cit. on p. 8).

[133] Ole Sigmund. "Materials with prescribed constitutive parameters: An inverse homogenization problem". In: *International Journal of Solids and Structures* 31.17 (1994), pp. 2313–2329 (cit. on pp. 8, 14).

[134] Ole Sigmund. "Morphology-based black and white filters for topology optimization". In: *Structural and Multidisciplinary Optimization* 33.4-5 (2007), pp. 401–424 (cit. on p. 16).

[135] Gustavo Assis da Silva, André Teófilo Beck, and Ole Sigmund. "Stress-constrained topology optimization considering uniform manufacturing uncertainties". In: *Computer Methods in Applied Mechanics and Engineering* 344 (2019), pp. 512–537 (cit. on p. 84).

[136] Jose Simões and António Marques. "Design of a composite hip femoral prosthesis". In: *Materials & Design* 26 (Aug. 2005), pp. 391–401 (cit. on p. 35).

[137] Matthew Sloan, Ajay Premkumar, and Neil P Sheth. "Projected volume of primary total joint arthroplasty in the US, 2014 to 2030". In: *JBJS* 100.17 (2018), pp. 1455–1460 (cit. on p. 88).

[138] Travis Small, Viktor Krebs, Robert Molloy, et al. "Comparison of acetabular shell position using patient specific instruments vs. standard surgical instruments: a randomized clinical trial". In: *The Journal of Arthroplasty* 29.5 (2014), pp. 1030–1037 (cit. on p. 79).

[139]L Spencer-Gardner, J Pierrepont, M Topham, et al. "Patient-specific instrumentation improves the accuracy of acetabular component placement in total hip arthroplasty". In: *The bone & joint journal* 98.10 (2016), pp. 1342–1346 (cit. on p. 79).

[140]Scott M Sporer and Wayne G Paprosky. "The use of a trabecular metal acetabular component and trabecular metal augment for severe acetabular defects". In: *The Journal of arthroplasty* 21.6 (2006), pp. 83–86 (cit. on pp. 88, 93).

[141]R Stamp, P Fox, W O'neill, E Jones, and C Sutcliffe. "The development of a scanning strategy for the manufacture of porous biomaterials by selective laser melting". In: *Journal of Materials Science: Materials in Medicine* 20.9 (2009), p. 1839 (cit. on p. 36).

[142]John L Stone, Gary S Beaupre, and Wilson C Hayes. "Multiaxial strength characteristics of trabecular bone". In: *Journal of Biomechanics* 16.9 (1983), pp. 743–752 (cit. on pp. 46, 109).

[143]Krister Svanberg. "The method of moving asymptotes—A new method for structural optimization". In: *International Journal for Numerical Methods in Engineering* 24.2 (1987), pp. 359–373 (cit. on pp. 16, 50).

[144]Krister Svanberg. "The method of moving asymptotes—a new method for structural optimization". In: *International journal for numerical methods in engineering* 24.2 (1987), pp. 359–373 (cit. on pp. 36, 72).

[145]Naoya Taniguchi, Shunsuke Fujibayashi, Mitsuru Takemoto, et al. "Effect of pore size on bone ingrowth into porous titanium implants fabricated by additive manufacturing: an in vivo experiment". In: *Materials Science and Engineering: C* 59 (2016), pp. 690–701 (cit. on p. 36).

[146]Nico P Van Dijk, Kurt Maute, Matthijs Langelaar, and Fred Van Keulen. "Level-set methods for structural topology optimization: a review". In: *Structural and Multidisciplinary Optimization* 48 (2013), pp. 437–472 (cit. on p. 68).

[147]Fengwen Wang, Boyan Stefanov Lazarov, and Ole Sigmund. "On projection methods, convergence and robust formulations in topology optimization". In: *Structural and Multidisciplinary Optimization* 43.6 (June 2011), pp. 767–784 (cit. on p. 17).

[148]Fengwen Wang, Boyan Stefanov Lazarov, and Ole Sigmund. "On projection methods, convergence and robust formulations in topology optimization". In: *Structural and Multidisciplinary Optimization* 43.6 (2011), pp. 767–784 (cit. on p. 71).

[149]Yingjun Wang, Sajad Arabnejad, Michael Tanzer, and Damiano Pasini. "Hip implant design with three-dimensional porous architecture of optimized graded density". In: *Journal of Mechanical Design* 140.11 (2018), p. 111406 (cit. on pp. 9, 26, 35).

[150]Yingjun Wang, Hang Xu, and Damiano Pasini. "Multiscale isogeometric topology optimization for lattice materials". In: *Computer Methods in Applied Mechanics and Engineering* 316 (2017), pp. 568–585 (cit. on pp. 11, 36).

[151]Yiqiang Wang, Feifei Chen, and Michael Yu Wang. "Concurrent design with connectable graded microstructures". In: *Computer Methods in Applied Mechanics and Engineering* 317 (2017), pp. 84–101 (cit. on p. 38).

[152] Yiqiang Wang, Lei Zhang, Stephen Daynes, et al. "Design of graded lattice structure with optimized mesostructures for additive manufacturing". In: *Materials & Design* 142 (2018), pp. 114–123 (cit. on p. 11).

[153] Andreas Weiler, Reinhard FG Hoffmann, Andreas C Stähelin, Hanns-Joachim Helling, and Norbert P Südkamp. "Biodegradable implants in sports medicine: the biological base". In: *Arthroscopy: The Journal of Arthroscopic & Related Surgery* 16.3 (2000), pp. 305–321 (cit. on p. 103).

[154] CE Wen, Y Yamada, K Shimojima, et al. "Processing and mechanical properties of autogenous titanium implant materials". In: *Journal of Materials Science: Materials in Medicine* 13.4 (2002), pp. 397–401 (cit. on p. 35).

[155] Michael R Whitehouse, Bassam A Masri, Clive P Duncan, and Donald S Garbuz. "Continued good results with modular trabecular metal augments for acetabular defects in hip arthroplasty at 7 to 11 years". In: *Clinical Orthopaedics and Related Research®* 473 (2015), pp. 521–527 (cit. on p. 88).

[156] J. Wu, N. Aage, R. Westermann, and O. Sigmund. "Infill Optimization for Additive Manufacturing; Approaching Bone-Like Porous Structures". In: *IEEE Transactions on Visualization and Computer Graphics* 24.2 (Feb. 2018), pp. 1127–1140 (cit. on pp. 11, 19, 20, 26).

[157] Jun Wu, Anders Clausen, and Ole Sigmund. "Minimum compliance topology optimization of shell–infill composites for additive manufacturing". In: *Computer Methods in Applied Mechanics and Engineering* 326 (2017), pp. 358–375 (cit. on p. 11).

[158] Jun Wu, Christian Dick, and Rüdiger Westermann. "A System for High-Resolution Topology Optimization". In: *IEEE Transactions on Visualization and Computer Graphics* 22.3 (Mar. 2016), pp. 1195–1208 (cit. on pp. 13, 31, 36).

[159] Jun Wu, Ole Sigmund, and Jeroen Groen. "Topology Optimization of Multi-scale Structures: A Review". In: *Structural and Multidisciplinary Optimization* 63.3 (2021), pp. 1455–1480 (cit. on pp. 36, 38).

[160] Liang Xia and Piotr Breitkopf. "Concurrent topology optimization design of material and structure within FE2 nonlinear multiscale analysis framework". In: *Computer Methods in Applied Mechanics and Engineering* 278 (Aug. 2014), pp. 524–542 (cit. on p. 36).

[161] Liang Xia and Piotr Breitkopf. "Design of materials using topology optimization and energy-based homogenization approach in Matlab". In: *Structural and Multidisciplinary Optimization* 52.6 (Dec. 2015), pp. 1229–1241 (cit. on pp. 14, 18).

[162] Liang Xia and Piotr Breitkopf. "Recent advances on topology optimization of multi-scale nonlinear structures". In: *Archives of Computational Methods in Engineering* 24.2 (2017), pp. 227–249 (cit. on p. 11).

[163] Shengli Xu, Yuanwu Cai, and Gengdong Cheng. "Volume preserving nonlinear density filter based on heaviside functions". In: *Structural and Multidisciplinary Optimization* 41.4 (Apr. 2010), pp. 495–505 (cit. on p. 16).

[164]Suna Yan, Fengwen Wang, and Ole Sigmund. "On the non-optimality of tree struc-
tures for heat conduction". In: *International Journal of Heat and Mass Transfer* 122
(2018), pp. 660–680 (cit. on p. 31).

[165]Shoufeng Yang, Kah-Fai Leong, Zhaohui Du, and Chee-Kai Chua. "The design of
scaffolds for use in tissue engineering. Part II. Rapid prototyping techniques". In:
Tissue Engineering 8.1 (2002), pp. 1–11 (cit. on p. 36).

[166]Dong J Yoo. "Porous scaffold design using the distance field and triply periodic
minimal surface models". In: *Biomaterials* 32.31 (2011), pp. 7741–7754 (cit. on
p. 102).

[167]Dong-Jin Yoo. "Heterogeneous porous scaffold design for tissue engineering using
triply periodic minimal surfaces". In: *International Journal of Precision Engineering
and Manufacturing* 13 (2012), pp. 527–537 (cit. on p. 102).

[168]Amir A. Zadpoor. "Mechanical meta-materials". In: *Materials Horizons* 3 (5 2016),
pp. 371–381 (cit. on p. 8).

[169]Shiwei Zhou and Qing Li. "Design of graded two-phase microstructures for tailored
elasticity gradients". In: *Journal of Materials Science* 43.15 (2008), pp. 5157–5167
(cit. on pp. 9, 14, 38).

[170]Bo Zhu, Mélina Skouras, Desai Chen, and Wojciech Matusik. "Two-Scale Topology
Optimization with Microstructures". In: *ACM Trans. Graph.* 36.5 (July 2017) (cit. on
p. 9).

[171]David Zhu and Jean-Claude Latombe. *New heuristic algorithms for efficient hierarchi-
cal path planning*. Tech. rep. STANFORD UNIV CA DEPT OF COMPUTER SCIENCE,
1989 (cit. on p. 61).